2019

Photoresponse and Charge Transport in Halide Perovskites

Xi Wang

FLORIDA STATE UNIVERSITY

COLLEGE OF ARTS AND SCIENCES

PHOTORESPONSE AND CHARGE TRANSPORT IN HALIDE PEROVSKITES

By

XI WANG

A Dissertation submitted to the
Department of Physics
in partial fulfillment of the
requirements for the degree of
Doctor of Philosophy

2019

Xi Wang defended this dissertation on June 7, 2019.
The members of the supervisory committee were:

Hanwei Gao
Professor Directing Dissertation

Eric Hellstrom
University Representative

Nick Bonesteel
Committee Member

Jorge Piekarewicz
Committee Member

Peng Xiong
Committee Member

The Graduate School has verified and approved the above-named committee members, and certifies that the dissertation has been approved in accordance with university requirements.

Dedication to my beloved mother, Qiuju He

father, Jinbiao Wang

and my husband Dong Li

ACKNOWLEDGMENTS

I would like to thank my mother first. Life was tough for a single mother. But she always tried her best to support me through so many years, even I wanted to go to America to get a Ph.D. degree. Without her moral support and encouragement through so many years, everything is impossible. She was also my role model to fight the challenges in my life. Though she couldn't know anymore, I still want to say thank you, for your love and support.

After I came to America, I was alone. I was so lucky to meet my husband, a considerate thoughtful person. I would like to thank my husband to take care of me for the past seven years, and his unconditional support for my work.

I joined Prof. Hanwei Gao's group in 2014. I really enjoyed the time as a student in his research group. His passion for science, his rigorous attitude to research, his patience to educate students, undoubtfully affected me. I have learned a lot from him in the past five years, not only limited to experimental skills, problem-solving capability and scientific thinking, but also how to manage life, enjoy life and communicate with different people. He is not just my advisor in research. He is my mentor in life.

I want to thank Prof. Peng Xiong, for the encouragement, helpful discussion with research, and giving me the opportunities to share equipment with his group. Prof. Xiong treated me as his own student. I really appreciate his guidance and support. Prof. Xiong's students, Jorge Barreda, Timothy Keiper, and Longqian Hu provided me a lot of help, also collaborations when I started my research in Prof. Gao's group as his first student. Also, thank Prof. Shangchao Ling to useful research discussion and collaborations.

I would like to express my gratitude to Prof. Jorge Piekarewicz, for always being so supportive and encouraging. I am very pleased to have him as my Ph.D. committee member. I also would like to Prof. Simon Capstick. When I made my decision to transfer to Prof. Gao's research group, it was approaching the end of my third year in Ph.D. He told me to go for the decisions making my life better as the department was always backing up for me.

I am grateful to thank Mr. Kurt Koetz, Dr. Eric Lochner, Mr. Robert Smith, and the staff of the Physics Machine Shop (Ian Winger, Greg White, Randall Smith) for their help with the experiments and equipment in our lab. Especially Kurt, Eric and Ian, I really appreciate the useful discussions with you for designing facilities and improvement of experimental setups.

Finally, thank members of my advising committee, Prof. Eric Hellstrom and Prof. Nick Bonesteel. Thank my lab colleagues Yichuan Ling, Xiujun Lian, Yu-Che Chiu, Fernando Perez-Orive, Javan Knox, Yijun Du, Xavier Quintatna and Zihan Zhang. I had a great 5-year time at FSU, with all the great people I have met here. Please accept my apologies if I unintentionally forgot to mention any names here.

TABLE OF CONTENTS

LIST OF TABLES

LIST OF FIGURES

ABSTRACT

Halide Perovskites have recently risen as a new class of optoelectronic materials. Remarkable optical and electrical properties have led to the demonstration of various perovskite-based devices such as solar cells[1], LEDs[2-5], photodetectors[6] and lasers[7,8]. Particularly, perovskite solar cells have reached >24% of the energy conversion efficiency and outperformed most of the single-junction thin film solar cells available on the market[1]. Unfortunately, most of the perovskite-based devices remained more-or-less unstable due to a series of unusual behaviors such as current-voltage hysteresis[9] and photo-induced phase segregation[10,11]. Studies about the underlying mechanisms are in demand.

In this dissertation, I focused on studying the charge transport and photoresponse of halide perovskites to reveal the mechanisms related to material stability, particularly under electrical and optical stimuli. The changes of halide perovskite materials in a device under electrical operation were studied by using a microscopic tool, scanning photocurrent microscopy. The results showed the dynamic nature of the doping concentration in the hybrid perovskite $CH_3NH_3PbI_3$, as a function of the external biasing voltages. Further studies on the synthesis methods showed such a dynamic process could be attributed to electric field-assisted ion migration mainly through defect sites. The partial suppression of ion migration was observed in materials processed at higher temperature.

Except the electric-field triggered instability of the internal potential distribution, while under illumination, a different type of stability, the phase stability in mixed-halide perovskites attracted a lot of attention. Phase separation in mixed-halide perovskites under illumination was a tough problem, which directly related to the degradation of desired device performance. In this dissertation, the correlation between the phase stability and morphology was discovered. A model based on thermodynamics was developed to explain such a correlation. Based on the thermodynamic model, the composite materials $CsPbX_3/Cs_4PbX_6$ with guest-host structures were created with the phase separation problem successfully solved. Furthermore, the composites are sustainably functionalized even under extreme conditions, i.e., under extremely intense illumination, making the composited useful for devices required to work in extreme conditions.

The optical and electrical properties of $CsPbX_3/Cs_4PbX_6$ composites were further investigated for the application of such composites to functional devices. Surprisingly, the presence of the photoluminescence inactive Cs_4PbBr_6 can significantly enhance the light emitting efficiency of $CsPbBr_3$ in the composites. The unique negative thermal quenching observed near the liquid

nitrogen temperature indicates that a type of shallow states generated at the $CsPbBr_3/Cs_4PbBr_6$ interfaces is responsible for the enhancement of photoluminescence. Finally, light emitting diodes based on $CsPbBr_3/Cs_4PbBr_6$ composites are demonstrated. Both quantum efficiency and emission brightness are improved significantly compared with similar devices constructed using pure $CsPbBr_3$. The unfavorable charge transport property of host matrix Cs_4PbBr_6 could be circumvented by optimizing the ratio between the host and the guest components and the total thickness of the composite thin films. The inorganic composition of the emitting layer also leads to improved device stability under the condition of continuous operation.

The studies in this dissertation indicated great potentials of composite materials with optimized designed properties. Depends on the application purposes, more matrix materials with the combination of halide perovskites need to be explored. The future plan will more directed to the investigations of fundamental photophysics and charge transport in a large collection of compositing combinations.

CHAPTER 1
INTRODUCTION

Semiconductors technology has been the backbone of many popular optoelectronic devices, including the modern computers whose central processing unit (CPU) is composed of field-effect transistors, Light Emitting Diodes (LEDs) inside lightbulbs and indicator signs, state of the art screen display in cellphones, solar panels for Eco-friendly energy production, and photodetectors in cameras. Although semiconductors were discovered over 100 years, researchers never stopped developing new generations of semiconductor-based technology to enhance and simplify life for future generations.

My Ph.D. work focused on studying the photoresponse and charge transport in emerging semiconductors, for example, vanadium dioxide (VO_2) and halide perovskites. In this dissertation, I mainly present my experimental studies performed on halide perovskites.

My work about halide perovskites is composed of three parts. The first part, Chapter 2, is the microscopic studies on organic-inorganic hybrid perovskite $CH_3NH_3PbI_3$ using scanning photocurrent microscopy. This study revealed the dynamic nature of the doping concentration in the hybrid perovskite $CH_3NH_3PbI_3$, which can be tuned by the external biasing voltages. Further studies on the synthesis methods showed such a dynamic process could be attributed to defect-assisted ion migration. The suppression of ion migration was observed in materials processed at higher temperature. Results are published in Nano Letters in 2017[12]. The second part, Chapter 3, is about the tunability of phase stability in mixed-halide perovskites. The phase separation in mixed-halide perovskites under illumination was a tough problem, which directly related to the degradation of desired device performance. In my study, I found out the underlying mechanism responsible for such phase separation. A model based on thermodynamics explained the correlation between the phase stability and morphology. With the mechanism known, I further created composite materials $CsPbX_3/Cs_4PbBr_6$ with guest-host structures. The phase separation problem was successfully solved in such composite materials. Furthermore, I found out, the composites are sustainably functionalized even under extreme conditions, i.e., under extremely intense illumination. The related results are published in Nature Communication in 2019[13]. The last major part, Chapter 4, of my work is to study the optical and electrical properties of $CsPbX_3/Cs_4PbX_6$ composites. There are two parameters, the ratio between halide ions and the ratio between the host Cs_4PbX_6 and the guest $CsPbX_3$. We fixed one parameter at one time and vary

another one. The more important parameter that affects the electric behavior is the ratio between Cs_4PbX_6 and $CsPbX_3$. Therefore, my studies started from the pure bromine-based composite and change only the ratio between the host Cs_4PbBr_6 and the guest $CsPbBr_3$. Further applications to optoelectronic devices, such as Light-emitting diodes, were investigated. I was involved in the built of the equipment, developing evaporation receipt and data analysis in the project focusing on the optical properties of $CsPbBr_3/Cs_4PbBr_6$ composites. The related results have been published in the Journal of Physical Chemistry Letter[14]. My colleague Xiujun Lian and I (Equally contribution) later focused on studying the electric properties and the demonstration of LED devices. The results are published in Advanced Functional Materials[15].

The other Appendices contain the detailed modeling with calculations related to phase stability in mixed-halide perovskites. The fabrication of LED devices is also included in a separate appendix.

The VO_2 project deviates from the outline of this dissertation. The related results can be found in Nano Letters which was published in 2015[16].

I believe, the studies presented here had an important contribution to understand the properties of halide perovskites, and might bring the field closer to the realization of marketing applications based on halide perovskites.

1.1 Introduction to halide perovskites

Halide perovskites, an emerging class of semiconductors, have shown great potential of revolutionizing optoelectronics with improved performance and lower costs. Examples of optoelectronics that have received most attention include perovskite-based solar cells, whose efficiency increased to 23.7% with only 5-years development[1]. For comparison, the highest solar panel efficiency based on thin-film silicon is 21.2%. In the meantime, the cost of such perovskite-based devices is much lower than other semiconductor devices due to its facile synthetic procedure and earth-abundant composition. Besides, the perovskites also showed promises for LED applications with the color tunable across the entire visible range [2-5]. Such LEDs are critical components in, for example, affordable full-color displays with sharp contrast. Perovskites have found many applications beyond PV (solar cells) and light-emitting diodes, expanding into the areas of photodetectors[6], X-ray detectors[17], Gamma-ray detectors[18], Gamma-ray scintillator[19], memory devices[20], and so on.

Halide perovskites, falling into the general perovskite category, are a class of compounds which have the same type of crystal structure of Perovskite, $CaTiO_3$, called perovskite structure (Figure 1-1). The general chemical formula is ABX_3, where A (e.g. Cs^+, Rb^+, $CH_3NH_3^+$, $HC(NH_2)_2^+$) and B (e.g. Pb^{2+}, Sn^{2+}) are two cations and X (e.g. Cl^-, Br^-, I^-) is an anion. Perovskites have many appealing properties in both experiments and theories, for example, colossal magnetoresistance, ferroelectricity, superconductivity and so on[21]. Metal halide perovskites are a class of semiconducting materials out of the perovskite family. Particularly, light-matter interactions in metal halide perovskites attracted an enormous amount of attention in recently year. The related properties that make such materials suitable for the application of various optoelectronic devices such as large absorption coefficient[22], the high efficiency to convert photon energy to electrical energy (efficient PV, photodetectors as mentioned at the beginning). Besides, the rather processing steps are simple and low-cost. All kinds of general material processing methods have the access to synthesize halide perovskites materials including spin-coating, evaporation or even casting at room temperature[23,24].

Besides the general good properties of metal halide perovskites, some of the special properties attract the researchers' attention. For example, the softness of the lattice frame[25,26], highly mobile ions[27], as well as the phase stability issues in some of the halide perovskites[10,11,28]. These are closely related to the photoresponse of devices made out of perovskites. Abnormal large hysteresis in current-voltage relations, a huge change of dielectric constant when under illumination, as well as instability of bandgaps while under operation conditions are some of the examples. Yet, the underlying mechanisms are not clear.

In this chapter, general optoelectronic properties of metal halide perovskites will be introduced. Then I will focus on the discussion about the softness of the structures, the mobile ions and phase stability in halide perovskites, which are closely related to Chapter 2 and Chapter 3.

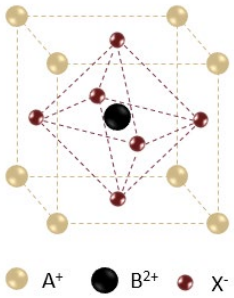

Figure 1-1 Structure of metal halide perovskite crystal.

1.1.1 General optoelectronic properties of halide perovskites

The important factors that support superior performance of devices based on metal halide perovskites are multiple-dimensional. The outstanding physical properties include (1) high optical absorption coefficient; (2) Long carrier lifetime; (3) Good mobility for both holes and electrons with well-balanced charge transfer (ambipolar); (4) Long carrier diffusion length as a result of long carrier lifetime and good mobility.

1.1.1.1 Strong absorption

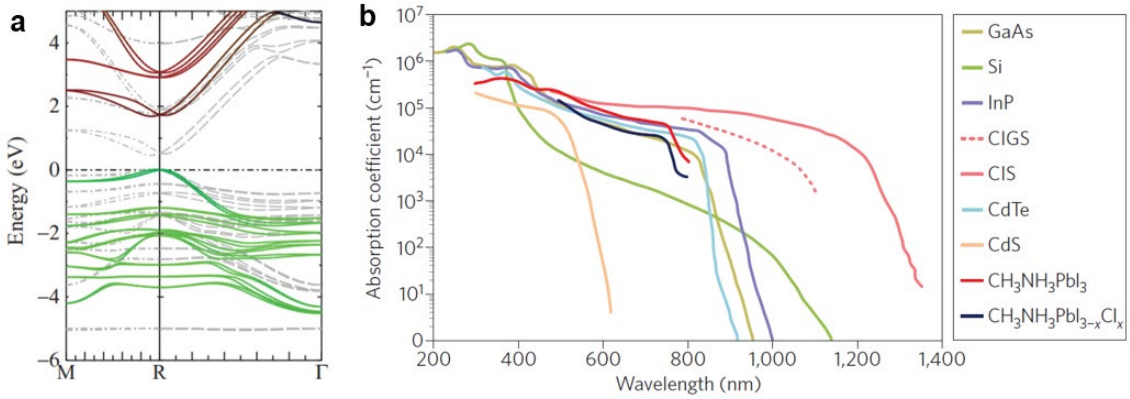

Figure 1-2 Bandgap information about metal halide perovskites. (a) Dispersion relation of $CH_3NH_3PbI_3$. (b) Absorption coefficient comparison for different semiconductors. (a) is adapted with permission[22]. Copyright 2014 American Physical Society. (b) is adapted with permission[29]. Copyright 2014 Nature Publishing Group.

Strong optical absorption is one of the keys to obtain solar cells with high performance. Both the requirements for layer thickness and charge carrier collections can be fulfilled more easily. Calculations showed the metal halide perovskites have direct bandgaps (e.g. Figure 1-2a calculated dispersion relation of $CH_3NH_3PbI_3$) [22]. The absorption measurements (Figure 1-2b) are consistent with calculations showing large absorption coefficient (>10^5 cm^{-1}) featuring direct bandgaps[29]. Besides the direct bandgap, the excitonic feature showed in the edge of the absorption, with excitonic binding energy 30-75 meV[29]., further expands the absorption range and strength. Since the binding energy of excitons is around room temperature range, the photogenerated excitons are easy to separate into free carriers, which further promotes the PV performance.

1.1.1.2 Relatively long carrier lifetime

Most of the trap states formed in $CH_3NH_3PbI_3$ are either shallow within the band gap or within the bands (valence band or conduction band) (Figure 1-3a). Carriers trapped in the shallow defect

states will detrap with the assistance of thermal perturbation easily. The charge carriers are almost not affected by these trap states in such case. But it's worth noting that deep traps can still be formed in halide perovskites, for example, deep traps on the surfaces[30-32]. The density of deep traps depends on the methods of synthesis[33]. Therefore, the passivation of surfaces, especially in polycrystalline thin films, is one of the critical issues that researchers are looking into. More details about surface passivation will be mentioned in Chapter 4.

Besides the defect tolerance, the high ionic density in halide perovskites helps to suppress recombination of charge carriers. The soft ionic lattices behave like "crystal-liquid", belongs to so-called phonon glass electron crystals, whose dielectric responses and phonon dynamics are typical of liquids. Phonon glass electron crystals are potential candidates for most efficient thermoelectrics[26]. The "crystal-liquid" duality with the resulting dielectric response is responsible for screening of charge carriers to suppress recombination by large polaron formation (Figure 1-3b). Though the mobility of charge carriers is affected by the charge-screening effect, the long diffusion lengths show limited compensation.

The charge carrier lifetimes are long in halide perovskites. The PL lifetime can be as long as > 1 μs in $CH_3NH_3PbI_3$ with passivated surfaces (Figure 1-3c) [34].

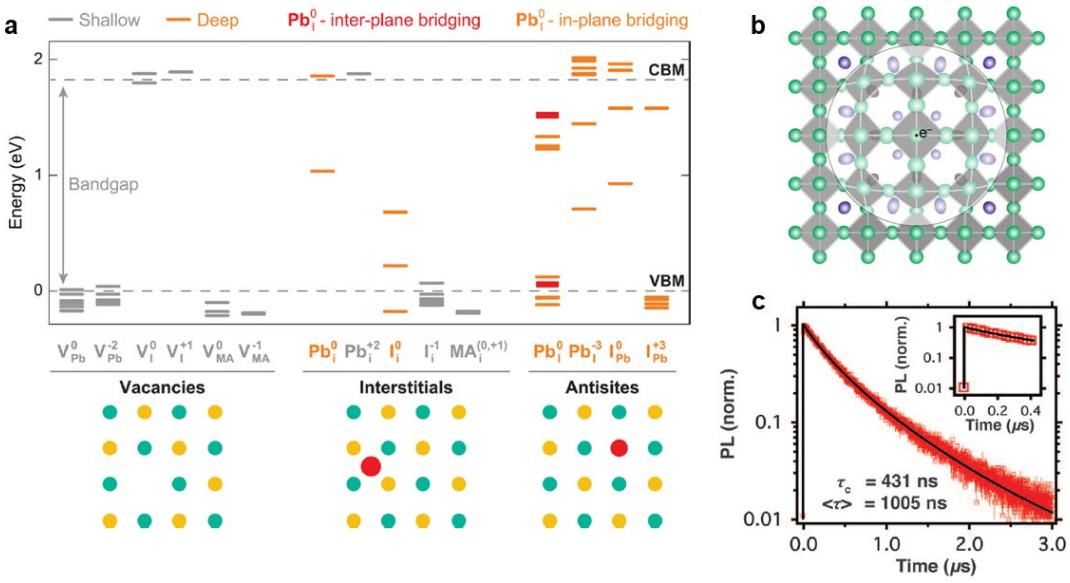

Figure 1-3 Relatively long carrier lifetime was observed in metal halide perovskites. (a) calculated defect levels in $CH_3NH_3PbI_3$. (b) schematic showing structural dynamic polaron in perovskites. (c) Long PL lifetime was measured in $CH_3NH_3PbI_3$. (a) is adapted with permission[30]. Copyright 2014 American Chemical Society. (b) is adapted with permission[35]. Copyright 2018 Nature Publishing Group. (c) is adapted with permission[34]. Copyright 2015 American Association for the Advancement of Science.

1.1.1.3 High mobility

As intrinsic semiconductors, metal halide perovskites are almost ambipolar. The term ambipolar transport means the excess carriers behave with time and in space in the presence of electric fields and density gradients are of equal importance. The excess electrons and holes diffuse and drift with the same effective diffusion coefficient and with the same effective mobility.

The charge transport properties were studied by fabrication of field-effect transistors (FETs). Balanced electron and hole transport in $CH_3NH_3PbI_{3-x}Cl_x$ thin films were reported with mobilities of ~1 cm^2 /Vs at room temperature[36]. Similar effective mass values for both electrons and holes were calculated with $m^*(h) = 0.29m_0$ and $m^*(e) = 0.23m_0$ (m_0 is the rest mass of an electron, 9.11×10^{-31} kg) [37].

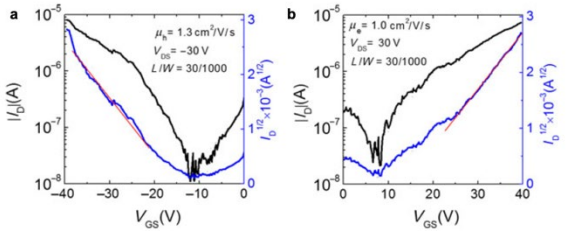

Figure 1-4 Drain current as a function of gating voltages for p-type transport (a) and n-type transport (b). Adapted with permission[36]. Copyright 2015 Material Research Society.

The photogenerated carriers in halide perovskites behave as free carriers, and these carriers can migrate in the perovskite absorber layer without recombination for a long time (long carrier lifetime as introduced in the previous session). The diffusion length ranges from 1 μm in polycrystalline thin films[38] to 100 μm in single crystals[39].

1.1.1.4 Tunable bandgap

Besides other desirable optical and electrical properties, the halide perovskites offered a unique opportunity to optimize the spectral range of photoresponse by tuning the bandgaps[40-43]. Two types of halogen anions can be accommodated in homogenous crystal lattices with nearly arbitrary mixing ratios, leading to a wide range of the bandgap tunability. For example, the bandgap of the perovskite $CsPb(Br_xI_{1-x})_3$ can be tuned continuously from 2.4 eV (corresponding to $CsPbBr_3$) to 1.75 eV (corresponding to $CsPbI_3$), covering half of the visible spectrum. The range could be further extended when chlorine was incorporated (Figure 1-5a, b) [40]. In optoelectronic applications, the bandgap of photoactive semiconductors is often critical to device performance—it determines the upper limit of the energy conversion efficiency in solar cells[44], or the color of emission in light

emitting diodes[45,46]. The color tunability is applicable to metal halide perovskites with different cations, such as $CH_3NH_3PbX_3$ ($MAPbX_3$ in Figure 1-5c) [42] and $CH(NH_2)_2PbX_3$ ($FAPbX_3$ in Figure 1-5d) [43]. By changing the cations, the bandgaps are changing slightly. Therefore, the bandgaps can be slightly tuned by mixing the cations.

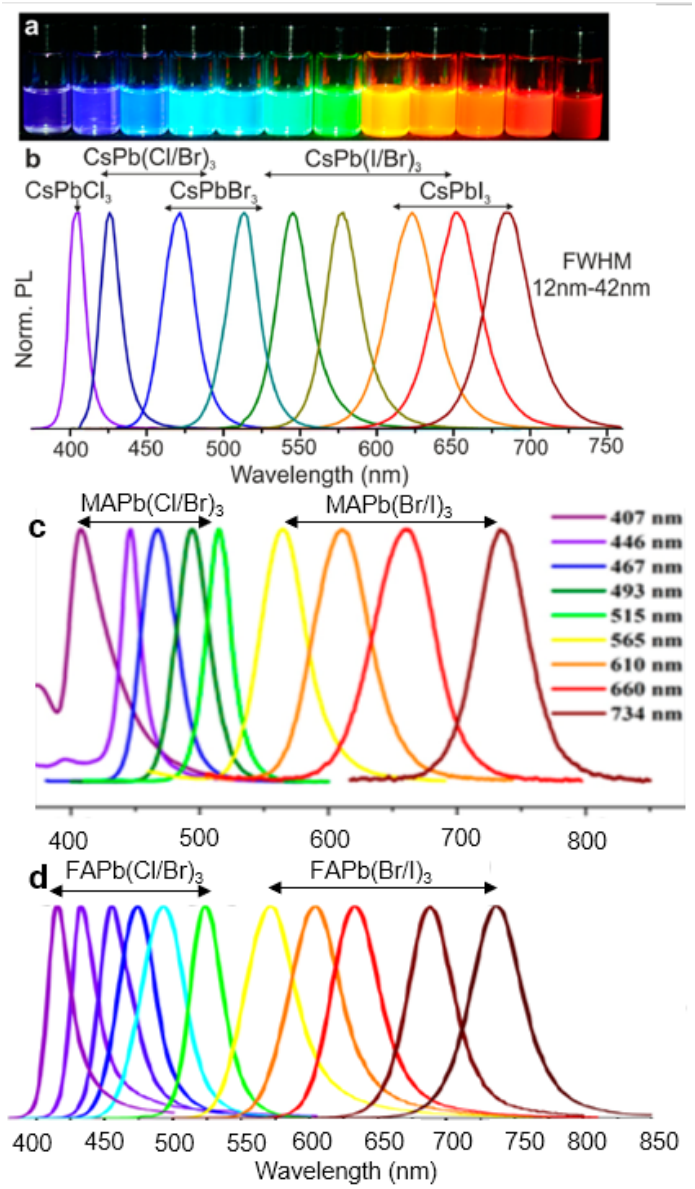

Figure 1-5 The bandgaps of halide perovskites can be tuned by mixture of halide anions. (a) Photographs of $CsPbX_3$ nanocrystals under mixed daylight and UV excitation. (b) Survey PL spectra of $CsPbX_3$ nanocrystals. (c) When the cation changed to MA^+ ($CH_3NH_3^+$), the tuned bandgaps slightly red-shifted to lower energy. (d) PL spectra of FA^+ ($CH(NH_2)_2^+$) based mixed-halide perovskites. (a-b) is adapted with permission[40]. Copyright 2015 American Chemical Society. (c) is adapted with permission[42]. Copyright 2015 American Chemical Society. (d) is adapted with permission[43]. Copyright 2017 American Chemical Society.

The practical value of the bandgap tunability in perovskites, however, had been limited due to poor material stability under optical illumination[10,47-52]. While the freshly prepared mixed-halide perovskites exhibited homogenous crystal phases, the bandgap could vary significantly under continuous optical illumination. The details about the bandgap instability will be discussed in Chapter 3.

1.1.2 Soft ionic lattices of halide perovskites and ion migration

When there is a bright side, there will be a dark side. The soft ionic nature of halide perovskite lattices is a double-sided sword. It is responsible for screening of charge carriers to suppress recombination. But the highly mobile ions lead to various unusual optoelectronic behaviors of devices made of halide perovskites which are closely related to the stable operation of applicable optoelectronics. Efforts in research about ion migration have been put by many research groups worldwide, including GAO's group at FSU (my Ph.D. group). In this session, I will introduce the related phenomena support ion migration in halide perovskites. The governed principles about ion transport in perovskite about the intrinsic factors will be discussed.

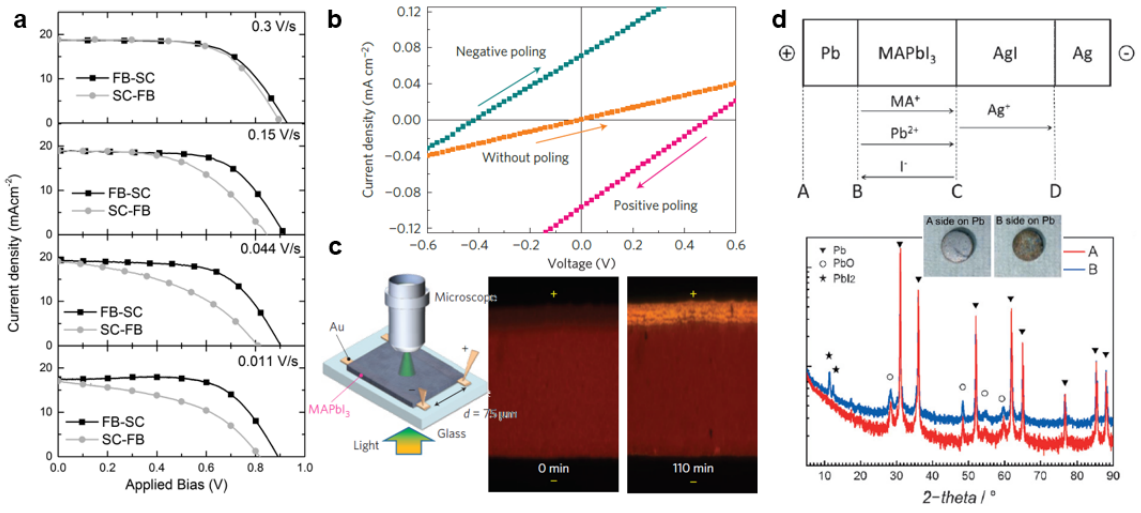

Figure 1-6 Ion migration in halide perovskites. (a) Scanning rate dependent current-voltage curves. (b) Switchable PV effect in symmetric devices. (c) Composition and morphology changes during poling of a lateral device. (d) Conduction of I^- in Pb|$CH_3NH_3PbI_3$|AgI|Ag cell under electrical bias. It's a proof of ion (I^-) conduction in pellet samples under applied voltage (positive at Pb). (a) is adapted with permission[9]. Copyright 2014 American Chemical Society. (b-c) is adapted with permission[56]. Copyright 2014 Nature Publishing Group. (d) is adapted with permission[57]. Copyright 2015 Wiley-VCH.

Followed by the development of solar cell devices, hysteresis in the current-voltage (I-V) curves was reported. The I-V curve showed a loop in which current is a function of voltage scanning direction (Figure 1-6a) [9]. The scanning rate also affects the magnitude of the I-V loop. Researchers were debating about the origins responsible for such I-V hysteresis. Ferroelectricity and ion migration are the two hot topics discussed the most. For the ferroelectricity was reported frequently in oxide perovskite such as BiFeO3 with spontaneous polarization due to a polar distortion of crystal structure[53]. The dipole moment of the polar $CH_3NH_3^+$ cation was hypothesized to contribute to ferroelectricity when $CH_3NH_3^+$ cations are aligned in switchable ferroelectric domains[54]. The hypothesis of ferroelectricity in $CH_3NH_3PbI_3$ was not supported by other simulations nor experiments. The $CH_3NH_3^+$ cations prefer to randomly oriented at room temperature[55].

On the other hand, ion migration has been proved in halide perovskites with various experimental designs[27,56,57], as well as calculations[58]. The report that brought ion migration to the spotlight is published by Huang's group[56]. Switchable photovoltaic effect was reported (Figure 1-6b). Photocurrents of the device before and after negative and positive poling for a single cell were measured under 0.25 sun illumination. The history of electric biasing poling determined the polarization of current in the post-bias condition. The photovoltage resulted from the poling effect is independent of electrodes distance. At the same time, no ferroelectric polarization was detected from the devices both at room temperature and cryogenic temperature (77 K). The operating history dependent I-V relation was diminished at low temperature (~ 250 K). The phenomena introduced above pointed to the conclusion that ion migration in halide perovskites dominates over both ferroelectricity and trapping. Another supportive evidence for ion migration is the observation of composition and morphology changes during electrical biasing of a lateral device. The device was intentionally poled (electrical bias) for a much longer time (2 h). The original brown film became transparent at the anode (Figure 1-6c). The change of morphology at the area close to anode is also obvious, indicating ionic reaction. The drifting of vacancy ions (such as V_{Pb}^{2-}, V_{MA}^{-}) with the accumulation at the anode might be responsible for such electrochemical reaction. Experimental evidence for iodine migration was also obtained by designing galvanic cells (Figure 1-6d) based on $CH_3NH_3PbI_3$ ($MAPbI_3$) [57]. The ion conductivity was measured and visualized. By using electron and ion selective contacts, PbI_2 formation at the Pb/perovskite interface because of I^- migration or $CH_3NH_3^+$ drifted to the opposite direction with positively poling at the Pb

electrode. The transport of ions in halide perovskites was reported to be active. Ion diffusivity as high as 10^{-7} cm^2 s^{-1} have been reported at room temperature.

The diffusivity might be higher if the material is highly defective. Solid-state diffusion is often mediated by defects in lattices, for example, site vacancies and interstitials. Low energy defects in halide perovskites were reported by first-principles calculations, similar to what I have mentioned previously in 1.1.1 and Figure 1-3. Vacancies and interstitials, among all the defects, would commonly mediate ion diffusion as have shown in Figure 1-7. The calculated activation energy for vacancy mediated iodide diffusion is only 0.6 eV or below[60-62]. The energy for $CH_3NH_3^+$ diffusion is only 0.8 eV. Thin films with grain boundaries would have lower barriers (lower activation energy) for ions to migrate where point defects density is usually high at the boundaries and surfaces with dangling bonds, lattice dislocation, and lattice distortions. The grain boundaries in polycrystalline thin films are like expressways to mobile ions. When a device is under operating condition, the electric field will provide extra energy for the ions to migrate. Global ion migration with the modification of internal electric field both at the contact interfaces and bulk was observed. Details about the microscopic studies are described in Chapter 2.

Ion migration exists in halide perovskites. The ability of defects to migrate, on the other hand, depends on available migration paths. Therefore, it is related to defect states, which are highly

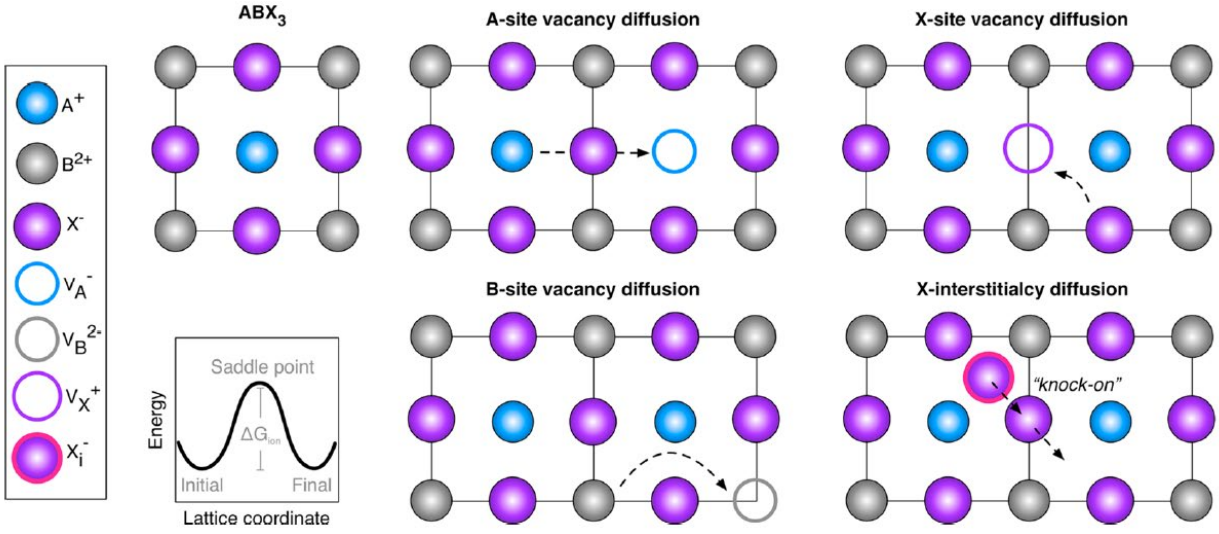

Figure 1-7 Possible ion migration pathways in halide perovskites. is adapted with permission[59]. Copyright 2018 American Chemical Society.

sensitive to synthesis methods. Synthesis methods determine the defect states, including types of

defects and density. The first is influenced by processing conditions such as stoichiometry and crystal growth processes. Additionally, the feasibility of creating defects can be described thermodynamically. The lower the so-called formation energy, the more likely it is to obtain a higher equilibrium concentration of thermally generated defects. The ion migration in materials prepared by different methods was part of my Ph.D. work, which is included in Chapter 2.

Ion migration is not a surprise in perovskite systems. But the migration in some degrees is reversible due to the high tolerance of halide perovskite lattices.

1.1.3 Phase instability of halide perovskites

The other very interesting phenomenon related to ion migration in halide perovskites is the photoinduced phase separation in mix-halide perovskites. Halide perovskites offered a facile approach to tune the bandgap across a wide energy range by accommodating two types of halogen anions in a solid solution—the so-called mixed-halide perovskites (Introduced in 1.1.1 and Figure 1-5). Performance of optoelectronic devices depends highly on the bandgap energy of the photoactive components[44,63]. However, the tuned bandgap in mixed-halide perovskites is known to be unstable. While the freshly prepared mixed-halide perovskites exhibited homogenous crystal phases, the bandgap could vary significantly under continuous optical illumination. An additional PL peak positioning at low energy (in $CH_3NH_3PbBr_xI_{3-x}$, new PL peak is at 1.68 eV) continuously grows under illumination at room temperature (continuous 457-nm light source, 15 mW cm^{-2}), and the original PL peak gradually disappeared (Figure 1-8a). Split X-ray diffraction patterns were observed (Figure 1-8b)[10]. Various measurements indicated that the observed bandgap shifts could be attributed to photoinduced phase separation[10,47-50] -- the homogeneously distributed halogen anions segregated into bromine- and iodine-rich domains (Figure 1-8c).

It's worth noting that the position of this new peak is independent of halide composition and bandgap (Figure 1-8d)[10], indicating the iodine-rich domain is the stable state, with respect to other compositions. The other interesting phenomenon is the reversibility of phase separation. After resting in the dark for an elongated time, the PL will resume back to the original position and goes through the phase separation again under continuous illumination, even after several cycles (Figure 1-8e).

Though the phenomena themselves are very interesting, the bandgap shift would be particularly detrimental when photoresponse of perovskite-based optoelectronic devices needs to be tailored toward specific spectral ranges. Fortunately, the phase separation can be substantially suppressed

when nanocrystals of the mixed-halide perovskites $CsPb(Br_xI_{1-x})_3$ were embedded in an endotaxial

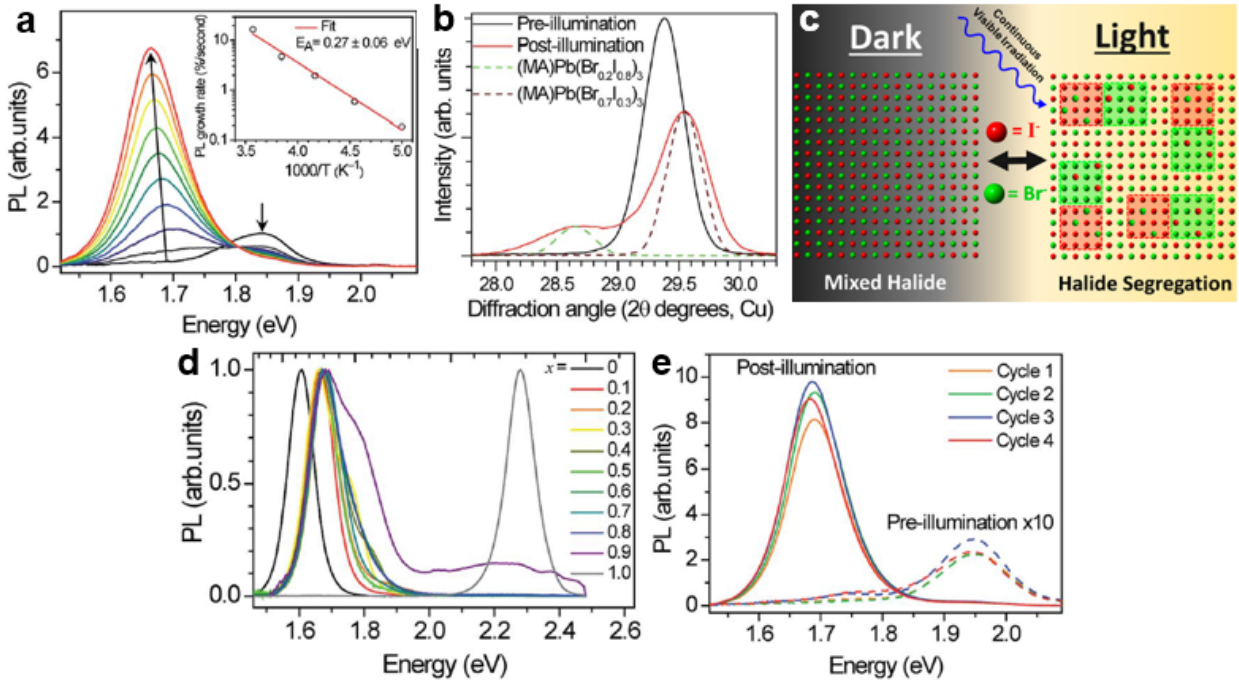

Figure 1-8 Phase separation in mixed-halide perovskites. (a) PL of $CH_3NH_3Pb(Br_{0.4}I_{0.6})_3$ over 45 seconds with 5 seconds interval PL collection under 457-nm illumination (15 mW cm^{-2}). temperature dependence of initial PL growth rate (b) The 200 XRD peak of an $CH_3NH_3Pb(Br_{0.4}I_{0.6})_3$ film before (black) and after (red) white-light soaking for 5 minutes at 50 mW cm^{-2}. The dash lines are the XRD patterns of an $CH_3NH_3Pb(Br_{0.2}I_{0.8})_3$ (dashed green) and an $CH_3NH_3Pb(Br_{0.7}I_{0.3})_3$ film (dashed brown) (c) Schematic showing the homogeneous mixed state in the dark and phase segregated into Br-rich and I-rich domains under illumination with perovskite materials X = 0.5. (d) Normalized PL spectra of $CH_3NH_3Pb(Br_xI_{1-x})_3$ thin films after illuminating for 5–10 minutes. (e) PL spectra of $CH_3NH_3Pb(Br_{0.4}I_{0.6})_3$ thin film after sequential cycles of illumination for 2 minutes (457 nm, 15 mW cm_2) followed by 5 minutes in the dark. (a)(b)(d)(e) are reprinted from Ref [10]. (c) Adapted with permission[52]. Copyright 2017 American Chemical Society.

matrix $Cs_4Pb(Br_xI_{1-x})_6$. The study about the origin of the phase separation in the thermodynamic aspect and the solution for this issue will be discussed in detail in Chapter 3.

The phase instability, attributing to the thermodynamic origin, is a problem in some of the uni-halide perovskites (containing a single type of halogen). $CsPbI_3$, in its perovskite phases (either with the high-symmetry cubic lattices or the relaxed tetragonal/orthorhombic lattices), was considered highly promising for photovoltaic applications[66]. According to the Shockley-Queisser limit[67], the suitable bandgap energy (1.75 V) makes $CsPbI_3$ ideal for either single-junction solar

cells or the top-cell in Si-based tandem cells[66]. However, $CsPbI_3$ can transit spontaneously to a so-called δ-phase (Figure 1-9a) [65]. $CsPbI_3$ in this phase, with a non-perovskite orthorhombic lattice structure, appeared neither electrically nor optically active for optoelectronic applications[68].

It has been reported recently that $CsPbI_3$ in form of nanocrystals could be fixed in its perovskite phase[69]. The phase stability, however, could be compromised when the small grains of $CsPbI_3$ quickly merged into larger ones[70]—a typical behavior shared by other perovskite nanocrystals discussed above. These phenomena together pointed to the composite structures as a logical solution to obtaining useful perovskite $CsPbI_3$.

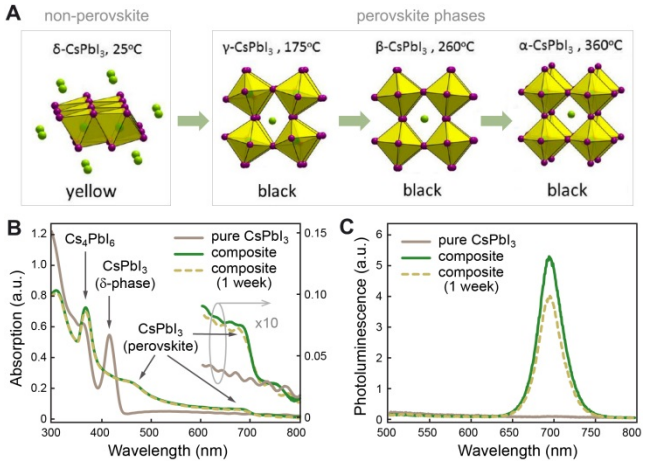

Figure 1-9 (a) Crystal structure of $CsPbI_3$ in non-perovskite and perovskite phases. (b)-(c) Optical absorption and photoluminescence spectra show improved phase stability of the perovskite $CsPbI_3$ in composite thin films. (a) Adapted with permission[65]. Copyright 2015 American Chemical Society.

Stabilization of the perovskite phase $CsPbI_3$ has been achieved recently in our laboratory using the $CsPbI_3/Cs_4PbI_6$ composite, which project I was involved. Similar to the case of mixed-halide perovskites[13], the composite of $CsPbI_3$ nanocrystals embedding in the Cs_4PbI_6 matrix was obtained using thermal evaporation. Optical absorption edge and peak were observed at 700 nm and 368 nm, corresponding to the bandgap energy of $CsPbI_3$ (in its perovskite phase) and Cs_4PbI_6, respectively (Figure 1-9b). The strong PL near 697 nm also verified that a significant amount of $CsPbI_3$ was retained in its perovskite phase in the composites (Figure 1-9c). Alternatively, in the composites containing minimal Cs_4PbI_6, almost all of the $CsPbI_3$ settled in its non-perovskite δ-phase (corresponding to the optical absorption around 417 nm), with no absorption or photoluminescence spectral features corresponding to the perovskite $CsPbI_3$. Compared with the

PL from bulk whose center is around 709 nm[71], the $CsPbI_3/Cs_4PbI_6$ composite with PL centered at 697 nm, showed weaker confinement, indicating the small size of confined $CsPbI_3$. The small size estimation with large surface-to-volume ratio is consistent with dominancy from the interfacial effect. The correlation between the optical properties, the compositional ratio, and the microscopic morphology indicated that the crystal phase of $CsPbI_3$ was dictated largely by the size of the crystalline domains and the host-guest interfaces. Such phase manipulation appeared to be quite sustainable with minimal spontaneous phase transition observed over the course of weeks (dashed line in Figure 1-9b and c).

Besides the phase stability, the optical properties of $CsPbI_3/Cs_4PbI_6$ composite were studied roughly during my Ph.D. work. This work hasn't published yet and this project is led by another graduate student. The details will be skipped in this dissertation.

1.2 Conclusions and future remarks

The appealing optical and electrical properties of halide perovskites, with the low-cost advantages, earth-abundant elements, will make them very useful materials for potential highly-efficient optoelectronics. Though there are some drawbacks, with all the efforts invested now and in the future by scientists, I believe these series of materials would be very promising to fulfill the requirement for marketing in the near future.

CHAPTER 2
SCANNING PROBE MICROSCOPIC STUDIES ON HALIDE PEROVSKITES

2.1 Introduction

Organic-inorganic hybrid metal halide perovskites have recently emerged as a highly promising class of optoelectronic semiconductors, as introduced before. Despite the successful demonstration of the devices by far, unusual electronic behaviors such as the current-voltage hysteresis and the switchable photovoltaic effect[4], introduced in Chapter 1, have not been fully understood. Devices with these behaviors may exhibit variations in performance, especially during extended operation[72]. Given the strong correlation between the electronic material properties and the optoelectronic device performance, there is a pressing need for understanding the mechanisms behind the dependence of charge transport behaviors on the operating history of the devices.

Ion migration has been proposed to be one of the major factors responsible for the commonly seen *I-V* hysteresis and the temporal evolution of the current-to-photon efficiency as (details in Chapter 1). Previous work investigating the effects of applied biases was often carried out in packaged devices where the results are likely convoluted given the presence of charge transport materials other than the photoactive perovskites[73-76]. The microscopic pictures about the actual changes are in absent, for example, how the actual internal electric field is changing with the external stimulation. In my work, microscopic pictures of electronic evolution intrinsic to the hybrid perovskites using scanning laser microscopy were obtained. Distinct from the previous studies that attempted to visualize the uneven distribution of chemical compositions or photoluminescence[77-79], our method provides spatial-resolved electric fields which directly dictate the charge transport behaviors of these photoactive semiconductors. The electric fields across the perovskite thin films are found to be unevenly tuned under applied biases, which indicates the accumulation of space charges. The bias-induced space charges are persistent with slow dissipation kinetics after the bias is removed, showing that the reconfigurable electric fields observed here are not purely electronic. The phenomena agree well with the expectations from field-assisted ion migration which can essentially dope the semiconductor and form dynamic electronic (p-n) junctions. Interestingly, we found that such bias-induced dynamic behaviors can be effectively suppressed in samples

processed at elevated temperature, offering a means to create hybrid halide perovskites with stable and reliable charge transport properties during extended device operation.

2.1.1 Scanning photocurrent microscopy

Before discussing the details of this project, I want to introduce briefly the major tools that I have used. One of the major tools used in this work is scanning photocurrent microscopy, in short SPCM. SPCM is a powerful tool for the investigation of spatially resolved optoelectronic properties of semiconductors and microscopic structures.

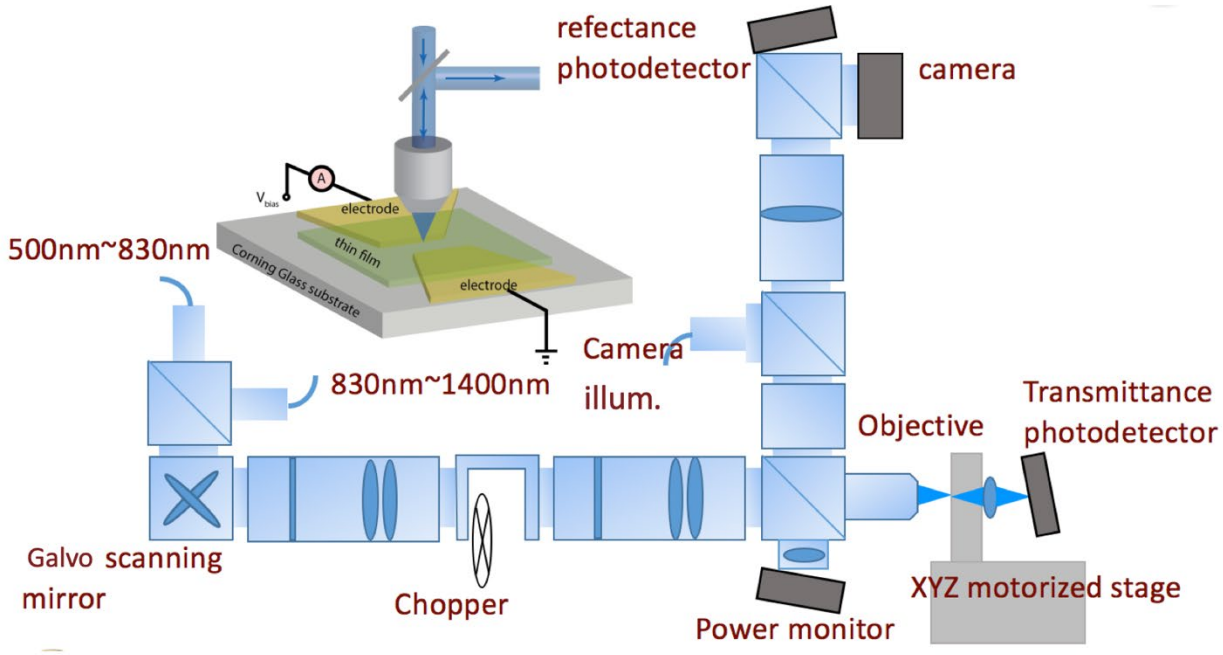

Figure 2-1 Schematic diagram of scanning photocurrent setup. The inset is the simplest version of the device structures with electric measurement elements (two-terminal devices).

2.1.1.1 Experimental setup

The experimental setup of SPCM is home-made as shown in Figure 2-1, with a typical device configuration shown in the inset of Fig. 2-1. SPCM measurements were performed using a confocal microscope to focus light onto a sample mounted on a motorized XYZ stage. A laser beam tightly focused using a 50x objective lens (50x Mitutoyo Plan Apo Infinity Corrected Long WD Objective) was raster scanned along the films while the photocurrent was measured under applied bias. The illumination is from a supercontinuum laser filtered by an acousto-optic tunable filter (AOTF). The scanning is controlled by a pair of electronically controlled X-Y Galvo mirrors (Thorlabs, GVS012). The photocurrent generated in the sample is measured by a Keithley 4200-

SCS Parameter Analyzer with preamps mounted in four channels. The reflection and transmission of light are collected by Si/InGaAs photodiodes whose electric signals are also collected by the Keithley 4210-SCS. The controls of mirrors and other equipment are facilitated by a LabVIEW program. All the outputs are then recorded by the same LabVIEW program, with generation of a synchronous map of the photocurrent and the reflection/transmission. In some experiments, a chopper/vibration of mirrors with a fixed frequency is used to enhance the signal to noise ratio in the frequency range of Hz to kHz. Theories on the Charge Transport and Recombination under Local Excitation.

The analysis of SPCM data is often not trivial as the observed photocurrent can originate via several different mechanisms[80]. The essence of the understanding of data generated by the SPCM technique is a model of the generation, subsequent motion and collection of locally injected free carriers in the structure being studied. The necessary equations are well established for bulk semiconductor materials and serve as the basis for analysis in SPCM experiments.

In SPCM, a focused laser is used to excite excess carriers in a semiconductor device locally. By moving the position of the light beam, changes in current are recorded. To describe the behavior of non-equilibrium excess charge carriers, one can begin with the charge continuity equation

$$\frac{1}{e}\frac{\partial \rho}{\partial t} = G - R - \frac{1}{e}\vec{\nabla}\cdot\vec{J} \ldots\ldots (2.1)$$

where ρ is the charge density, G is the carrier generation rate, R is the carrier recombination rate, e is the positive fundamental electronic charge and $\vec{J}$ is the current density. In the limits of extrinsic doping and low carrier injection, the photocurrent is dominated by the minority carriers. Here, for the sake of simplicity, we choose holes as the minority carriers. The recombination term R can be expressed as:

$$R = \frac{\Delta p}{\tau_h} \ldots\ldots (2.2)$$

where Δp is the density of photo-excited density of holes and τ_h is the recombination lifetime. We assume the photoexcitation is a delta function, i.e., only one point. Outside of the excited point, the generation rate $G = 0$. The continuity equation becomes:

$$\frac{\partial p}{\partial t} = -\frac{\Delta p}{\tau_h} - \frac{1}{e}\vec{\nabla}\cdot\overrightarrow{J_h} \ldots\ldots (2.3)$$

$$\overrightarrow{\mathrm{J_h}} = \mathrm{pe}\mu_\mathrm{h}\vec{\mathrm{E}} - \mathrm{eD_h}\vec{\nabla}\mathrm{p} + \sigma S\vec{\nabla}T(x) \ldots\ldots (2.4)$$

$$\mathrm{D_h} = \frac{k_B T}{e}\mu_h \ldots\ldots (2.5)$$

where μ_h is the hole mobility, $\vec{E}$ is the electric field and D_h is the hole diffusion coefficient. $\sigma S\vec{\nabla}T$ is the current term due to emf generated by thermopower with σ being the electrical conductivity, S being the Seebeck coefficient and $T(x)$ is the temperature distribution on the material. For most semiconductor materials, the drift and diffusion current dominate the photoresponse. Thus, in Eq. 2.4, the dominant terms are the first two terms.

2.1.1.2 Extracting diffusion length in one-dimensional system

When the electric field in the semiconductor is zero (assuming diffusion current dominate), Eq. 2.3 has been reduced to

$$\frac{\partial p}{\partial t} = -\frac{\Delta p}{\tau_h} + D_h \frac{\partial^2 \Delta p}{\partial x^2} \ldots\ldots (2.6)$$

In the steady state, $\frac{\partial p}{\partial t} = 0$ which will lead to

$$0 = -\frac{\Delta p}{\tau_h} + D_h \frac{\partial^2 \Delta p}{\partial x^2} \ldots\ldots (2.7)$$

with the assumption that the excitation point is $x = 0$, the solution in the range $x > 0$ is

$$\Delta p = \Delta p_0 e^{\frac{-x}{L_h}} \ldots\ldots (2.8)$$

where Δp_0 is the photo-excited density of holes at $x = 0$ and L_h is the hole diffusion length. Here $L_h = \sqrt{D_h \tau_h}$. Thus, the current density can be expressed as:

$$\overrightarrow{J_h} = -eD_h \frac{\partial \Delta p}{\partial x} \propto e^{\frac{-x}{L_h}} \ldots\ldots (2.9)$$

The current density decays exponentially from the excited point with a decay length equal to the minority carrier diffusion length.

2.1.1.3 Probing internal electric field

If an electric field exists, the drift current can be comparable to the diffusion current or even dominant. We define electric field that makes the drift current of holes and diffusion current of holes equal as E_c. The diffusion current is $eD_h \frac{\partial \Delta p}{\partial x} \approx eD_h \frac{\Delta p}{L_h}$ and the drift current is $e\Delta p \mu_h E$. E_c can be described as:

$$E_c = \frac{k_B T}{e L_h} \ldots\ldots (2.10)$$

When $E > E_c$ is satisfied, the drift current is dominant. In the presence of strong electric field, the photogenerated electrons and holes are efficiently separated and the spatially resolved photocurrent can be used to map local electric field distributions.

The sources of electric field can be heterojunctions, Schottky contacts, local charge accumulation, defects and externally applied electric field by source-drain voltage or gating voltage[81,82]. The location of photocurrent spots gives indications of spatial distribution of electric field. The sign of the photocurrent indicates the direction of electric field and the magnitude is proportional to the strength of electric field. Such distribution can provide information such as the band bending in a metal-semiconductor interface[83,84].

2.1.1.4 Other applications

SPCM can also be used to probe doping concentration. Gradually change in doping concentration will lead to the spatially resolved voltage distribution. Based on spatially resolved photocurrent and its corresponding integration, Lauhon's group[85] in Northwestern demonstrated the measurements of doping gradient profile in n-type Si nanowires using SPCM with the assumption of drift current domination.

In some cases, the thermoelectric effect is overwhelming the drift and diffusion current, such as photothermoelectric effect in graphene 2D materials. Xu et al used SPCM to study the photocurrent generation mechanism in the interface between 2-layer graphene and single-layer graphene devices by comparing the polarity of the photocurrent spots to the gate-tuned position of the Fermi level[86]. They've shown the Seebeck coefficient correlated to the photocurrent.

Equipped with a super-continuous laser, the barrier heights of Schottky contacts between metal contacts and semiconductor devices can be measured by internal photoemission in SPCM. The illumination at the metal-semiconductor interface with sub-bandgap photons will generate a photocurrent dominated by internal photoemission of hot electrons/holes. By analyzing the dependence of photocurrent yield on photon energy, the barrier height is able to be extracted quantitatively[87].

In conclusion, SPCM is a powerful experimental method to gain a wealth of information including optoelectronic parameters, interfacial properties, charge transport and recombination in semiconductor devices.

2.1.2 Kelvin probe force microscopy

The other major tool I have used in this project is Kelvin probe force microscopy (KPFM), which is an extended function of Atomic Force Microscopy. KPFM measurements in my experiments were carried out using commercial atomic force microscopy (AFM) system (Bruker Dimension Icon, equipped with Amplitude Modulated-KPFM module). The AFM is enclosed in a metal case

which was purged with pure nitrogen gas to provide chemically inert atmosphere. The surface potential was mapped in the dark using a platinum-iridium coated Si probe (SCM-PIT-V2) with a tip radius of 20 nm, a probe-sample distance of 30 nm, and a scan rate of 0.4 Hz. The laser spot used for the AFM feedback loop is shifted away from the very end of scanning tip to avoid photocurrent induced by the laser illumination during the measurements.

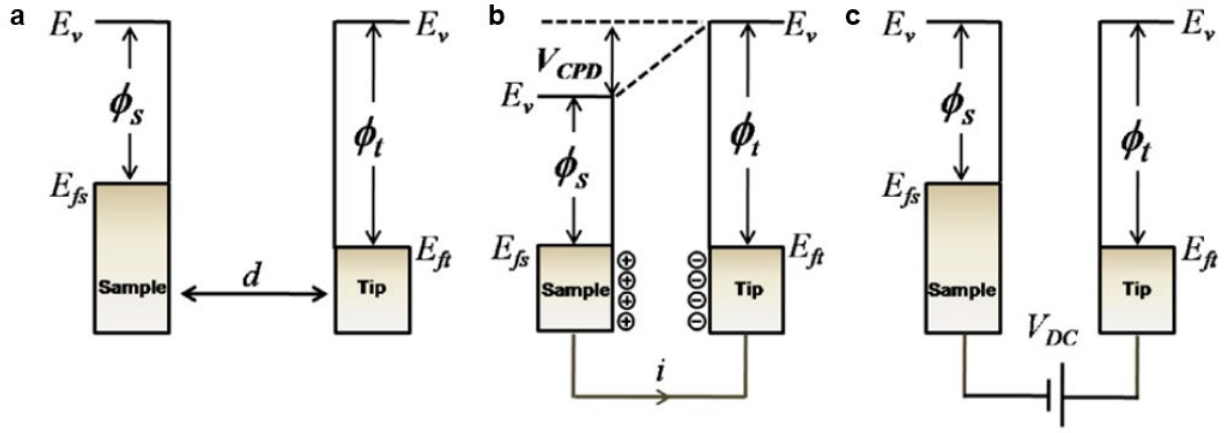

Figure 2-2 Electronic energy levels of the sample and tip for three cases. (a) Long distance, no interaction (b) in electrical contact (c) with an external bias (V_{DC}) applied. E_v is the vacuum energy level. E_{fs} and E_{ft} are Fermi energy levels of the sample and tip, respectively. Adapted with permission[88]. Copyright 2011 Elsevier B.V.

Basically, it's a tool to measure the local contact potential difference (CPD) between a conductive AFM tip and the surface of interest, defined as

$$V_{CPD} = \frac{\varphi_{tip} - \varphi_{sample}}{-e} \quad \ldots\ldots (2.11)$$

φ_{tip} and φ_{sample} and the work functions of the tip and sample, e is the electronic charge. Figure 2-2 describes how the electronic levels aligned one the tip is brought close to the sample. With an external bias V_{DC}, the CPD between tip and sample are null. The V_{DC} is equal to the CPD and the surface potential can be probed.

To acquire accurate data of surface potential, the samples mapped by KPFM were not encapsulated with the PMMA layer. A Keithley 2400 source-meter unit was used as the voltage source and provided external biases between the Au electrodes during the bias-dependent measurements. The spatial-resolved electrostatic potential allowed us to determine the distribution of the local electric field $E(x) = dV(x)/dx$.

2.2 Experimental results of organic-inorganic hybrid perovskite $CH_3NH_3PbI_3$

2.2.1 SPCM and KPFM on solution processed $CH_3NH_3PbI_3$

2.2.1.1 Preparation of CH3NH3PbI3 thin films by Solution synthesis

Solution synthesis of perovskite thin films was carried out following the one-step spin-casting method reported previously[56]. Lead acetate ($PbAc_2$) was purchased from Sigma-Aldrich. Methylammonium iodide (CH_3NH_3I) was prepared by mixing the methylamine (CH_3NH_2) solution (33wt% in absolute ethanol, Sigma-Aldrich) with equimolar hydroiodic acid (HI) (57 wt % in water, stabilized, 99.95%, Sigma-Aldrich), stirred at 0 °C for 2 hours. The precursor solution was prepared in N_2 filled glove box by dissolving 133.2 mg CH_3NH_3I and 102.6 mg $PbAc_2$ in 0.54 ml dimethylformamide (DMF). The glass substrates were pre-patterned with two photolithography defined Cr/Au (5 nm/35 nm) electrodes separated by 20 μm (Figure 1c inset) and treated in UV-ozone plasma for 15 minutes for reduced hydrophobicity. The perovskite precursor solution was then spin-casted onto the glass substrate at 4,000 rpm for 40 seconds in the glovebox. The samples were baked on a hotplate at 95 °C for 15 min to facilitate solvent evaporation and solid film crystallization. After cooling, 10 wt% poly (methyl methacrylate) (PMMA) dissolved in toluene was spin-casted on top at 4,000 rpm for 40 seconds as an encapsulating layer.

2.2.1.2 Material and device characterization

Perovskite-based solar cells with the highest performance are developed and improved based on methylammonium lead triiodide ($CH_3NH_3PbI_3$), modified with the addition of multiple organic cations and a small number of bromine ions (introduced in Session 1.1.1 Tunable bandgap). Given the reported high performance as the photoactive media in efficient solar cells, $CH_3NH_3PbI_3$ is used as the model material in our study. To understand the intrinsic charge transport properties of the perovskites, we adopt a simple device architecture consisting of a $CH_3NH_3PbI_3$ thin film terminated by two Cr/Au electrodes (Figure 2-3c inset). The electrodes are separated by ~20 microns, providing the space for photocurrent mapping along the semiconducting perovskite channel. The $CH_3NH_3PbI_3$ thin films, 80-100 nm thick, were deposited on top of the pre-patterned electrodes (40-nm Cr/Au) using the one-step spin-casting method[89]. The films, after drying and annealing, are in the tetragonal perovskite phase, consistent with the product synthesized using similar recipes reported by others[89] (Figure 2-3a). Also consistent with previous work[38],

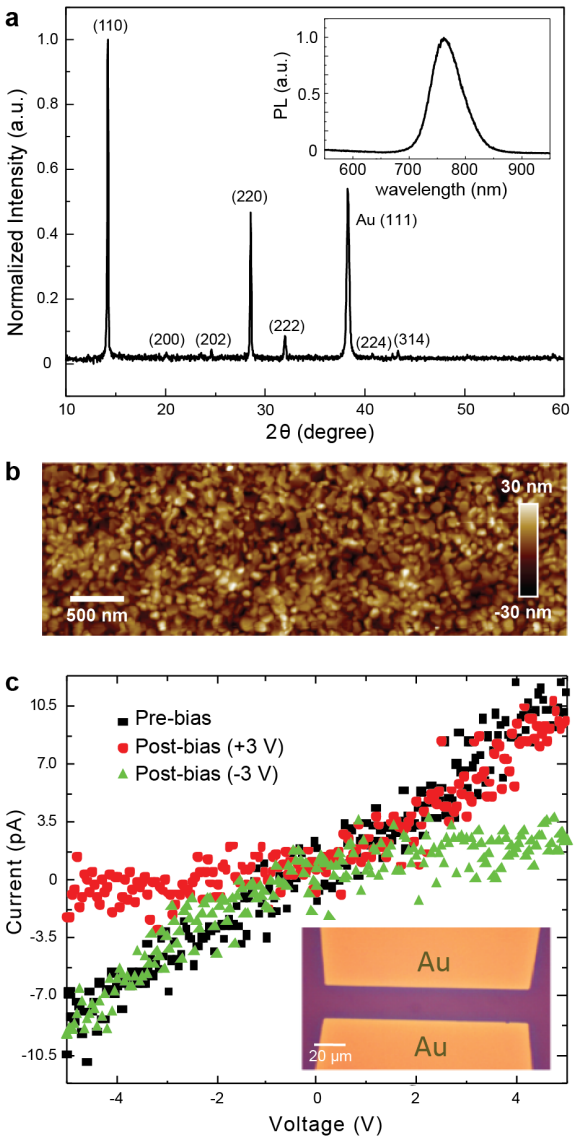

Figure 2-3 Solution-synthesized $CH_3NH_3PbI_3$ exhibits bias-induced I-V rectification. (a) X-ray diffraction (XRD) confirms the tetragonal crystal phase of the $CH_3NH_3PbI_3$ thin films. Photoluminescence from the films shown in the inset centers at 763 nm. (b) The AFM image shows that the thin film is smooth with most grains smaller than 100 nm. (c) A linear I-V curve is observed in a fresh-made sample (black squares) whereas the curve becomes rectified after a +3V (red circles) or -3V (green triangles) bias is applied for 5 min. Inset is an optical micrograph of the two-terminal device. All the I-V measurements were conducted under dark conditions.

$CH_3NH_3PbI_3$ in this crystalline phase produces photoluminescence with a peak around 763 nm (Figure 2-3a inset). With a grain size around 100 nm, the film surface is smooth (image Rq 8.45 nm, Ra 6.72 nm) without obvious pinholes (Figure 2-3b). A layer of ~200-nm thick poly (methyl

methacrylate) (PMMA) is coated on top to encapsulate and protect the perovskite thin films from degradation in ambient water vapor during further optical and electronic characterizations.

The current-voltage (*I-V*) relationships of the devices measured in the dark exhibit dependence on the history of applied biases (Figure 2-3c). A linear *I-V* relation from fresh-made devices indicates that the contacts at the perovskite-Au interfaces are Ohmic (or Ohmic-like). After a 3-V static DC bias was applied for 5 minutes, the *I-V* curve becomes rectified, which may originate from newly formed electronic junctions with space charge regions. Interestingly, the rectification of the *I-V* relationship is reversible. By switching the bias from +3 V to -3 V, opposite rectification is observed in the *I-V* curve, indicating that the polarity of the dynamic electronic junctions may be reversed. Although the device configuration is different, the bias-dependent *I-V* rectification observed here must contribute to the hysteretic charge transport properties in perovskite-based solar cells reported previously[56].

2.2.1.3 SPCM and KPFM on solution-processed CH3NH3PbI3

To uncover the microscopic mechanism of the bias-induced *I-V* rectification, we probed the distribution of the electric field along the perovskite films *in-situ* under controlled biases using scanning photocurrent microscopy (SPCM). A diffraction-limited focused laser beam (with a spot size of 380 nm at 600-nm wavelength) was raster-scanning along the films while the electrical current was measured (Figure 2-1 inset, Figure 2-5a inset). This so-called photocurrent stems from photo-generation of excess charge carriers when the semiconductor is excited by photons with energy above the bandgap. Following the Ohm's law,

$$j(x) = \Delta\sigma(x)E(x) = \Delta n(x)q\mu_q E(x) \quad \ldots\ldots \quad (2.12)$$

the photocurrent $j(x)$ is expected to be proportional to the local electric field $E(x)$. The unit charge q and the mobility μ_q can be considered constant in a uniform film. The dosage of the incident photons is fixed during the measurement so that the photo-generated carrier concentration $\Delta n(x)$ is not a function of position here. Accordingly, it is reasonable to assume the photoconductivity $\Delta\sigma(x)$ remained constant throughout the measurements. In addition, the thin films with fine grains and smooth surfaces minimize the fluctuations of photocurrent at the grain boundaries[90]. The SPCM scans showing features beyond the scale of the crystal domains, therefore, provide reliable tools to visualize spatially the distribution of the electric field along the semiconductor (perovskite) channel[81,82].

The spatial profiles of the photocurrent show that the space charges and the associated electric fields along the perovskite channel can be dynamically formed and tuned by varying the external biases. Before any static biases were applied, (i.e. the pre-bias condition), a fresh-made device exhibits two maxima of the photocurrent (regardless of the sign) near the two Au electrodes (Figure 2-4a, 0 V), which are characteristic of Schottky barriers.[87] The exponential fitting of the two photocurrent peaks shows that the minority carriers have a diffusion length about 5 μm. The existence of the Schottky barriers at the perovskite-Au interfaces is also verified by the internal photoemission current using sub-bandgap optical excitation (Figure 2-4b) [87]. Apparently, the barriers are not high enough to induce rectified *I-V* curves and the contacts in our devices behave Ohmic-like with a linear *I-V* relation in the dark (Figure 2-3c).

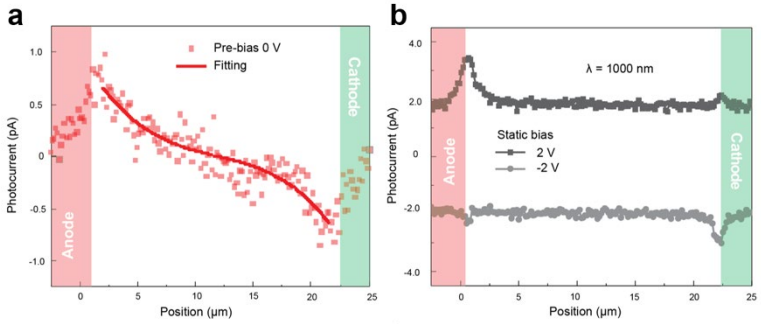

Figure 2-4 Schottky barriers were detected with 0V bias in pre-bias condition. (a) Short-circuit photocurrent exhibits two maxima (positive and negative) near the Au electrodes before any biases were applied. (b) Photocurrent mapping using the below bandgap wavelength λ=1000 nm shows two peaks at the perovskite-Au interfaces with the same polarity which can be attributed to internal photoemission processes from holes and electrons separately at anode and cathode.

When a small static bias is applied (0.5–1.5 V), the photocurrent maximum near the anode increases in amplitude whereas the one near the cathode quickly vanishes (Figure 2-5a and Figure 2-5c). Such changes in photocurrent are likely resulted from the reverse- and the forward-biased Schottky junctions near the two electrodes, leading to the intensified and reduced electric fields, respectively. As the static bias voltage (V_b) is increased, the SPCM peak continues to shift towards the center of the perovskite channel and, in the meantime, becomes broader. When V_b reaches 2 V, the broad photocurrent profile extends almost across the entire perovskite channel from the anode to the cathode. While the broadening effect at this voltage can be explained as the dominating effect from the extended depletion region of the reverse-biased Schottky junction, more unexpected photocurrent features are observed when the bias voltage is further increased.

When $V_b > 3$ V, a new maximum of photoresponse emerges near the cathode, which suggests a large electric field along with steep potential drop in this region. Such confined voltage drop indicates that a more resistive section is present in the perovskite channel, which cannot be simply explained by biased Schottky junctions at the contact. It is worth noting that all the photocurrent profiles under static biases are obtained after the biases have been applied for more than 5 minutes. Equilibrium conditions have been ensured by repeating the SPCM scans. To the best of our knowledge, neither the shifting nor the broadening of the photocurrent profiles observed here was reported previously in other symmetric metal-semiconductor-metal devices regardless of back-to-back Schottky junctions or Ohmic contacts at the electrodes[91].

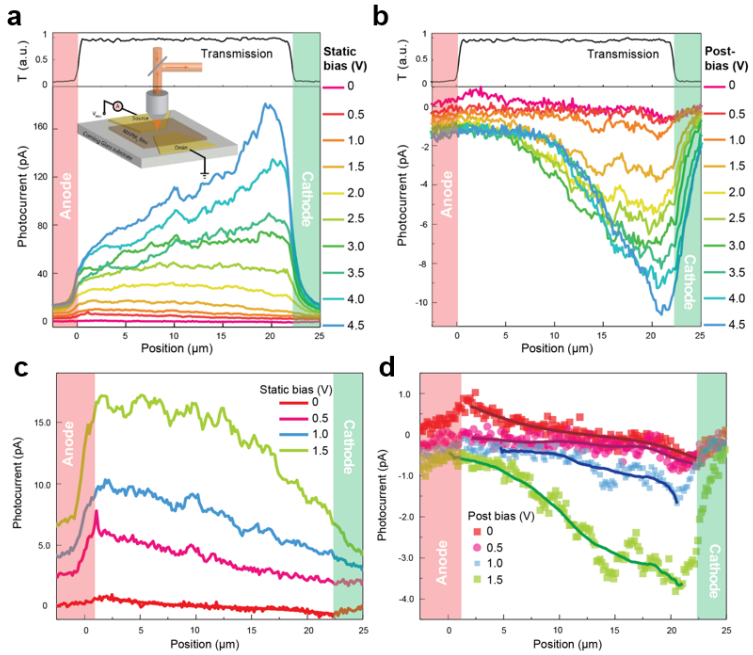

Figure 2-5 The photocurrent maps exhibit significant differences before and after the electric biases were applied (at 295 K). (a) The photocurrent line scans are shown as a function of voltage applied to the left electrode (anode) while the right electrode (cathode) is grounded. The transmission curve indicates the edges of the electrodes. Inset shows the schematics of the SPCM setup. (b) The short-circuit photocurrent after removing the biases is distinct from the pre-bias profile. Intensive electric field confined near the cathode indicates the accumulation of persistent space charges there. (c) Amplified photocurrent profiles with a small static bias applied. The photocurrent maximum near anode becomes more intensive whereas the one near cathode quickly vanishes. (d) Amplified photocurrent profiles in post-bias conditions after a small static bias applied. Post-bias photocurrent profiles are apparently different from the pre-bias situation even in lower biasing range.

Surprisingly, the short-circuit photocurrent measured after the electric bias is removed (post-bias) appears distinct from the one obtained pre-bias (Figure 2-5b and Figure 2-5d). Because the

photocurrent is locally proportional to the built-in electric field in the short-circuit configuration, the post-bias photocurrent profiles explicitly reveal the dynamic formation of the built-in electric-field induced by the extendedly applied bias. The persistent built-in electric-field implies a non-electronic nature of the bias-dependent charge transport reported in perovskites. The curved tails that broaden the photocurrent peaks can be attributed to the long carrier diffusion length (Figure 2-6) which are well fitted by a single exponential decay with about 5 μm diffusion length. Compared with the pre-bias photocurrent, the peak near the anode disappears in the short-circuit photocurrent taken right after a small bias (0.5 V) is withdrawn, while the other peak close to the cathode remains nearly unchanged. This means the electric-field of the Schottky junction at the anode is weakened by a newly-formed space charge region in this section. After a larger bias (1–3 V), however, the peak of the short-circuit photocurrent becomes significantly higher, indicating that space charges continue to accumulate as the bias voltage is increased. Such short-circuit photocurrent feature is characteristic of the formation of a p-n junction with high

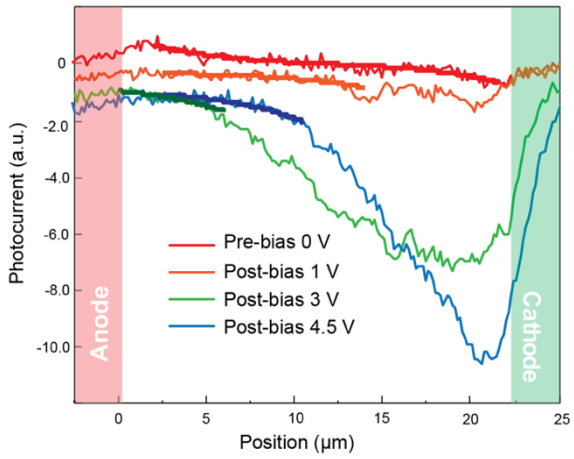

Figure 2-6 The tails of photocurrent profiles in the post-bias conditions can be well fitted with single exponential decay as shown by the thicker lines, indicating the broadening of the photocurrent peaks originates from the long carrier diffusion.

built-in potential in the corresponding region. With V_b exceeding 3 V ($\geq$ 3.5 V), the magnitude of the post-bias photocurrent near the cathode still keeps increasing, while the peak starts to narrow down and shift closer to the cathode. Moreover, the space charges accumulated under the applied biases dissipate slowly within the duration of the SPCM measurements. While kept in the short-circuit condition, the photocurrent profiles captured at different delays show that the residual electric field attenuates with time after the external biases are removed. After 4 V bias is applied

and withdrawn (Figure 2-7), for example, the built-in electric field continues to relax in amplitude for hundreds of seconds. Complete recovery in the dark (back to the pre-bias status) takes more than 20 minutes.

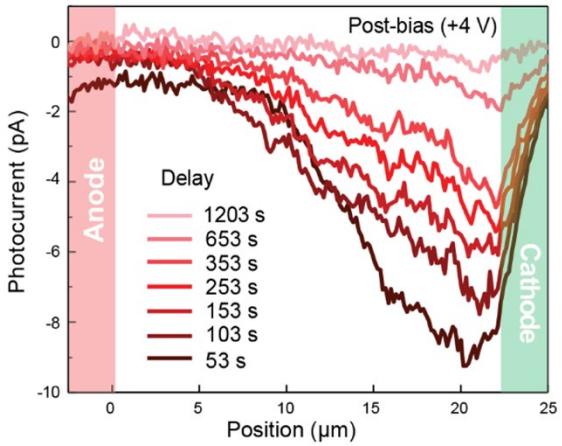

Figure 2-7 The profiles measured after 4 V bias was applied and withdrawn at different delay time show that the post-bias photocurrent relaxes with time.

The evolution of the electric field distribution driven by the applied biases is verified using Kelvin probe force microscopy (KPFM) (Figure 2-8). The surface potential mapped using KPFM in the dark can be used to deduce the local electric field simply based on the relation $E(x)=\mathrm{d}V(x)/\mathrm{d}x$. Without biases applied between the two Au electrodes (Figure 2-8, 0 V), higher potential is observed at the electrode regions, which indicates a higher work function of Au compared with that of the perovskite. Accordingly, the hybrid perovskite under studies here must be p-type in order to form the Schottky barriers with the Au electrodes that can be observed in the SPCM profiles. Under a small bias (Figure 2-8, 0.5 V), the applied voltage drops primarily near the anode where the Schottky junction is reverse-biased, consistent with the SPCM profiles in which a peak of the photocurrent (i.e. the electric field) is observed in the same region. When the bias is increased to 2 V, the potential drops more linearly across the perovskite channel, which agrees with the evenly distributed electric field observed in photocurrent under the same bias voltage (Figure 2-5a and c). The agreement between the KPFM and SPCM measurements is also found at the higher bias (5 V) where a sharp drop of the potential near the cathode corresponds to the high electric field there. Such large slope in electrostatic potential often accompanies the presence of

an electronic junction with unevenly distributed space charges (e.g. p-n junction) [92]. Moreover, corresponding to the slow space charge relaxation observed in the SPCM profiles, the potential profiles from the KPFM measurements also vary slowly after a sudden change of the applied bias. When the anode and the cathode are switched (i.e. reverse the bias from 5 V to -5 V), the section of the rapid potential drop (with larger slope) moves gradually with the anode from the right to the left side of the device (Figure 2-8, inset). Notably, the stabilized KPFM profile with -5 V bias is almost a mirror image of that under 5 V bias. This confirms that all the relevant bias-induced processes, such as accumulation of space charges and formation of built-in electric field, are highly reversible within the range of the biases we applied.

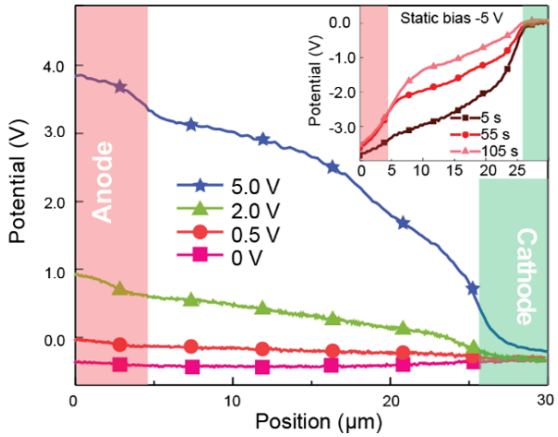

Figure 2-8 Voltage drop from electrostatic potential mapping using KPFM is consistent with the SPCM results. A mirror image of the voltage drop is observed using KPFM when the bias is switched from +5 V to -5 V as shown in the inset.

The dependence of the photocurrent on the biases applied agrees well with predictions from a model based on field-assisted ion migration. Ionic conduction is well documented in oxide perovskites, such as $LaBO_3$ (B=Cr, Mn, Fe, Co), where migration of oxygen ions is believed to be assisted by oxygen vacancies which provide pathways with low energy barriers[93]. Low activation energy of mobile ions is also reported in the organic-inorganic hybrid metal halide perovskites both theoretically[60,61] and experimentally[10,11,27,57]. These mobile ions, in our model, can be driven to migrate by the electric field under externally applied biases, similar to the process of ionic conduction in solid state electrolytes.

Before any external biases are applied, the anions and cations are evenly distributed without unbalanced ionic charges across the perovskite channel (Figure 2-9a). The SPCM profile is

therefore only showing two maxima near the electrodes representing the back-to-back Schottky barriers located at the Au-perovskite interfaces. When an external bias is applied, mobile ions can drift collectively under the applied electric field, leaving behind unevenly distributed space charges. The drift of the mobile ions competes with the back diffusion and reaches an equilibrium that is bias dependent.

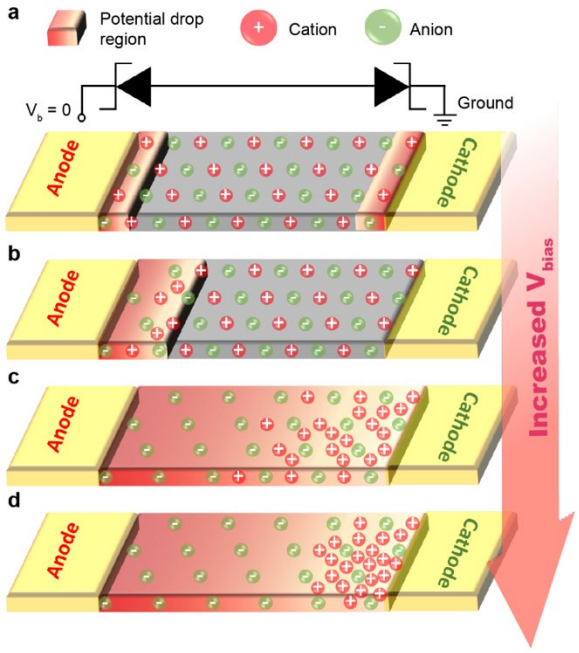

Figure 2-9 Schematic diagrams illustrate the model of field-assisted ion migration in response to electric biases. (a) In the original short circuit condition, there are two back-to-back small Schottky junctions located at the Au-perovskite interfaces. The perovskite material is intrinsic with evenly distributed ions in the lattices. (b) With a small bias, the cations in the depletion region of the reverse-biased Schottky junction migrate with the assistance of electric field. (c) When the bias is increased, the potential drop region is across the entire channel. More cations are moving to the cathode, leaving negative charged vacancies behind. (d) Further increasing the bias can result in more cations migrating toward the cathode, leading to larger and more spatially confined electric field originated from the space charges.

Under low biases ($\leq$ 0.5 V), the Schottky barrier near the cathode is forward biased with reduced electric field, diminishing the photocurrent maxima observed there when no bias was applied. The photocurrent feature near the anode, however, becomes broader with higher intensity, which can originate from the extended depletion width of the reverse biased Schottky junction (Figure 2-9b). When the bias is increased (0.5 V < Vb $\leq$ 3 V) (Figure 2-9c), the electric field under this condition distributes across a large section of the semiconductor channel, resulting in further broadening of

the photocurrent peak. This wide E-field distribution is dominated by the long depletion region under the so-called punch-through condition because of the low carrier concentration[94,95]. Although the voltage could also drop on the series resistance of the channel, the resultant electric field would be constant through the channel and, therefore, is less likely to be responsible for the photocurrent profile presented in Figure 2-9c. Nearly uniform photocurrent between the anode and the cathode is then observed when $V_b \geq 2$ V (Figure 2-5a). The mobile-ion-induced space charges may also contribute to the photocurrent broadening, but is hard to be distinguished from the electronic depletion region extended across the entire perovskite channel under the punch-through condition. As more ions are shifted with the larger biases, higher concentration of space charges can accumulate and be compensated by electrons and holes. This is a process similar to the effective doping caused by mobile ions in ionic transport polymers[92]. The p-doped region near the anode (where excess anions are accumulated) and n-doped region near the cathode (excess cations are accumulated) can eventually approach each other and form an effective p-n junction. The electric field mapped is a combination of the applied external bias and the built-in potential of the effective p-n junction. The doping fronts of both p and n types close to the p-n junction region have lower doping concentration due to lower accumulation of ions. As a result, when the bias exceeds 3 V ($\geq$ 3.5 V), a new maximum can be visualized in the photocurrent profile which corresponds to the high electric field in the depletion region of the effective p-n junction. The location of the photocurrent peak, being closer to the cathode, indicates that the cations ($CH_3NH_3^+$ or the iodine vacancy V_I^+) have higher mobility than the anions in the perovskite we use. The hypothesis of field-assisted ion migration is also supported by the phenomenon of material breakdown under extreme biases. When $V_b > 5$ V, the optical transmission of the 600-nm light increases abruptly near the anode (Figure 2-10). With a large number of cations migrated away from the anode, the perovskites in this region can degrade to PbI_2 which is known to be transparent at this wavelength. The material breakdown triggered by the applied biases can be considered similar to electrochemical reactions at the electrode[78] and irreversible even after removing the external biases.

The phenomena related to ion migration become further evident after the applied bias is withdrawn (i.e. short-circuit condition). Unlike electronic space charges that would return to the original equilibrium instantaneously after an external bias is removed, it takes much longer time for the relocated mobile ions to relax back to the original uniform distribution because the mobility of

ions is typically orders of magnitude lower. Accordingly, the post-bias photocurrent profiles are distinct from the pre-bias ones (Figure 2-5). The p-n junction formed by the bias-driven ion migration is retained after the bias is removed, which can be visualized as the (negative) photocurrent maximum near the cathode that decays slowly. According to the sign of the photocurrent, the material near anode is more p-doped while material neighboring cathode is more n-doped. It is interesting that although the photocurrent maxima near the cathode were not obvious when low biases were applied, the signatures of mobile-ion induced junction (i.e. the photocurrent maxima) can be clearly identified in the post-bias SPCM profiles even though the biases were low (V_b >1.5 V). Therefore, compared with the photocurrent mapped under static biases, transient photocurrent measured post-bias at this timescale provides a more sensitive method to detect the ion migration in halide perovskites. After a higher bias was applied, the peak in the short-circuit photocurrent becomes narrower. This is because higher density of mobile ions is expected to accumulate under higher biases, effectively doping the materials more heavily and reducing the width of the depletion region of the effective p-n junction formed.

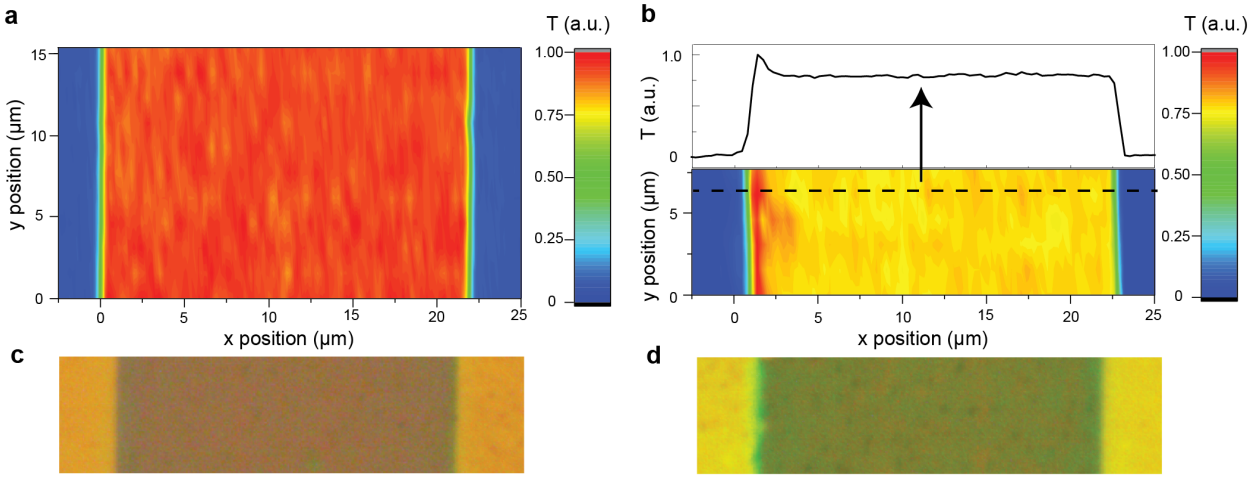

Figure 2-10 The transmission can effectively probe the degradation of materials. (a) Non-degradation samples have uniform transmission with some fluctuations corresponding to film topology. The transmission 2D image is from a sample with 4 V bias voltage on. (b) The degradation of samples under the biases is monitored by the transmission. The increase of the transmission at the anode is from the degradation of perovskite into PbI2 which has a bandgap higher than 600 nm. The upper image is the cross-section from the lower 2D transmission labelled by the dashed line. (c) (d)The corresponding photos were taken separately after the (a) and (b).

The mechanism of ion migration is further verified using temperature dependent photocurrent mapping (Figure 2-11). At reduced temperature (235 K, above the phase transition temperature

165 K from the orthorhombic to the cubic crystal structure[96]), the pre-bias photocurrent shows features of Schottky barriers near the Au electrodes, analogous with those observed at room

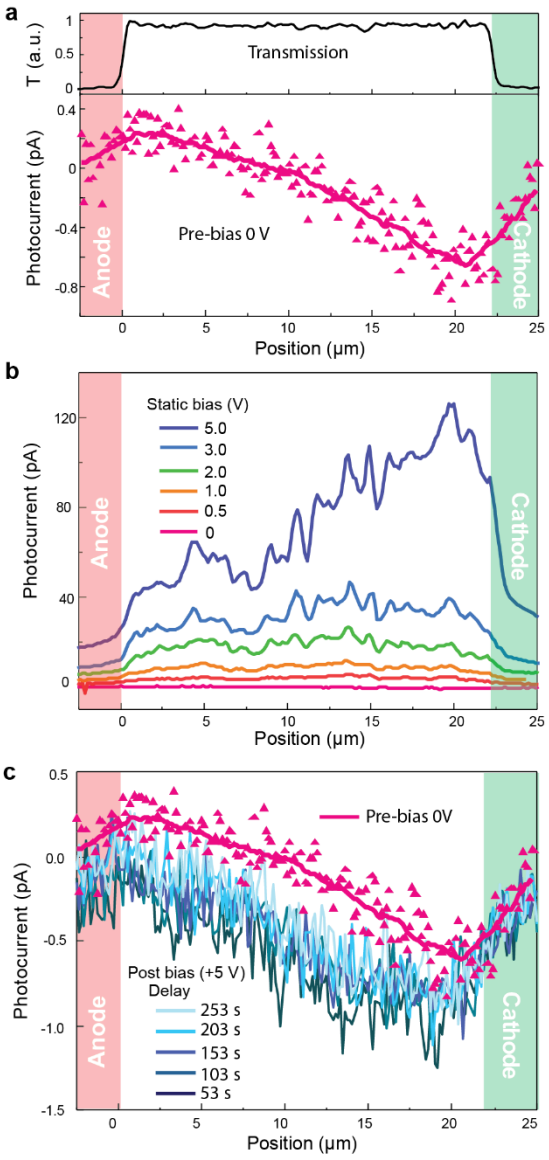

Figure 2-11 Building up of space charges in biased perovskites can be suppressed at reduced temperature (235 K). (a) Features of back-to-back Schottky junctions can still be observed in pre-bias photocurrent. The smaller slope of photocurrent decaying along the channel indicates longer minority diffusion length at reduced temperature. The solid line is extrapolated from the experimental data as a visual guide. (b) The photocurrent profiles obtained at 235K is uniform across the entire channel under low bias voltages (< 3 V). When the static bias is increased to 5 V, a maximum of photoresponse is observed close to cathode, indicating a small number of mobile ions accumulated there. (c) The short-circuit photocurrent starts to exhibit noticeable changes after 5 V biasing. The relaxation of the space charges, however, is much slower at the 235 K compared with that at the room temperature.

temperature (Figure 2-11a). The longer exponential decay towards the center of the perovskite channel can be attributed to an extended minority diffusion length that is expected at lower

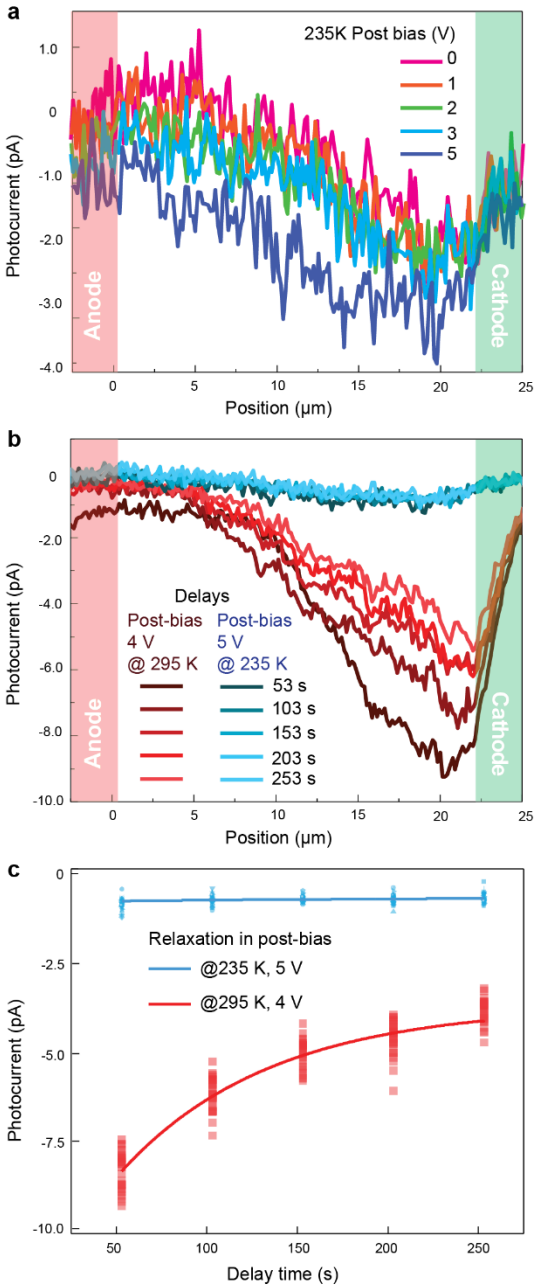

Figure 2-12 Post-bias photocurrent line scans at 235 K exhibit much smaller difference before and after biasing. (a) The photocurrent line scans in the post-bias conditions after different bias voltages are listed. Differences between the post- and pre- bias photocurrent measured at the reduced temperature are not obvious. (b) Compared with the relaxation after applying 4 V bias at room temperature, the relaxation of the post-bias photoresponse at 235 K after 5 V bias has a much smaller amplitude. (c) The relaxation rate in lower temperature is also slower than the situation in room temperature. The solid lines are the single exponential fitting with the relaxation rate 1/92 s-1 at room temperature and 1/1091 s-1 at 235K.

temperature[97]. With lower carrier concentration and higher resistance of the semiconducting perovskites at reduced temperature, the punch-through condition is easily fulfilled between the back-to-back Schottky barriers, resulting in nearly flat photocurrent profile across the channel even at low biases (e.g. 0.5 V) (Figure 2-11b). Unlike at room temperature, the post- and pre-bias photocurrent measured at the reduced temperature do not show obvious differences until a higher bias is applied (Figure 2-12a). When the bias is increased to 5V, the potential drops more in the region closer to the cathode, which is considered as a feature originating from the mobile-ion induced p-n junction. After withdrawing the bias, weak residual electric field is retained at the corresponding region, showing that only a small number of cations get migrated and accumulated near the cathode under high external biases at this reduced temperature. The relaxation of the mobile-ion-induced space charges, after removal of the biases, is slower at 235 K (Figure 2-11c) compared with that at room temperature (Figure 2-12b and c). These comparisons together imply that the ion mobility in the hybrid perovskite decreases with reduced temperature, which is generally expected in ionic conductive solid-state materials[98-100]. It is worth noting that deep-level charge trapping, another mechanism often proposed for the *I-V* hysteresis in perovskite-based solar cells previously, is unlikely responsible for the bias-dependent, reconfigurable space charges observed here. Although the capturing and ionization rates can be lower at reduced temperature, the density of space charge carriers induced by electronic trapping should remain the same as that at room temperature, especially after static high biases are applied for extended period of time and all the trap states get neutralized or ionized (depending on the location of the traps and the polarization of the bias) [101]. Such expectations based on electron trapping, however, contradict our experimental observations—the amplitude of the electric field associated with the persistent space charges is significantly reduced as the temperature drops from 295 K to 235 K (Figure 2-11c).

2.2.2 SPCM on "dry-method" processed $CH_3NH_3PbI_3$

2.2.2.1 Preparation of perovskite thin films at elevated temperature

The persistent space charges induced by external biases can be drastically suppressed in hybrid perovskites processed at elevated temperature. Using thermal evaporation followed by solid-vapor reactions, we created $CH_3NH_3PbI_3$ perovskite thin films at a reaction temperature up to 150 °C. In addition to solution synthesis, perovskite thin films were also created at elevated temperature using a two-step solid-vapor reaction method[102,103]. 40-nm thick PbI_2 was first deposited onto the glass substrate (pre-patterned with Au electrodes) using a thermal evaporator (Edward 306A). The PbI_2

thin film was then brought into reaction with CH_3NH_3I vapor in a quartz tube furnace. The CH_3NH_3I vapor was generated by placing the CH_3NH_3I powder at the center of the quartz tube (~150 °C). The substrate with the PbI_2 thin film was placed at the downstream close to the source. The reaction was carried out for 2 hours with 30 SCCM flow of high purity N_2 gas at a pressure of 500 Torr. The converted films were encapsulated using PMMA.

High-temperature treatment is often used as an effective approach to improve the crystallinity and reduce the density of defects, especially the metastable point defects that are more likely trapped in lattices during synthesis at a lower temperature. These defects may be too subtle to be detected using crystallography techniques, but their effects on optical and electronic properties can be significant. A good example is ZnO nanowires obtained using low-temperature hydrothermal synthesis or high-temperature physical vapor transport growth, which exhibit remarkable differences in electrical conductivity and photoluminescence efficiency[104-106].

2.2.2.2 SPCM on "dry-method" processed CH3NH3PbI3

While the gas-phase reacted hybrid perovskites (or dry perovskites) exhibit negligible differences in crystallinity compared with the solution-synthesized samples (Figure 2-13a), the grain size is notably larger in the perovskites obtained at the higher temperature (Figure 2-13a, inset). Features related to ion migration are significantly weakened in the photocurrent mapped in the dry perovskites. Under static biases, the maximum of the photocurrent profile remains confined near the anode (Figure 2-13b), similar to the photoresponse under low biases in the solution-processed perovskites (Figure 2-13a). This maximum is identified in earlier discussions as the feature of the reverse-biased Schottky junction. The peak moves slightly towards the center of the perovskite channel when the bias exceeds 3 V, showing that only a small number of ions can migrate under higher biases in the dry perovskites. The photocurrent peak near the cathode, observed in the solution-processed perovskites as the feature of mobile-ion induced p-n junction under high biases (> 3.5 V), never emerges in the dry perovskites even if the bias is increased to 10 V. It is also worth noting that these dry perovskites are much more stable under high biases applied likely due to the suppressed ion migration. When the solution-processed perovskites have already exhibited electrochemical breakdown under 6 V bias (Figure 2-10), dry perovskites are much more durable without obvious degradation under 10 V bias.

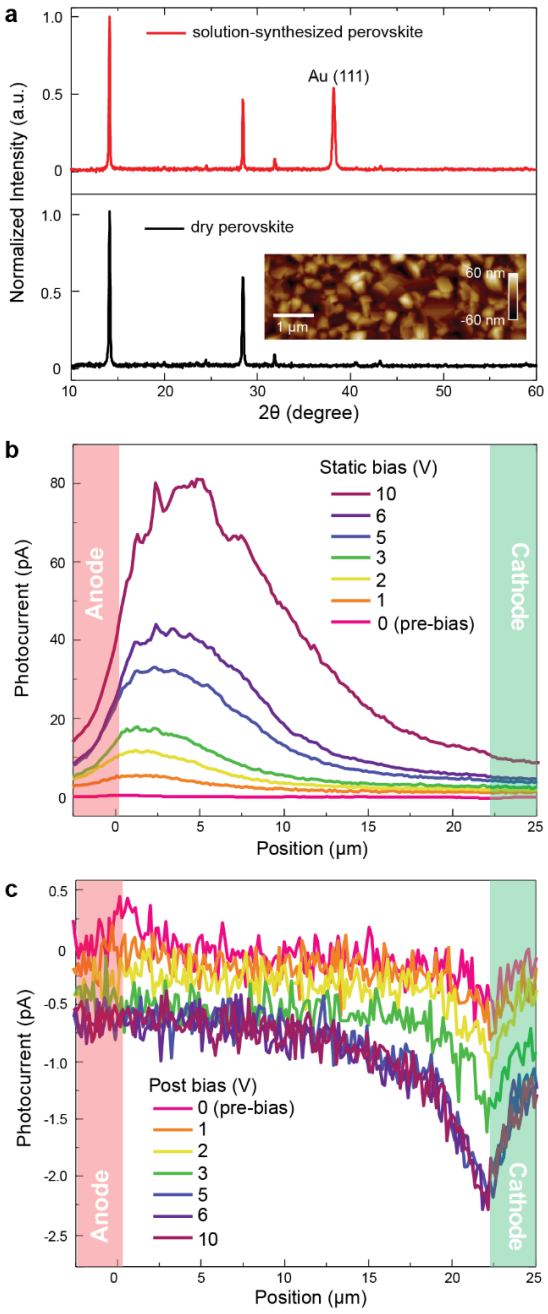

Figure 2-13 $CH_3NH_3PbI_3$ processed at elevated temperature exhibits suppressed space charge accumulation under applied biases. (a) The XRD patterns show negligible differences in the crystallinity between of the solution-processed perovskite (top) and the dry perovskite (bottom). The AFM image in the inset shows larger grain size. (b) The photocurrent with the static biases applied has a maximum confined near the anode which is caused by the reversely biased Schottky junction there. The small shift of the peak position may be caused by the mobile ion-induced space charges, similar to the situation under lower biases in the solution-processed perovskite. (c) Post-bias photocurrent shows much weaker persistent electric field in the dry perovskites compared with the solution-processed ones.

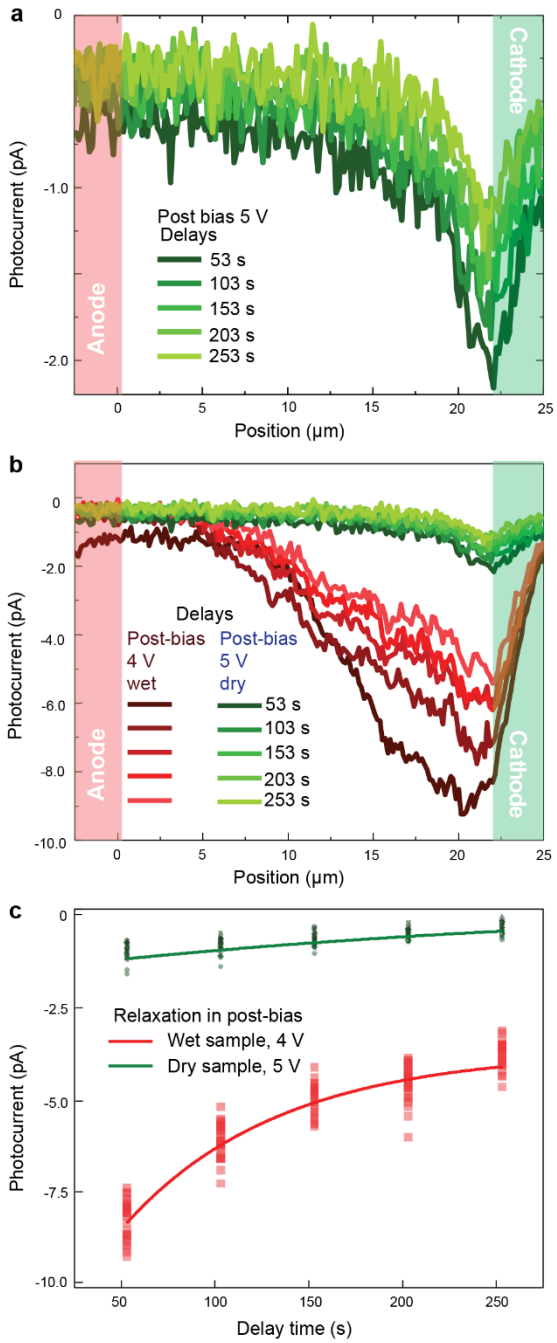

Figure 2-14 Relaxation of persistent photocurrent in the dry sample synthesized from an elevated temperature shows a slower rate. (a) The spatially resolved photocurrent after removing 5 V bias is a function of time. The scan is continuous, and each scan takes 50 seconds. (b) The comparison of relaxation between the elevated temperature synthesized dry sample and the low temperature solution synthesis solution sample shows the former one has much smaller change of persistent photoresponse. (c) The slower relaxation rate of dry samples suggests a reduced ion mobility. The solid lines are the single exponential fittings showing the relaxation rate fitted from the wet sample is 1/92 s^{-1} while the dry sample has a relaxation rate of 1/263 s^{-1}.

The suppressed ion migration is also reflected in post-bias photocurrent. After the bias is removed, the short-circuit photocurrent shows residual built-in potential as a sign of the mobile-ion induced space charges accumulated near the cathode (Figure 2-13c). The number of the persistent space charges, indicated by the magnitude of the short-circuit photocurrent, appears much less compared with that observed in the solution-processed perovskites (Figure 2-5). The weakened effects of ion migration can be attributed to the reduced ion mobility or lower defect density. Saturation in the residual built-in potential is observed when the bias exceeds 5 V. Assuming that the migration and accumulation of the $CH_3NH_3^+$ cations near the cathode is facilitated by the $CH_3NH_3^+$ vacancies[77], such saturation can be considered the evidence for lower defect density in the dry hybrid perovskites. In the meantime, the reduced ion mobility can be observed as slower relaxation of accumulated space charges after the removal of applied biases (Figure 2-14).

2.3 Conclusions and future remarks

In summary, using photocurrent and surface potential mapping techniques, we have visualized spatially the dynamic formation of built-in electric field in the halide perovskite $CH_3NH_3PbI_3$ under electric biases. Not only does our work provide a microscopic picture for the *I-V* hysteresis commonly observed in $CH_3NH_3PbI_3$, the formation of dynamic p-n junctions suggested by the SPCM and KPFM images can also help understand the unique optoelectronic functionalities such as switchable photovoltaic effects or junction-less LEDs based on halide perovskites. The relaxation kinetics of the bias-induced space charges, along with a temperature-dependent study, suggests ion migration being the driving force behind these dynamic phenomena. Importantly, we found that the dependence of charge transport properties on the history of the biases applied can be effectively suppressed if the hybrid perovskite $CH_3NH_3PbI_3$ is created at elevated temperature. We speculate that the thermal treatment can help reduce point defects (vacancies) which are believed to facilitate ion migration by providing effective and low-energy pathways. This finding can have a practical impact because halide perovskites that are less prone to performance degradation with operating history are highly desirable for developing stable and reliable perovskite-based optoelectronics.

The verification of the doping hypothesis by compensated charges of ions is going to be done by using spatially resolved Hall effect measurement. The schematic of the devices for Hall effect measurement is shown in Figure 2-15. As discussed in the model of Fig 2-9, by applying different

bias voltages, the doping level of the perovskite material close to anode/cathode will change, which will result in the variation of Hall voltages in different pairs of electric leads, i.e., the spatially separated pairs of hall voltage measurements leads shown as V_1~V_5 would have increased/decreased values.

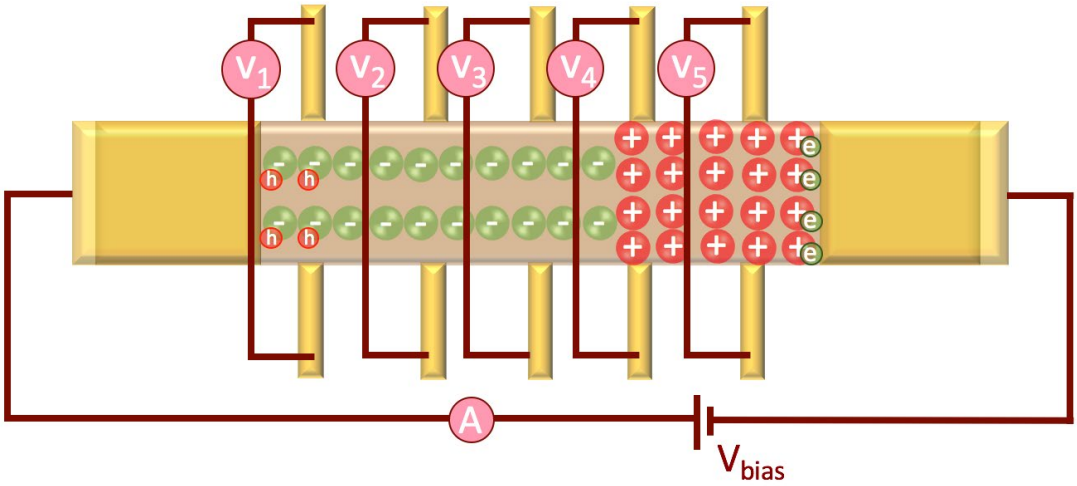

Figure 2-15 Schematic of spatially resolved Hall measurement.

CHAPTER 3
PHASE STABIITY IN MIXED-HALIDE PEROVSKITE COMPOSITES

3.1 Introduction of composites

In the long history of developing and utilizing man-made materials, composite materials have played indispensable roles. Two or more constituents are incorporated in specific ordering so that the product exhibits combined advantages from each component. Successful examples span from conventional composites for building construction (concrete, plywood, fiberglass) to advanced materials for microelectronics[107].

To researchers at the frontier of optoelectronics, the question now is whether the concept of compositing can be applied to a new class of photoactive materials — halide perovskites. Despite the success of device demonstration in laboratories, commercialization of the perovskite-based optoelectronic technology remains challenging. A particular concern is how the excellent physical properties can be retained when the photoactive materials are integrated into functional devices, especially when these devices need to be operated for an extended period of time. It has been reported repeatedly that the photoresponse, the charge transport, or even the desirable crystal phases of halide perovskites could vary significantly under continuous optical, electrical or thermal stimulation.[10,65,108,109] For instance, $CsPbI_3$ could lose its photoactive perovskite phase slowly at room temperature[65]; mixed-halide perovskites suffered from bandgap shifting under optical illumination[10,47]; LEDs made of perovskites could become considerably less emissive when operated continuously under electrical biases.[109] These slowly evolving processes undermined device reliability and longevity and, therefore, needed to be addressed for the development of viable applications.

Although it is not prevailing yet, initial work has shown that creating halide perovskites with composite structures could circumvent some of the above problems. In this chapter, I will be focusing on the perovskite composites $CsPbX_3/Cs_4PbX_6$ (X: halide ions, e.g. I^-, Br^-, Cl^-). The major part of the discussion will be the physics related to the stability of mixed-halide perovskites and how composite structures help suppress the phase separation.

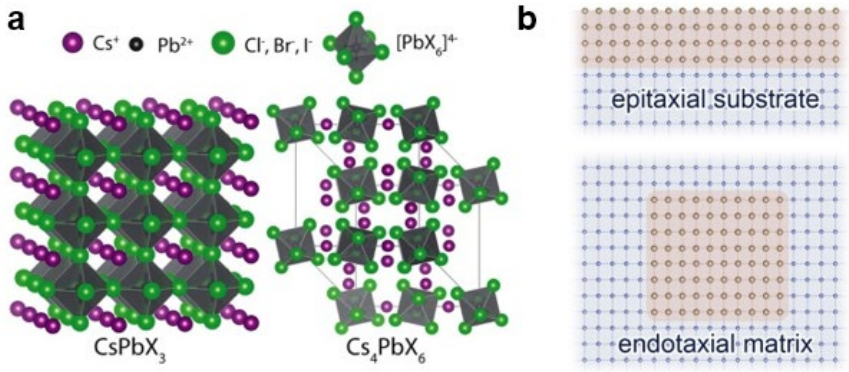

Figure 3-1 (a) Structural models of 3D cubic perovskite $CsPbX_3$ and 0D hexagonal Cs_4PbX_6 with X = Cl, Br, I. (b) Schematics of epitaxial versus endotaxial heterostructures. (A) Adapted with permission[110]. Copyright 2017 American Chemical Society.

3.1.1 Preparing composite perovskites

Perovskite $CsPbX_3$ is an efficient emitting material, whereas the host Cs_4PbBr_6 is an optically-inactive non-perovskite derivative of the ternary compound with the structures shown in Figure 3-1a[110]. Although not perfectly matched, the cubic lattice of $CsPbX_3$ and the hexagonal lattice of Cs_4PbX_6 can form the so-called endotaxial interfaces (Figure 3-1b) [111].

The thin films of mixed-halide perovskites and the $CsPbX_3/Cs_4PbX_6$ can be prepared by using dual-source thermal evaporation. Solid precursors $PbBr_2/PbI_2$ and CsBr/CsI were evaporated onto glass substrates followed by thermal annealing for sufficient inter-diffusion and reactions. With a stoichiometry ratio of Pb/Cs in the premixed precursors, polycrystalline thin films of $CsPb(Br_xI_{1-x})_3$ was obtained (Figure 3-2a). The host-guest structures could be achieved by simply increasing the relative weight ratio of the Cs-containing precursor (i.e. CsBr/CsI). According to the phase diagram[111], such variation of the precursor ratio would produce a mixture of $CsPb(Br_xI_{1-x})_3$ and $Cs_4Pb(Br_xI_{1-x})_6$ when fully reacted.

An Edwards E306A coating system was used for dual-source evaporation. Cs and Pb salts (CsBr, CsI, $PbBr_2$, PbI_2) were premixed with desirable ratios and used as precursor materials. Glass or thermal oxide substrates were cleaned sequentially by sonication in 1% Alconox precision cleaner solution, acetone, and isopropyl alcohol for 20 min followed by UV ozone treatment for 10 min prior to use. With a base pressure of 6×10^{-6} mbar, the two precursor mixtures containing Cs and Pb salts were evaporated alternatingly from separate quartz crucibles. The evaporation rates were controlled 0.1-0.5 Å s^{-1} for the Pb salts and 0.1-0.5Å s^{-1} for Cs salts. The above steps were repeated

until the desired composition and film thickness were obtained (Table 3.1). The evaporated samples were annealed at 150 °C on a hot plate in a nitrogen-filled glove box for 30 min. Cesium bromide (99.9%), cesium iodide (99.9%), lead bromide (98%) and lead iodide (98%) were acquired from Sigma-Aldrich.

Table 3.1 Parameters for thermal evaporation

		Cs Source	T (nm)	Pb source	T (nm)	T ratio Cs:Pb
113 rich	X_{Br} = 0.4	CsI	20	$PbBr_2/PbI_2$ 4/1	20	1
	X_{Br} = 0.5	CsI	20	$PbBr_2/PbI_2$ 6/1	20	1
	X_{Br} = 0.6	CsI/CsBr 1/1	20	$PbBr_2/PbI_2$ 6/1	20	1
	X_{Br} = 0.7	CsI/CsBr 3/1	20	$PbBr_2$	20	1
	X_{Br} = 0.8	CsI/CsBr 1/2	20	$PbBr_2$	20	1
	X_{Br} = 0.9	CsI/CsBr 1/3	20	$PbBr_2$	20	1
416 rich	X_{Br} = 0.4	CsI	7.5 x 4	$PbBr_2$	2.5 x 4	3
	X_{Br} = 0.5	CsI/CsBr 5/1	7.5 x 4	$PbBr_2$	2.5 x 4	3
	X_{Br} = 0.6	CsI/CsBr 3/1	7.5 x 4	$PbBr_2$	2.5 x 4	3
	X_{Br} = 0.7	CsI/CsBr 1/1	7.5 x 4	$PbBr_2$	2.5 x 4	3
	X_{Br} = 0.8	CsI/CsBr 1/2	7.5 x 4	$PbBr_2$	2.5 x 4	3
	X_{Br} = 0.9	CsI/CsBr 1/4	7.5 x 4	$PbBr_2$	2.5 x 4	3

The initial characterization to confirm the chemical phases include X-ray diffraction (XRD) and UV-VISIBLE absorption (UV-VIS). Optical absorption spectra were measured using an Agilent Cary 5000 UV-Vis-NIR spectrometer. To avoid the exposure to the moisture in air, the samples were placed in a home-made airtight container with two sapphire windows. The XRD patterns showed that the lattice constant of cubic-phase perovskites shifted as the ratio of Br/I was varied (Figure 3-2a). The corresponding spectral edge of the optical absorption (bandgap) changed monotonically to higher energy as the ratio of Br/I was increased. which was consistent with the gradually changed lattice constant in XRD (Figure 3-2c). The composite thin films were found to be dominated by the host matrix $Cs_4Pb(Br_xI_{1-x})_6$. Consistently, the optical absorption spectra were

also dominated by $Cs_4Pb(Br_xI_{1-x})_6$. The shift of the absorption peak was a result of the change in the ratio of Br/I (Figure 3-2b and Figure 3-2d).

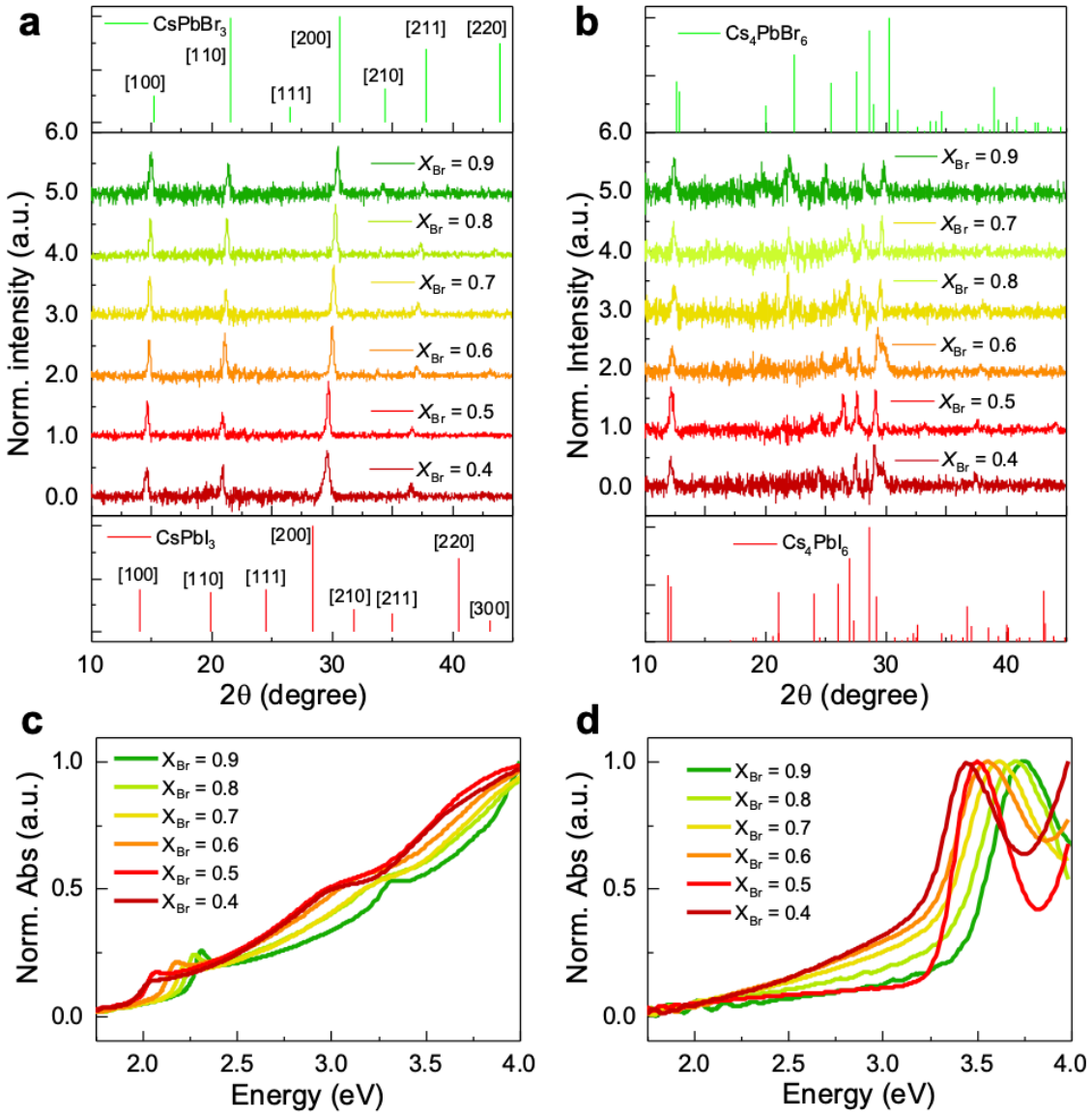

Figure 3-2. XRD and UV-VIS absorption spectroscopy were used to check the composition of the thin films. (a) The XRD patterns of pure perovskites. (c), the corresponding spectral edge of the optical absorption (bandgap) changed monotonically to higher energy as the ratio of Br/I was increased. (b) The composite thin films with dominated by the host matrix $Cs_4Pb(Br_xI_{1-x})_6$. (d) Optical absorption spectra were also dominated by $Cs_4Pb(Br_xI_{1-x})_6$.

3.2 Stabilized homogeneous phase of mixed-halide perovskites

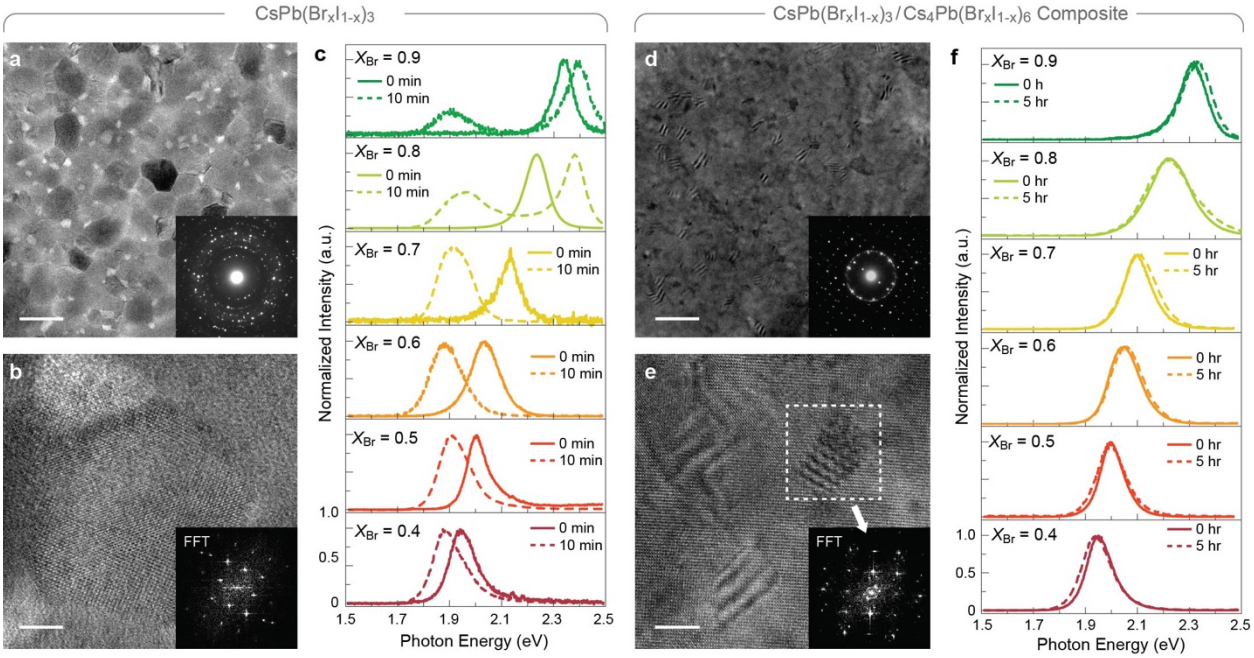

Figure 3-3. The phase stability of mixed-halide perovskite $CsPb(Br_xI_{1-x})_3$ is correlated with the morphology. (a) A representative TEM image of polycrystalline $CsPb(Br_xI_{1-x})_3$ thin films showed an average domain size around r = 35 nm. (b) An HR-TEM image of a single domain and the corresponding FFT pattern of the image (inset) confirmed these thin films were composed of perovskites. (c) The photoluminescence peak of these mixed-halide perovskites shifted exclusively to 1.87 eV after continuous illumination. The solid lines were the spectra taken from freshly made samples and the dashed lines were measured after 10-min illumination with the intensity of 0.3 W cm^{-2}. (d) In composite thin films, $CsPb(Br_xI_{1-x})_3$ and $Cs_4Pb(Br_xI_{1-x})_6$ formed host-guest structures. Inset: the electron diffraction pattern was dominated by a $Cs_4Pb(Br_xI_{1-x})_6$ single crystal, where the ring came from the distributed $CsPb(Br_xI_{1-x})_3$ crystallites. (e) An HR-TEM image with clear Moiré Fringes showed an average $CsPb(Br_xI_{1-x})_3$ domain size about r = 7.5 nm. Inset: the FFT pattern of the highlight area confirmed that the Moiré Fringes were formed by overlapping the lattices of the $Cs_4Pb(Br_xI_{1-x})_6$ host and the $CsPb(Br_xI_{1-x})_3$ guest. (f) The wavelength-tunable photoluminescence from the $CsPb(Br_xI_{1-x})_3$ crystallites in the composites exhibited high stability under 0.3 W cm^{-2} illumination. The scale bars in (a) and (d) are 100 nm and 50 nm respectively. The scale bars in (b) and (e) are 10 nm.

The phase separation issue is introduced in the first chapter (Session 1.1.3). while the freshly prepared mixed-halide perovskites exhibit homogenous crystal phases, the bandgap could vary significantly under continuous optical illumination. Various measurements indicate that the observed bandgap shifts could be attributed to photoinduced phase separation[10,47-52]. The homogeneously distributed halogen anions segregated into bromine- and iodine-rich domains, exhibiting a redshifted photoluminescence peak and split X-ray diffraction patterns[10]. A few

studies show that such photoinduced degradation could be mitigated in some of the mixed-halide perovskites with certain compositions[46,112]. Yet, stabilizing the bandgap across the entire spectrum (from pure bromide to pure iodide, i.e. $0 < x < 1$) remains challenging. In this work, we find that the light-induced phase separation could be effectively suppressed when crystals of the mixed-halide perovskite $CsPb(Br_xI_{1-x})_3$ are spatially confined in an endotaxial matrix $Cs_4Pb(Br_xI_{1-x})_6$. Stabilization of the tuned bandgap is achieved across the full spectrum (regardless of the Br/I ratio). It is remarkable that, for certain composition ($x \leqslant 0.6$), the tuned bandgaps remain stable under extremely intensive illumination up to 440 W cm^{-2} (as a reference, the standard solar spectrum (AM1.5) has an integrated power density of 0.1 W cm^{-2}). Note that such intensity is about an order of magnitude higher than what is typically used in concentrator solar cells[113].

3.2.1 Correlation between phase stability and morphology

A representative TEM image of Polycrystalline thin films of $CsPb(Br_xI_{1-x})_3$ showed an average domain size around r = 35 nm. The cubic crystal phase was also confirmed consistently in the selected area diffraction (SAD) patterns (Figure 3-3a, inset), the high-resolution transmission electron microscopy (TEM) images, and the corresponding fast Fourier transformed (FFT) patterns (Figure 3-3b), consistent with the XRD and UV-VIS results (Figure 3-2). The photoluminescence peak (corresponding to the energy of bandgap) of $CsPb(Br_xI_{1-x})_3$ could be tuned by varying the ratio of Br/I in the premixed precursors (Fig. 3-3c).

Photoluminescence of all these $CsPb(Br_xI_{1-x})_3$, however, appeared unstable under extended photoexcitation (Fig. 3-3c). The peak position, regardless of its initial wavelength, redshifted to ~ 1.87 eV within 10 min of illumination at an intensity of 0.3 W cm^{-2} (compared with an integrated power density of 0.1 W cm^{-2} of the AM1.5 standard solar spectrum). Such redshift, corresponding to a reduction in the bandgap, is consistent with previously reported observations[47]. The initially homogeneous $CsPb(Br_xI_{1-x})_3$ segregated into Br- and I-rich domains with increased and decreased bandgaps, respectively. The energy transfer between neighboring domains makes the small-bandgap species (i.e. the I-rich domains) dominate the photoluminescence after the phase separation[10,47,48]. The exceptions in our experiments are the samples with very large Br content (Figure 3-3c, X_{Br} = 0.8 and 0.9), which exhibited photoluminescence from both large- and small-bandgap species (2.4 eV and 1.87 eV, respectively). The number of the Br-rich domains, in this case, is likely too large to be quenched completely by the I-rich domains.

The photoinduced phase separation is found to be highly suppressed when the mixed-halide perovskites $CsPb(Br_xI_{1-x})_3$ are created in form of nanocrystals and are embedded in a non-perovskite matrix $Cs_4Pb(Br_xI_{1-x})_6$. The expected composite structure was confirmed using TEM (Figure 3-3d). The electron diffraction pattern was predominately from the hexagonal lattices of the $Cs_4Pb(Br_xI_{1-x})_6$ single crystal (close to [100]). A faint ring corresponding to the {200} cubic plane of $CsPb(Br_xI_{1-x})_3$ indicated that many tiny crystallites of the perovskite were distributed within the 400-nm electron beam spot (Figure 3-3d, inset). The high-resolution TEM image showed that the nanocrystal $CsPb(Br_xI_{1-x})_3$, with an average radius of ~7.5 nm, were embedded in the $Cs_4Pb(Br_xI_{1-x})_6$ matrix with clear Moiré Fringes (Figure 3-3e). The photoluminescence from these isolated, spatially-confined perovskites appeared remarkably stable. After continuous illumination for 5 hours (0.3 W cm^{-2}, 365-nm wavelength), the emission wavelength remained unchanged in all the samples regardless of the Br/I mixing ratio (Figure 3-3f). Such photo-stability was only reported previously in iodine dominated mixed-halide perovskites ($x<0.3$) in rare cases[47]. A thermodynamic model based on nucleation theory[114] was developed to understand the mechanisms of the high photo-stability observed (APPENDIX A). In this model, whether the mixed-halide perovskites would remain homogeneous or experience phase separation is determined by changes of the Gibbs free energy ΔG. The homogenous phase would be stable when ΔG is negative.

ΔG in the dark (ΔG_{dark}) is contributed together by the volumetric enthalpy (Δh_{mix}), the volumetric entropy (Δs_{mix}) and the cohesive energies $\Sigma c_i r^2 W_i$:

$$\Delta G_{dark}(X_{Br},T)=\frac{4}{3}\pi r^3[\Delta h_{mix}(X_{Br},T)-T\cdot\Delta s_{mix}(X_{Br},T)]-\sum_i c_i W_i r^2 \quad \text{.....(3.1)}$$

The terms are functions of the average grain size r, the temperature T, and the relative number of bromine in the mixed-halide phase X_{Br}. Based on the quantities calculated using Density Functional Theory (APPENDIX B, *Computational Methods*), ΔG_{dark} is found to be negative regardless of the mixed-halide composition (Figure 3-4a). A relatively large domain size r = 35 nm was assumed in the calculation, but the results would not change qualitatively even if a larger r was used. The theoretical predictions are consistent with the experimental results observed in this work and reported previously: the photoluminescence spectra (Figure 3-3c), the X-ray diffraction patterns, and the UV-VIS absorption spectra (Figure 3-2a and Figure 3-2c) all indicated that the mixed-halide perovskites remained homogeneous in the dark.

Optical illumination could turn the ΔG to be favorable for phase separation under certain conditions. The effects of photoexcitation in the model were accounted for by involving the photoinduced polarons[26,48,115,116]. Polarons could bring in excessive strain energy (Δg_s) due to the locally shortened and lengthened Pb-halogen bonds (APPENDIX A):

$$\Delta G_{light}(X_{Br},T) = \Delta G_{dark}(X_{Br},T) + \frac{4}{3}\pi r^3 \cdot \Delta g_s(X_{Br}) \quad \text{.....(3.2)}$$

When Δg_s becomes sufficiently large, the strain energy would be released by de-mixing the halogen anions and forming Br- and I-rich domains (i.e. phase separation).

ΔG_{light}, assuming weak illumination, is found positive when $X_{Br} > 0.3$ (Figure 3-4b). The negative ΔG_{light} in the I-rich region is indicative of relatively better stability and stemmed from the larger interfacial area with nucleated I-rich domain with a fixed crystal size. The calculated threshold X_0 between the stable and unstable compositions is in reasonable agreement with those observed in our measurements (Fig. 3-3a) and reported by others previously[47]: photoluminescence from pure $CsPb(Br_xI_{1-x})_3$ redshifted notably under continuous optical illumination when $X_{Br} > 0.3$. The coincidence testified the reasonableness of the physical quantities that we obtained using the nucleation model. It is worth noting that the photoinduced phase separation is reversible in experiments. The shifted photoluminescence would gradually return to its initial wavelength after the optical illumination was removed. The reversibility is also a natural prediction in our theory given that the model was built entirely on the thermodynamic basis.

The phase separation under optical illumination could alternatively be suppressed if the domain size of the mixed-halide perovskites is reduced (APPENDIX A). The stability could be attributed to the dominating role of the cohesive energy ($\Sigma c_i r^2 W_i$) when the surface-to-volume ratio was increased. While all other terms in the model are proportional to the volume of the domains ($\propto r^3$), the cohesive energy is a function of the area ($\propto r^2$) (Equation (3.1) & (3.2) and Equation A1 ~ A3 in APPENDIX A). Domains of the new phase (i.e. the iodine-rich perovskite domains) nucleated out of the mixed-halide perovskites would need to reach a certain critical size r^* in order for the volume-proportional terms to dominate and the phase separation to prevail ($-\Delta G_{light} < 0$). In other words, if the mixed-halide perovskites are confined with an average domain size smaller than r^*, nucleation and growth of iodine-rich perovskite domains would never be energy favorable. In that case, the infinitesimal domains of the new I-rich phase would experience dynamic equilibrium between nucleation and dissolution without prevailing phase separation. Experimentally, by

confining the nanocrystals of mixed-halide perovskites with r = 7.5 nm in the non-perovskite matrix, we were able to limit the size of iodine-rich nucleates. The phase separation then would not occur regardless of the Br content X_{Br} (Figure 3-4c). The predicted phase stability agrees well with our experiments, in which nanocrystals of the perovskite $CsPb(Br_xI_{1-x})_3$ were spatially confined in the $Cs_4Pb(Br_xI_{1-x})_6$ matrix with large surface-to-volume ratio (Figure 3-3d-f). What also helps to suppress the phase separation is the endotaxial lattice matching between the $CsPb(Br_xI_{1-x})_3$ guest and the $Cs_4Pb(Br_xI_{1-x})_6$ host matrix[111]. The phase separation becomes further unfavorable because a segregated perovskite domain would increase the energy at the host-guest interfaces and raise the total Gibbs free energy (APPENDIX A).

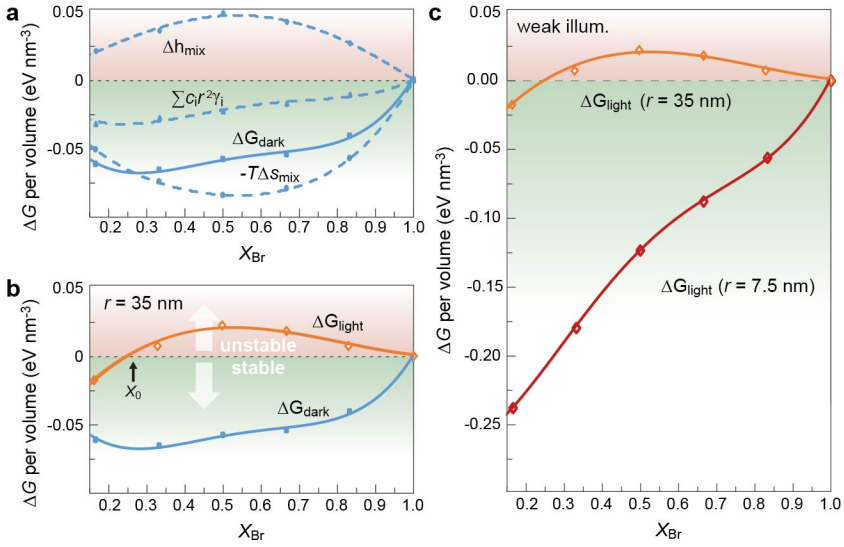

Figure 3-4 A thermodynamic nucleation model explains the dependence of phase stability on the morphology. a, The calculated ΔG_{dark} per volume (solid line) is negative regardless of the Br content. The dashed lines show the calculated volumetric enthalpy Δh_{mix}, volumetric entropy Δs_{mix}, and cohesive energy $\Sigma c_i r^2 W_i$. A relatively large grain size was used here (r = 35 nm). b, Under illumination, the calculated free energy ΔG_{light} becomes partially positive assuming the same grain size. A threshold composition $X_0 \sim 0.3$ divides the mixed-halide perovskites into stable (I-rich) and unstable (Br-rich) regions. c, To mimic the experimental conditions of the $CsPb(Br_xI_{1-x})_3/Cs_4Pb(Br_xI_{1-x})_6$ composites, a small grain size (r = 7.5 nm) was assumed and the cohesive energy was considered. The calculated ΔG_{light} turns negative, indicating a stable phase of homogenous mixed-halide perovskites

3.2.2 Spectral stability under extremely intensive illumination

Remarkably, the tuned bandgap of the $CsPb(Br_xI_{1-x})_3/Cs_4Pb(Br_xI_{1-x})_6$ composites remained stable even under extremely intensive illumination. Photoluminescence spectra were measured using a HORIBA iHR320 spectrometer, equipped with a HORIBA Synapse back-illuminated CCD. The samples were placed in a vacuum chamber with cryogenic temperature control (Janis ST-500). A continuous-wave diode laser (405-nm) was used as the photoexcitation source. By focusing the laser beam to a 3-μm spot, the optical power density (i.e. intensity) could reach as high as 442.0 W cm^{-2} (equivalent to 4400 times of integrated intensity of the AM1.5 solar irradiation). No obvious changes were observed in the photoluminescence spectra taken from the samples with $X_{Br} \leq 0.6$ (Figure 3-5a-c). However, with higher bromine concentrations, the samples started to show phase separation under the strong illumination condition (Figure 3-5d-f). The correlation between the photo-stability and the composition is consistent with the relative phase stability between the Br- and I-rich perovskites discussed above (Figure 3-4c). ΔG_{light} becomes smaller with less Br content (X_{Br}) and results in a more stable alloy phase. Note that the amount of peak shift appeared noticeably different between the composites and the pure perovskites: the peak in the former settled at higher energy (2.00 eV) compared with the latter (Figure 3-3c, 1.87 eV). The quantitative difference suggested a smaller degree of phase separation in the composites with a smaller change of iodine concentration in the segregated I-rich domains.

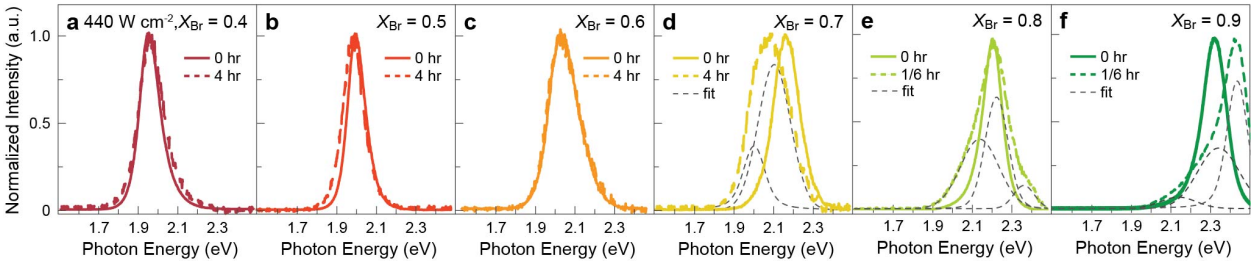

Figure 3-5 The perovskite composites remained stable under extremely intensive illumination. The solid lines are spectra obtained from experiments. The dash lines show the results of multiple-peak fitting. (a-c) Minimal changes were observed in the photoluminescence measured from the samples with $X_{Br} \leq 0.6$, even after 4-hour of illumination with intensity of 440 W cm^{-2}. (d-f) The sample with higher bromine content ($X_{Br} \geqslant 0.7$), which was stable under low-intensity illumination, exhibited redshift and blueshift in the photoluminescence with the strong illumination (440 W cm^{-2}).

The observed high photo-stability indicates that the cohesive energy is a more dominating factor in stabilizing a homogenous phase. As long as the grain size of the mixed-halide perovskites is sufficiently small, the presumable increase of the cohesive energy associated with the phase separation would dominate over the increase of the photoinduced strain energy, leading to a highly stable homogenous phase even though the high illumination intensity was assumed (APPENDIX A).

3.2.3 Temperature dependent photo-stability

Photo-stability of the mixed-halide perovskites, according to the theoretical model with an explicit variable T (Equation (3.1) & (3.2)), should also be a function of the temperature. In general, ΔG_{light} increases when the temperature is reduced (Figure 3-6a). Accordingly, an unstable mixed-halide perovskite could experience further phase separation as the temperature is lowered (Figure 3-6a, dashed line b). Alternatively, samples that are photo-stable at room temperature could become unstable (Figure 3-6a, dashed line c) or remain stable (Figure 3-6a, dashed line d) at a lower temperature depending on the level of Br content (X_{Br}).

We were able to observe such temperature dependence experimentally by measuring the photoluminescence at different temperatures. Samples with three representative compositions X_{Br} = 0.7, 0.5, 0.4 (corresponding to the vertical dashed line b/c/d in Figure 3-6a) were characterized. Given the high stability of the materials under low-intensity illumination, we had to use focused 405-nm laser light (440 W cm^{-2}) in order to reveal the evolution of photoluminescence with the temperature. For the most Br-rich perovskites (Figure 3-6b, X_{Br} = 0.7), the photoluminescence peak split at room temperature after continuous optical illumination. The spectral separation between the photoluminescence peaks was found to increase continuously as the temperature was reduced from room temperature to 200 K. The larger spectral split indicated higher iodine and bromine concentrations in the segregated domains, respectively. The reduced photo-stability could also be observed in the perovskite with nearly 1:1 Br/I ratio (Figure 3-6c, X_{Br} = 0.5). While no spectral shift was observed at room temperature, a new peak corresponding to I-rich domains emerged as the temperature was reduced. Among the three samples, only the one with the highest iodine content remained homogeneous regardless of the temperature (Figure 3-6d, X_{Br} = 0.4). The agreement between the theoretically predicted and the experimentally measured temperature dependence further validated the model of phase separation based on nucleation. Such phenomena could be attributed to the effect primarily driven by the changes of the entropy, which favor more

uniformly distributed bromine and iodine anions (i.e. a homogenous phase) at elevated temperatures, as often observed in alloy systems[114].

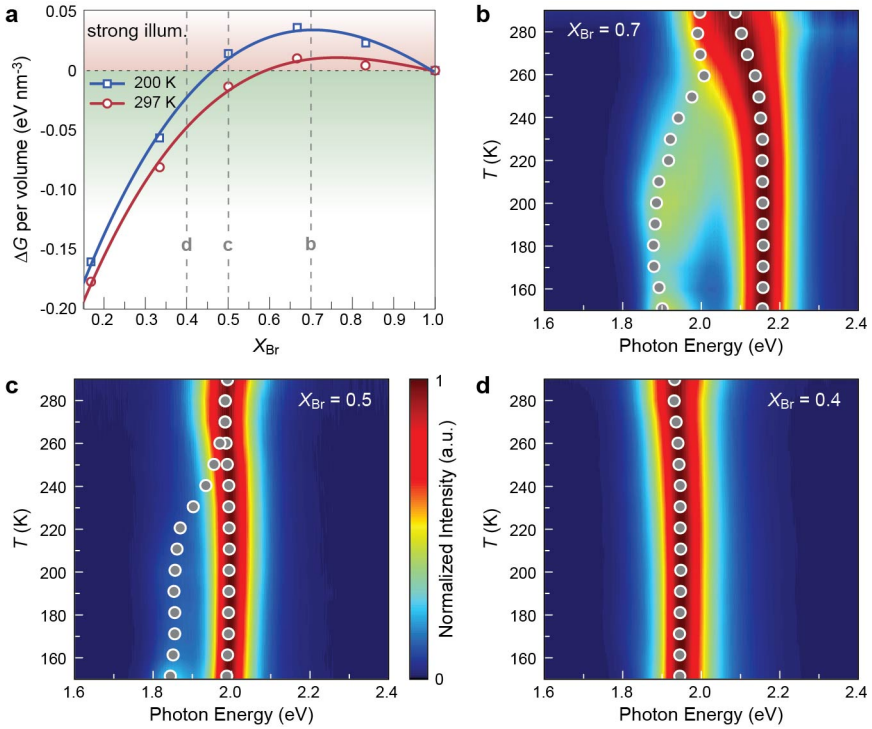

Figure 3-6 Photo-stability of the perovskites exhibited strong temperature dependence. (a) The calculated ΔG_{light} indicates that, under strong illumination, the perovskite in the composites would be less photo-stable as the temperature reduces from 297 K to 200 K. The vertical dash lines correspond to the compositions of samples examined experimentally in (b)-(d). (b-d) Photoluminescence spectra of $CsPb(Br_xI_{1-x})_3/Cs_4Pb(Br_xI_{1-x})_6$ composites with $X_{Br} = 0.7$ (b), $X_{Br} = 0.5$ (c) and $X_{Br} = 0.4$ (d) were measured at temperatures from 150 K to 290 K. Reduced photo-stability, indicated by further split of photoluminescence peaks, was observed at lower temperature in (b) and (c). The sample with higher iodine concentration in (d) ($X_{Br} = 0.4$) remained consistently stable across the entire temperature range, consistent with other measurements where I-rich perovskites appeared generally more photo-stable. The grey circles in (b)-(d) show the peak positions determined by fitting the measured photoluminescence spectra. (b)-(d) share the same color scale as shown in (c).

3.3 Discussions and future remarks

The stabilization of mixed-halide phases did not come at the cost of compromised optical properties. The photoluminescence quantum yields (PLQYs) of the composite thin films remained comparable with the previously reported bright emitters based on mixed-halide perovskites, with the highest reaching 36.8% (Figure 3-7a, $X_{Br} = 0.5$, 620-nm (2.0-eV) emission). The average photoluminescence lifetime was measured as 20 ~ 70 nanoseconds (ns), which appeared fairly long among the Cs-based perovskite thin films reported (Figure 3-7b). The addition of non-

conductive Cs_4PbX_6 may alter the electrical properties from that of the thin films containing pure mixed-halide perovskites. Future studies of electrical properties will be necessary to optimize the optoelectronic functionalities of the inorganic composite perovskites by, for instance, finely tuning the molar ratio between the two component compounds in the composites.

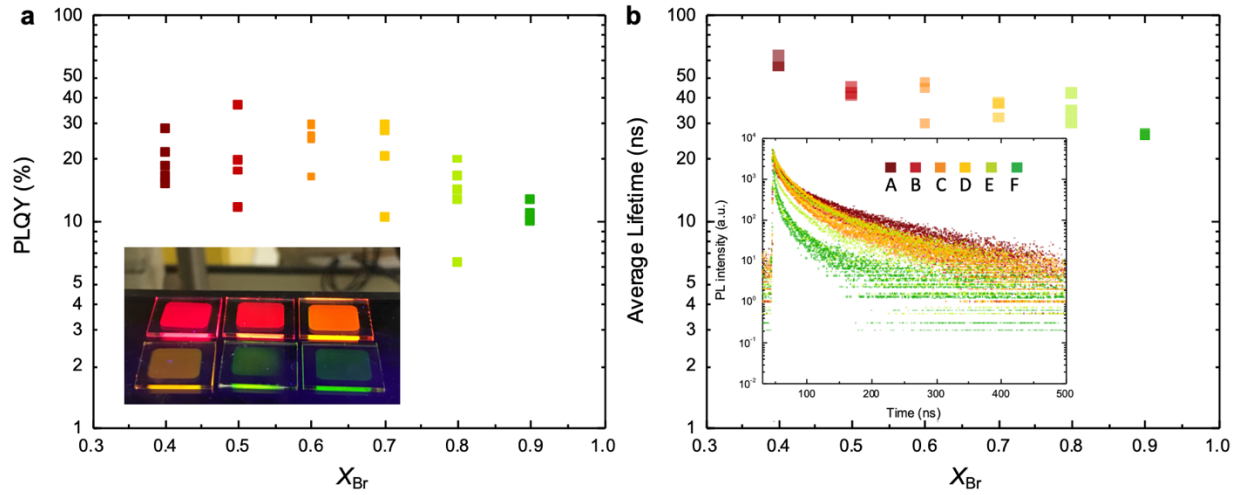

Figure 3-7 The stabilization of mixed-halide phases does not come at the cost of compromised optical properties. a. The general PLQYs of the all the mixed-halide perovskite thin films are at the level of > 10% with the highest number 36.8% (X_{Br} = 0.5, red color). Inset: bright photoluminescence of the $CsPbX_3/Cs_4PbX_6$ composite thin films was observed when excited with a hand-held UV lamp. The photo was taken with the room light on. b. The average lifetime is about 20 ~ 70 nanoseconds (ns).

CHAPTER 4
OPTOELECTRICAL PROPERTIES OF COMPOSITE PEROVSKITES

The composites $CsPbX_3$/ Cs_4PbX_6 showed high PLQY and long carrier lifetime, which is desirable for optoelectronic devices as introduced in Chapter 1. For device applications, both optical and electric properties need to be carefully characterized. To make the parameters simpler, the halide ratio X_{Br} will be eliminated as the parameter affecting the electric properties much is the ratio between $CsPbX_3$ and Cs_4PbX_6. I will focus on the $CsPbBr_3$ and $CsPbBr_3$/Cs_4PbBr_6 composites. In this chapter, the discussion about the enhanced optical properties in $CsPbBr_3$/Cs_4PbBr_6 will be drawn firstly, followed the discussion about electric properties and device performances with experimental results.

4.1 Improved optical properties and stability in $CsPbBr_3$/Cs_4PbBr_6 composites

4.1.1 Optical properties of $CsPbBr_3$/Cs_4PbBr_6 composites

Surface passivation can be particularly effective when the hosting matrices maintain certain levels of lattice coherence with the embedded nanocrystals—a favorable condition for reducing dangling bonds at the interfaces. The composite made of $CsPbBr_3$ and Cs_4PbBr_6 is one of these types. While the concentration of Cs_4PbBr_6, was increased, the brightness of photoluminescence of the $CsPbBr_3$/Cs_4PbBr_6 composite thin films keeps increasing (Figure 4-1a). But when the luminescent species $CsPbBr_3$ is totally eliminated, the Cs_4PbBr_6 has negligible PL under 365-nm Hg lamp (Sample F in Figure 4-1a).

The corresponding characterizations were shown in Figure 4-1b-d. The optical absorption peaks near 315 nm and 516 nm correspond to the bandgap energy of Cs_4PbBr_6 and $CsPbBr_3$, respectively (Figure 4-1b). Sample A-E have the corresponding ratio as shown in Table 4.1. The 33mol% is a ratio between B and C designed for the comparison of electrical properties and LED devices (details are in the later sessions). The changes of their relative intensity indicated the variations in the amount of $CsPbBr_3$ and Cs_4PbBr_6 contained in the thin films, which matched with the intended molar percentage (mol%) of Cs_4PbBr_6. X-ray diffraction patterns verified the coexistence of phase $CsPbBr_3$ and phase Cs_4PbBr_6 with varied molar concentration (Figure 4-1c). Higher concentration of Cs_4PbBr_6 was found in composite films prepared with larger ratio of $CsBr:PbBr_2$. The photoluminescence quantum yield (PLQY) increased monotonically when higher concentration of Cs_4PbBr_6 was incorporated (Figure 4-1d). All of the thin films exhibited green photoluminescence

with a peak near 516 nm (Figure 4-1d inset), corresponding to the band-edge excitonic emission from $CsPbBr_3$. For the composites containing a negligible amount of Cs_4PbBr_6 (i.e. nearly pure $CsPbBr_3$), the PLQY was as low as 1.22%, which is likely due to loss of spatial confinement[117] or non-radiative surface defects[31]. As the molar concentration of Cs_4PbBr_6 in the composite film was increased to ~95 mol%, the PLQY reached 40%.

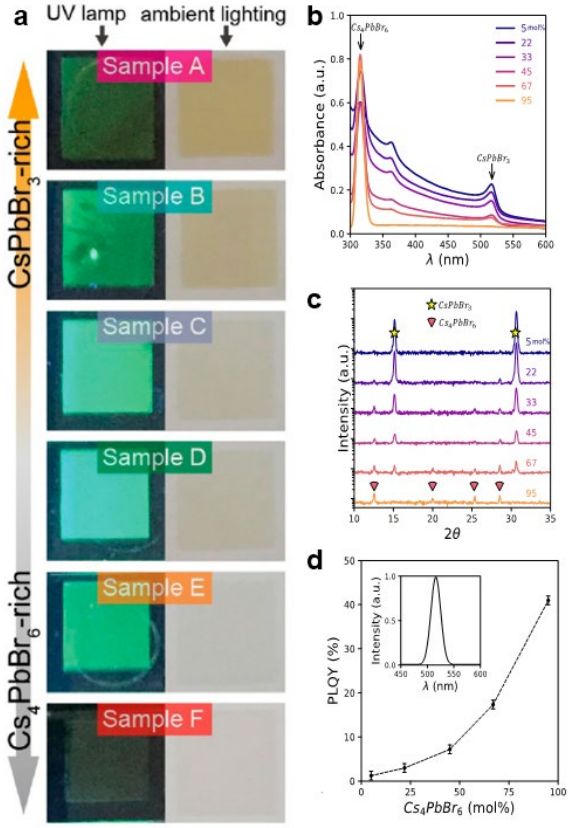

Figure 4-1 The presence of Cs4PbBr6 significantly affects the photoluminescent properties of the perovskite composites. (a) Thin films with various compositions under the 365 nm Hg lamp (left) and the ambient light (right). The corresponding mol ratio is shown in Table 4.1. Sample F is 100% Cs_4PbBr_6. (b) The absorbance spectrum and (c) X-ray diffraction (XRD) patterns of the perovskite composites with varied precursors ratios. The legends represent the mole percentage of Cs_4PbBr_6 in the composite perovskites, which were derived from the molar ratio of the precursors CsBr:$PbBr_2$ evaporated (c) Both absorbance spectrum and XRD patterns showed the gradual change of the composition ratio between Cs_4PbBr_6 and $CsPbBr_3$. (d) The PLQY of composite films increased with an increased percentage of Cs_4PbBr_6. (inset: Photoluminescence spectrum of composite films showing sharp peak near 516 nm with FWHM = 20 nm).

4.1.2 Mechanism responsible for improved optical properties: surface shallow trap formation

The enhanced PL from the CPB416-rich composites is accompanied by longer PL lifetime (Figure 4-2). Temperature-dependent PL (Figure 4-3) indicates that the enhanced PL in the perovskite composites may originate from passivated interfaces and increased exciton binding energy. As the temperature is lowered from 300 K, the integrated PL intensity first increases, followed by a decrease when the temperature is further lowered. The decrease of PL intensity with decreased temperature is more obvious when the interfacial area between $CsPbBr_3$ and Cs_4PbBr_6 is larger, i.e., higher Cs_4PbBr_6 concentration (Figure 4-3b).

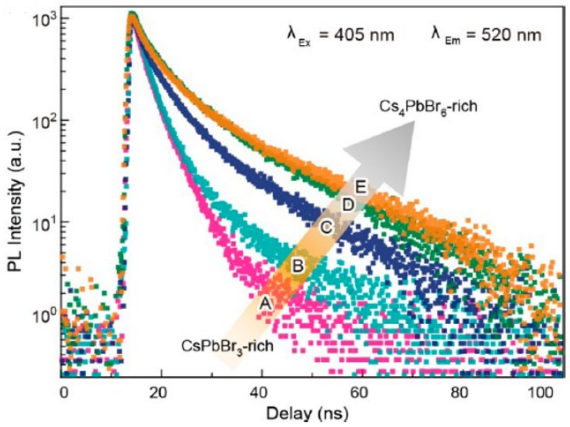

Figure 4-2 Enhanced PL lifetime with higher Cs_4PbBr_6 concentration.

Such a trend is rare. Usually, the PL intensity will increase when lower the temperature due to the suppressed phonon-assisted nonradiative recombination[118]. A mechanism that can lead to such so-called negative thermal quenching is the shallow trap states located near the edge of the bandgap[119]. The ionization energy of these states has to be so small that thermal perturbations (k_BT) at the room temperature are sufficient to excite the carriers trapped in these shallow states (Figure 4-4). These shallow states, therefore, are not effective traps at the room temperature. As the temperature reduces, k_BT decreases; the trapped carriers are less likely to be brought back thermally to the energy bands and, therefore, quench the PL. The temperature-dependent PL of the perovskite composites can be fit well using a combined exciton-trap model:

$$I(T) = I(0)\frac{1 + D_1 \exp\left(-\frac{E_q}{k_B T}\right)}{1 + C_1 \exp\left(-\frac{E_j}{k_B T}\right)} \quad \ldots\ldots(4.1)$$

E_j is the exciton binding energy, E_q is the ionization energy of the trap state, and $I(T)$ and $I(0)$ are the integrated PL intensities at finite temperature and hypothetically 0 K, respectively.

The fitting results are listed in Table 4.1. The depth of the shallow trap states E_q is comparable to $k_B T$ at room temperature. With higher Cs_4PbBr_6 concentration, the ratio of the shallow trap contribution increases. Also, as the big dielectric constant difference between $CsPbBr_3$ and

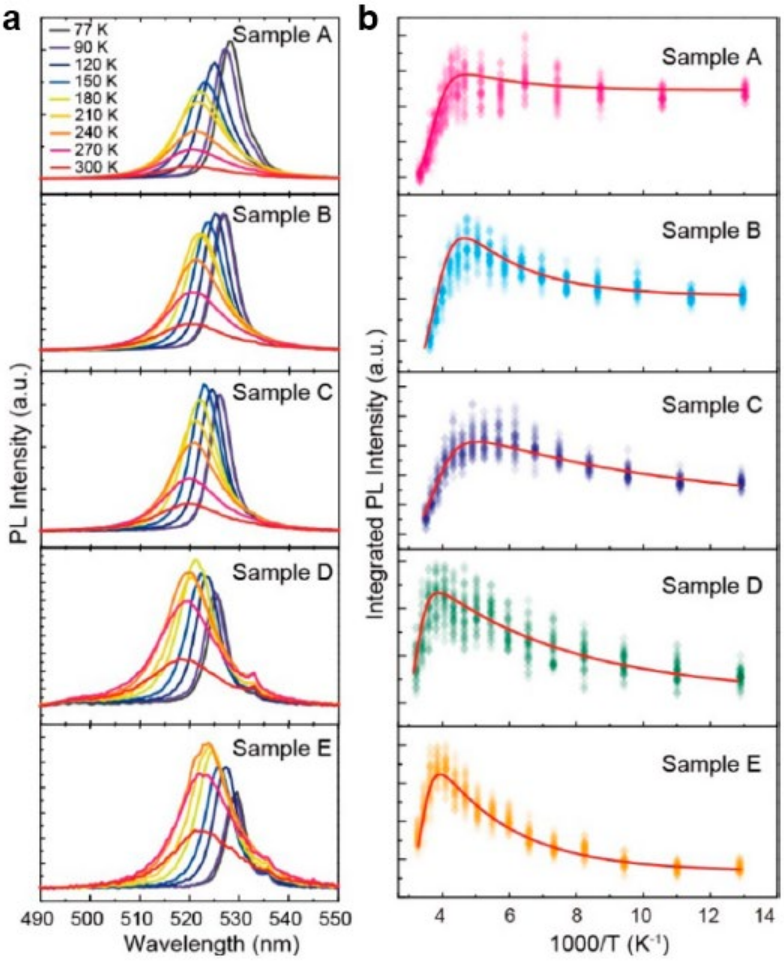

Figure 4-3 Temperature-dependent PL spectra indicate the mechanisms of the PL enhancement in the perovskite composites. (a) PL spectra collected from 77 K to room temperature (300 K). (b) Integrated PL intensity as the function of temperature. The solid curves are the fitting results based on the exciton-trap model. PL spectra were taken 50 times at each selected temperature for more reliable fitting. The fluctuations in the signal are primarily caused by the fluctuations from the q-switch laser source.

Cs_4PbBr_6, as well as the spatial confinement of $CsPbBr_3$ crystals by Cs_4PbBr_6 matrix, the exciton binding energy increases with the concentration of Cs_4PbBr_6.

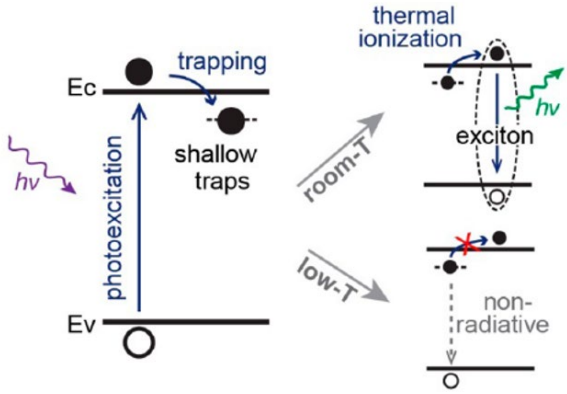

Figure 4-4 Schematics of the shallow traps which lead to the observed negative thermal quenching.

Table 4.1 Fitting results of temperature dependent PL based on the exciton-trap model

Sample	D_1	E_q (meV)	C_1	E_j (meV)	$I(0)$
A (5 mol%)	2.19	46.29	$2.10x10^6$	335.12	$5.52x10^5$
B (22 mol%)	5.76	42.38	$1.21x10^6$	276.29	$4.07x10^5$
C (45 mol%)	2.69	12.18	$1.02x10^6$	221.01	$1.31x10^5$
D (67 mol%)	6.13	20.31	$4.19x10^7$	445.96	$6.29x10^4$
E (95 mol%)	15.42	37.47	$2.99x10^7$	433.48	$4.32x10^4$

4.1.3 Improved stability in $CsPbBr_3/Cs_4PbBr_6$ composites

Besides enhanced physical properties, the composite structures also showed advantages in retaining the integrity of the materials in a longer timeframe. Stability is critical when materials are considered for viable applications. And this is particularly a problem for the halide perovskites, which is known to be unstable under various conditions[108].

Halide perovskites that have been explored so far are almost exclusively sensitive to moisture[120]. The most straightforward strategy to prevent the water-induced degradation is encapsulation. Host-guest composites, with intercalated micro-/nanostructures, can provide natural encapsulation to the embedded crystallites. Different from packaging the entire devices with sealant, the encapsulation offered by composite structures is infiltrated microscopically into the photoactive

layer (i.e. the halide perovskites) and, therefore, expected to be more durable. The remarkable stability of the $CsPbBr_3/Cs_4PbBr_6$ composites, for example, has been observed in the air with the

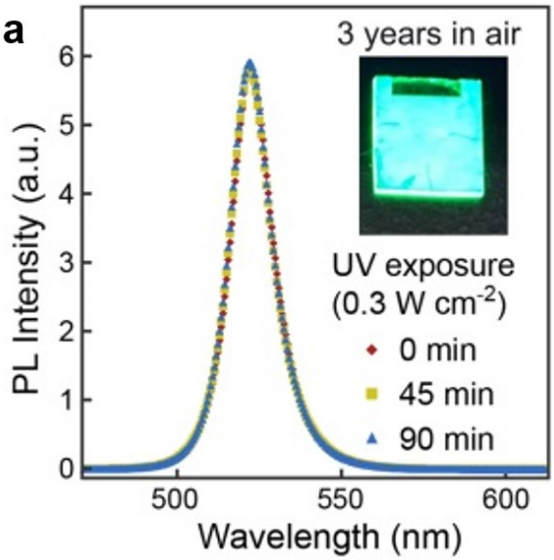

Figure 4-5 Photoluminescence spectra show that $CsPbBr_3/Cs_4PbBr_6$ composites remained stable against the ambient humidity even after stored in air for three years.

average relative humidity >55%. With the protection from the air-stable Cs_4PbBr_6 matrix, the embedded $CsPbBr_3$ crystallites remained structurally and optically stable in ambient environment for years (Figure 4-5).

4.2 $CsPbBr_3/Cs_4PbBr_6$ systems for devices

4.2.1 Electric properties related to device application

Besides optical properties, electrical properties of the composite thin films also exhibited strong dependence on the composition. As the concentration of Cs_4PbBr_6 was increased, the films became more electrically resistive.

AFM topography images showed that the films were composed of two types of crystalline grains with distinct morphology (Figure 4-6a). The increased concentration of Cs_4PbBr_6 coincided with the increase of the overall area of the larger domains, while the area of smaller grains (<100 nm) was reduced. The correlation between XRD, absorption spectrum and AFM images suggested that the smaller grains were dominated by $CsPbBr_3$ crystallites whereas the larger ones were primarily Cs_4PbBr_6. The matched patterns between the AFM topography and conductivity images showed clearly that the $CsPbBr_3$-dominated region (with smaller crystal domains) was more conductive (Figure 4-6a, b).

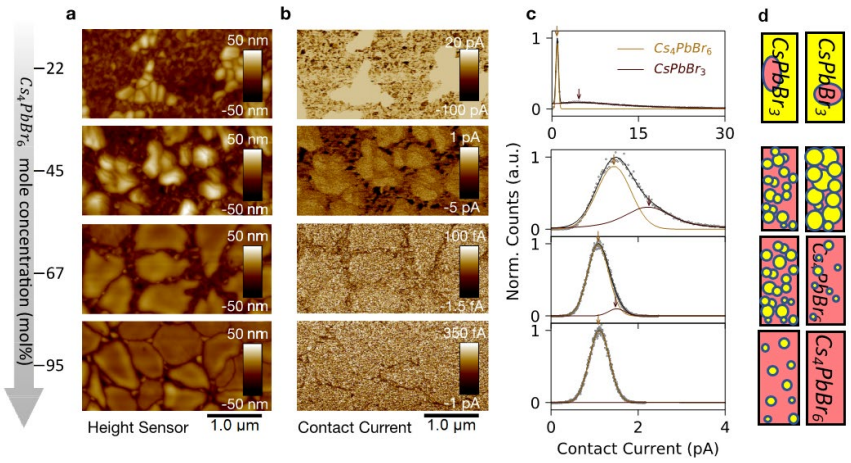

Figure 4-6 The conductivity distribution of the perovskite composite films implied electrical transport behaviors in the LED emitting layer. (a) Morphology and (b) contact current of composite films with different $CsPbBr_3$/Cs_4PbBr_6 ratio were measured using Peak Force Tunneling AFM (PF-tuna). The concentration of Cs_4PbBr_6 increased gradually from top to bottom with molar concentrations shown on the left bar. (c) The histogram of Figure 2b clearly shows the change of conductivity difference between $CsPbBr_3$ and Cs_4PbBr_6-rich area. The two fitted peaks corresponded to the conductivity of $CsPbBr_3$-rich area and Cs_4PbBr_6-rich area. The changes of relative areas under the 2 peaks matched well with the composition changes. The significant conductivity difference between $CsPbBr_3$ and Cs_4PbBr_6-rich area was suppressed as the concentration of Cs_4PbBr_6 increased. (d) Corresponding schematics indicate the relative distribution of $CsPbBr_3$ and Cs_4PbBr_6 based on the histogram.

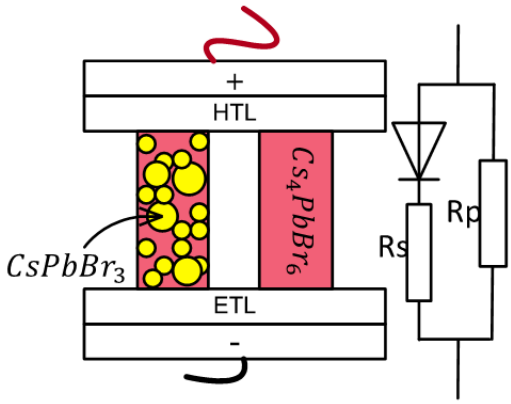

Figure 4-7 Schematic showing two types of current conducting channels (CsPbBr3-rich zone and Cs_4PbBr_6-rich zone) through the perovskite layer.

Histograms of conductive-AFM images showed quantitatively how the electrical properties evolved locally in $CsPbBr_3$- and Cs_4PbBr_6-rich domains as the film composition varied (Figure 4-

6c). Two distinct peaks (by Gaussian fitting) were observed in each histogram, with the high-current peak corresponding to the more conductive $CsPbBr_3$ domains and the lower-current peak representing Cs_4PbBr_6-dominated region. The two distinct peaks corresponding to the two conducting channels in Figure 4-7, as R_s and R_p respectively. As the concentration of Cs_4PbBr_6 was increased, both the under-the-curve area and the magnitude of the current of the high-current peak decreased. The former is consistent with the obvious reduction of the total area of $CsPbBr_3$ domains in the AFM images; the latter suggested that more Cs_4PbBr_6 filled between the $CsPbBr_3$ crystallites and made these regions less conductive. On the contrary, the conductivity of Cs_4PbBr_6-dominated domains remained nearly the same in all of the samples tested.

4.2.2 LED devices

To further explore the charge transport behavior and demonstrate optoelectronic functionalities, LED devices were constructed using composite perovskites as the emitting layer. The electrical behaviors of the LEDs exhibited strong dependence on the concentration of Cs_4PbBr_6. All of the devices exhibited green electroluminescence uniformly across the ~2 cm^2 device area (Figure 4-8a, inset). Compared with photoluminescence, the excellent color purity was retained in the electroluminescence with narrow FWHM ~23 nm (Figure 4-8a). Devices with a minimal amount of Cs_4PbBr_6 (5 mol%) exhibited moderate luminance ~5,000 cd m^{-2} even if a high bias of 12 V was applied (Figure 4-8b). The brightness of electroluminescence kept increasing as the concentration of Cs_4PbBr_6 was increased, until the maximum luminance (~55,000 cd m^{-2}) was reached with 45 mol% Cs_4PbBr_6. In devices with further increased concentration of Cs_4PbBr_6, the luminance began to decrease on the contrary. A similar trajectory was observed in EQE of the LED devices (the ratio of the number of photons emitted to the number of electrons passing through the device) as a function of the thin film composition (Figure 4-8c). The EQE began with 0.13% in $CsPbBr_3$-dominated devices (comparable to the reported devices based on pristine $CsPbBr_3$) [45], reached the maximum of ~2.5% with an intermediate concentration of Cs_4PbBr_6 (45 mol%), and dropped to ~0.22% when the emitting layer was dominated by Cs_4PbBr_6 (95 mol%).

The composition-dependent physical properties of the composite perovskites led to strong dependence of LED device performance on the ratio of $CsPbBr_3/Cs_4PbBr_6$ incorporated. The composition-dependent device performance can be understood as collective effects of the optical properties represented by PLQY and the electrical properties represented conductivity. By superposing the PLQY, the conductivity and the EQE together (Figure 4-8d), one can clearly see

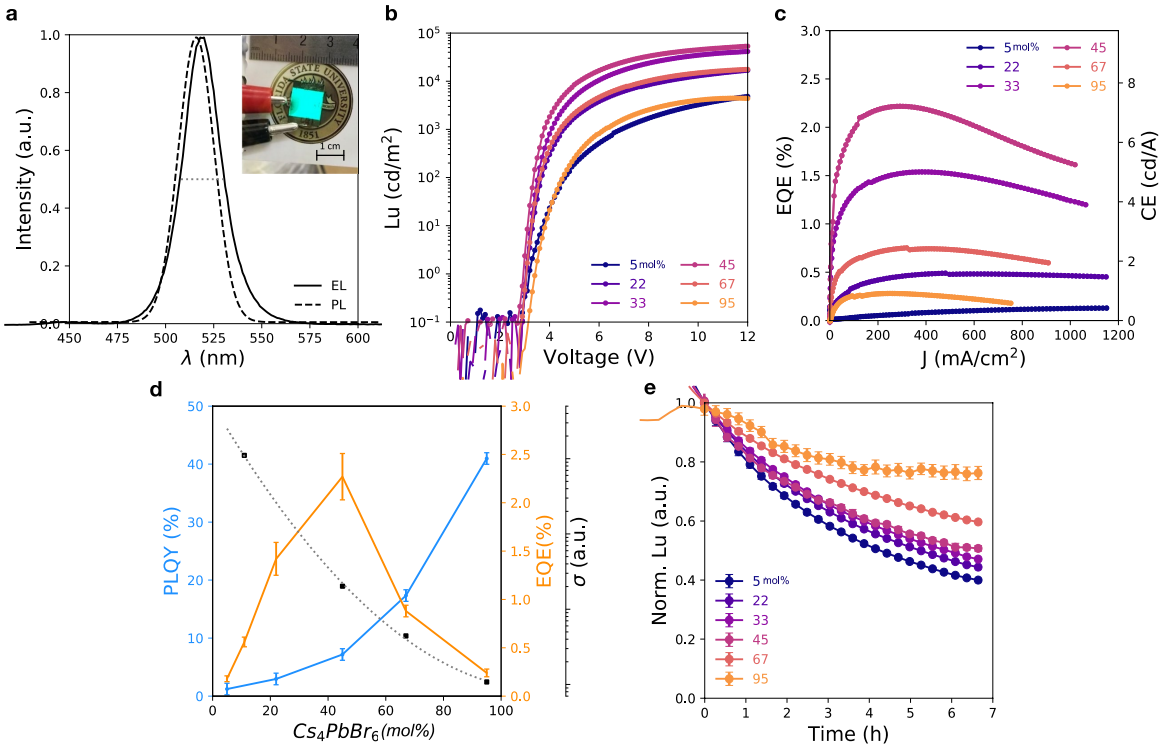

Figure 4-8 Composite perovskite-based LED performance could be optimized through tuning the concentration of Cs_4PbBr_6. (a) Photoluminescence and Electroluminescence spectrum of $CsPbBr_3/Cs_4PbBr_6$ composite film-based LEDs. The inset is a photo of our LED device with ~2 cm^2 pixel size, which suggested the ability to fabricate large-scale LED devices. (b) Luminance and (c) EQE for devices with respect to Cs_4PbBr_6 mole percentage. (d) PLQY, conductivity of the composite films and EQE of corresponding devices. Normalized luminance of LED devices under continuous operation for varied $CsPbBr_3/Cs_4PbBr_6$ ratios.

the two main factors affecting the device performance as functions of the Cs_4PbBr_6 concentration. In the region with moderate concentration of Cs_4PbBr_6, the efficiency of the LED devices followed the trajectory of PLQY and increased as a result of enhanced radiative recombination with a larger amount of Cs_4PbBr_6. Alternatively, in the region with high concentration of Cs_4PbBr_6, charge injection into the emitting centers (i.e. the $CsPbBr_3$ crystallites) became limited due to the low conductivity of Cs_4PbBr_6. Both the EQE and the electroluminescence brightness in this region exhibited a negative relation with respect to the concentration of Cs_4PbBr_6, suggesting that more electric current flowed through the optically inactive Cs_4PbBr_6 domains. This phenomenon agreed with the expectation based on the equivalent circuit discussed earlier (Figure 4-7). The increased concentration of Cs_4PbBr_6 would lead to increase in R_s and decrease in R_p, reducing the effective charge injection into the diode. The enhancement effect of Cs_4PbBr_6 can be further elaborated by

comparing the two extreme cases—the devices containing 5 mol% and 95 mol% Cs_4PbBr_6. Despite the unfavorable factors that Cs_4PbBr_6 was optically inactive and electrically insulating, the Cs_4PbBr_6-dominated devices were still more efficient (in EQE) than the $CsPbBr_3$-dominated devices, with comparable emission brightness. It's worth noting that the LED performance depended on the film morphology while the concentration of Cs_4PbBr_6 was a knob we found useful in tuning the morphology. The quantity of Cs_4PbBr_6 concentration, 45mol%, in this work corresponds to the optimized morphology for the devices (both optical and electrical properties). It is possible that using a different thin film preparation technique, the morphology would vary from what we obtained even if the molar concentration of Cs_4PbBr_6 remained the same.

Besides the enhanced performance, the composite thin films containing Cs_4PbBr_6 was found to be essential to the device stability. Primed LED devices based on different $CsPbBr_3/Cs_4PbBr_6$ composites were tested continuously under constant electric current. Significant improvement of the stability can be observed in devices containing higher concentration of Cs_4PbBr_6 (Figure 4e). While the luminance of $CsPbBr_3$-dominated devices dropped nearly 60% within 7 hours, only a <25% reduction was observed from $CsPbBr_3$-dominated devices under the same condition. Among the devices tested, the retention of luminance over extended operation increased monotonically with increased concentration of Cs_4PbBr_6. The improved stability can be attributed to two possible explanations: (a) the host-guest microstructure in the composites could suppress the global ion migration across the $CsPbBr_3$ domains, which could introduce the poling effect by electrochemical doping; (b) the isolation from the larger Cs_4PbBr_6 domains can inhibit growth of the embedded $CsPbBr_3$ crystallites in size, which was known to occur easily at slightly elevated temperature and diminish the enhancement effect of radiative recombination in spatially confined perovskites. What might also contribute to the observed stability was the all-inorganic composition of the composites. Note that the stability tests were carried out using devices without any thermal management mechanisms. Local temperature elevation in the emitting layer was expected to be significant due to the Joule heating. Electroluminescence remained uniform across the entire device area without noticeable failure (dark spots), suggesting minimal materials degradation in the emitting layer regardless of the elevated temperature during continuous operation.

4.3 Conclusion and remarks

In this 2-channel model, the more electrically resistive and optically inactive component (Cs_4PbBr_6) gave rise to shunt resistance R_p, whereas the resistivity of the photoactive component

($CsPbBr_3$) induced series resistance R_s. The inhomogeneous distribution of electrical conductivity could be beneficial when integrating such composite thin films into LED devices. Under electrical biases, the charge carriers may get preferably injected into the more conductive $CsPbBr_3$-dominated domains, which is the light emitting component in the composite material. This effect can mitigate the unfavorable charge transport properties of Cs_4PbBr_6 especially when a significant amount of Cs_4PbBr_6 is contained in the composite.

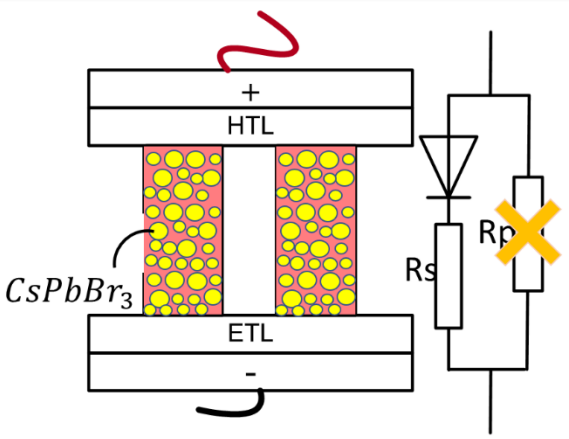

Figure 4-9 Schematic shows an improved configuration of host-guest structure. The separation of embedded nanocrystals is small which might utilize more efficient hopping and tunneling. Optically and electrically active area is maximized with inactive shunt resistant eliminated.

However, A high-performance optoelectronic device, regardless of light-to-electricity conversion or vice versa, requires the photoactive component to be both optically and electrically active. Numerous reports have testified the promises of composite perovskites with enhanced optical properties. When the device is optimized with the tuning of Cs_4PbBr_6 concentration, the area dominated by Cs_4PbBr_6 lowered the effective area of the emitting layer, resulting in lowered luminating efficiency of devices. Further improvement might be made if the shunt resistance area could be replaced by series resistance by the improvement of composite layer synthesis. Alternatively, if the separation between the embedded nanocrystals can be kept small, efficient charge transport could also be facilitated by tunneling or hopping.

The matrix material is not limited to insulating Cs_4PbBr_6. New matrices with considerably conductive might be more preferred if good interfaces can be formed between the matrices and halide perovskites.

CHAPTER 5
CONCLUSION AND OUTLOOK

In conclusion, we have studied physical properties of the halide perovskites from multiple aspects, including the charge transport, photoresponse and crystal phases (primarily on miscibility in mixed-halide perovskites). Many of these properties exhibit evolving behaviors under certain physical conditions, which can be understood as following: 1. Energy barriers for ions to migrate in the soft lattices of halide perovskites are low; 2. Defect states assist the ion migration with even lowered energy barriers, which makes the grain boundaries to be "express ways" for the ions; 3. In mixed-halide perovskites, the thermodynamic free energy of the system under operation conditions, such as under illumination, prefers the system to have phase separation, losing the designed properties; 4. The deformation of halide perovskites requires low energy especially with the mediation of moisture.

Because physical properties that vary with time are typically undesirable for practical applications, strategies to suppress such behavior and improve the material stability have been explored in the dissertation. Using thermal treatment to help reduce point defects (vacancies) to eliminate some effective and low-energy pathways for mobile ions (Chapter 2). This finding can have a practical impact because halide perovskites that are less prone to performance degradation with operating history are highly desirable for developing stable and reliable perovskite-based optoelectronics. Another effective method is to passivate the grain boundaries by creating suitable host-guest interfaces. With a beneficial interface, the undesirable trap states were observed to be effectively passivated with suppressed nonradiative recombination (Chapter 4). Surface passivation can be particularly effective when the hosting matrices maintain certain levels of lattice coherence with the embedded nanocrystals—a favorable condition for reducing dangling bonds at the interfaces. Although not perfectly matched, the cubic lattice of $CsPbBr_3$ and the hexagonal lattice of Cs_4PbBr_6 can form the so-called endotaxial interfaces. PL enhancement—the PLQY was enhanced at the room temperature with longer lifetime is an evidence support the passivation of deep defect states with the endotaxial $CsPbX_3/Cs_4PbX_6$ interfaces. Improved stability was also observed when composite perovskites were integrated in functional devices. Isolating $CsPbBr_3$ crystallites with larger Cs_4PbBr_6 domains seemed to inhibit the ion migration across the composites effectively. The suppression of ion migration might take effect in two ways: (i) grain boundaries often act as

the channel for rapid ion migration, which can be minimized when surface states or dangling bonds are passivated; (ii) the isolation of small perovskite crystals from non-ionic conductive matrix can inhabit massive migration of ions, avoiding the modification of internal electric field and material degradation due to global ion migration. LEDs based on pure $CsPbBr_3$ versus $CsPbBr_3/Cs_4PbBr_6$ composites were compared under constant-current conditions. Among the devices tested, the retention of luminance over extended operation increased monotonically with increased concentration of Cs_4PbBr_6. The results indicated that the all-inorganic composites may offer a solution to the long-term stability in perovskite-based LEDs.

Such endotaxial interfaces also led to the suppression of phase separation in mixed halide perovskites $CsPb(Br_xI_{1-x})_3$ (Chapter 3) when embedded in $Cs_4Pb(Br_xI_{1-x})_6$ matrices in form of nanocrystals. The photo-stability was found highly dependent upon the size of the nanocrystals. When the average radius (r) of the nanocrystals was sufficiently small, the increase of the interfacial energy ($\propto r^2$) would exceed the decrease of the Gibbs free energy in the bulk of the nanocrystals ($\propto r^3$), and phase separation became unfavorable in energy. Using this method, stabilized bandgap of $CsPb(Br_xI_{1-x})_3$ was achieved across the green-red spectrum, regardless of the Br/I ratio. For certain compositions ($x \leq 0.6$), the mixed-halide perovskites could sustain extremely intensive illumination for hours (up to 4400 times of the solar radiation) without noticeable phase separation. It is expected that such thermodynamically stabilized mixed-halide phases can also be applied to other compositions such as bromide-chloride solid solutions (e.g. $CsPb(Br_xCl_{1-x})_3$) and expand the tunable space across the entire visible spectrum. The tuned and stabilized bandgap can be essential to the development of tandem or concentrated solar cells, full-color LED displays, or wavelength-specific photodetectors.

Regarding the instability of decomposition with moisture, the host-guest composites, with intercalated micro-/nanostructures, can provide natural encapsulation to the embedded crystallites. Different from packaging the entire devices with sealant, the encapsulation offered by composite structures is infiltrated microscopically into the photoactive layer (i.e. the halide perovskites) and, therefore, expected to be more durable. Remarkable stability of the $CsPbBr_3/Cs_4PbBr_6$ composites, for example, has been observed in air with the average relative humidity >55%. With the protection from the air-stable Cs_4PbBr_6 matrix, the embedded $CsPbBr_3$ crystallites remained structurally and optically stable in ambient environment for years.

In spite of improved stability of the materials and devices we have achieved in halide perovskites using composite perovskites, the research on composite perovskites is far from being completed. A major uncertainty lies in their electrical properties. A high-performance optoelectronic device, regardless of light-to-electricity conversion or vice versa, requires the photoactive component to be both optically and electrically active. Numerous reports have testified the promises of composite perovskites with enhanced optical properties. However, not much has been done on their electrical properties. In fact, it would not be surprising if composite and pure perovskites exhibit behave electrically differently. In composites, the intercalated microstructures determine that charge transport through the host matrix will be inevitable when charge carriers are injected into or extracted from the photoactive sites (i.e. the embedded perovskite crystallites). Therefore, the matrix materials will have to be considerably conductive. Alternatively, if the separation between the embedded nanocrystals can be kept small, efficient charge transport could also be facilitated by tunneling or hopping. The specific structural configuration and the weight ratio between the compositing constituents will then be the key issues. Moreover, the type of the electronic band alignment at the host-guest interfaces will also need to be compatible with the functionality of the device. For instance, a type I heterojunction may be favorable for LEDs where exciton/carrier confinement in the perovskite nanocrystals can facilitate more efficient light emission; the same type of junction, however, would inhibit separation and extraction of excited charge carriers and, therefore, undesirable for solar cells.

Host-guest structures have led to tremendous success in the field of organic and hybrid optoelectronics (DSSC, OPV & OLED). It is hopeful that it will only take a good choice of the hosting material and a suitable interfacial configuration to achieve useful composite perovskites. The future of composite perovskites will rely substantially on the investigations of fundamental photophysics and charge transport in a large collection of compositing combinations.

APPENDIX A
THERMODYNAMIC MODEL ABOUT PHASE STABILITY

A thermodynamic model based on nucleation in phase transformation was developed to understand the mechanisms of the high photo-stability observed. In the model, photoexcited polarons, which were reported previously[48,121], tend to trigger the phase separation. The cohesive energy at interfaces, an additional factor that we considered in our model given the unique composite material morphology, is not in favor of separating mixed-halide perovskites into iodine-rich and bromine-rich domains. Particularly, when the interface-to-volume ratio is sufficiently large (i.e. the size of embedded perovskite nanocrystals was sufficiently small), the weight of the cohesive energy can dominate the total energy of the system, which eventually eliminates the photo-induced phase separation.

A.1 ΔG_{dark} for System in the Dark (Ground State)

Based on nucleation theory[114], the change of the free energy ΔG would be contributed together by the volumetric enthalpy (Δh_{mix}), the volumetric entropy (Δs_{mix}) and all the cohesive energies $\Sigma c_i r^2 W_i$. In the dark, $\Delta G = \Delta G_{dark}$ with the initial Br content X_{Br} was expressed as:

$$\begin{aligned}\Delta G_{dark}(X_{Br},T) &= \frac{4}{3}\pi r^3 \Delta g_v(X_{Br},T) - \sum_i c_i W_i r^2 \\ &= \frac{4}{3}\pi r^3 [\Delta h_{mix}(X_{Br},T) - T\cdot\Delta s_{mix}(X_{Br},T)] - (1-X_{Br})^{2/3}\cdot 4\pi r^2 \cdot W_1 - 4\pi r^2 \cdot \Delta W_2(X_{Br})\end{aligned} \quad \ldots\ldots(A1)$$

The coefficient, c_i, of the cohesive energies, W_i, accounts for both $CsPbI_3$/$CsPbBr_3$ and $CsPb(Br_xI_{1-x})_3$/$Cs_4Pb(Br_xI_{1-x})_6$ interfaces during phase separation with the values obtained from DFT calculations in Appendix B (*Computational Methods*) with W_1 = 0.42 eV nm^{-2} and $\Delta W_2(X_{Br}) = 0.312\cdot(1-X_{Br})$ eV nm^{-2}. For the $CsPb(Br_xI_{1-x})_3$-dominant thin films, only the interface W_1 between $CsPbI_3$ and $CsPbBr_3$ were considered and ΔW_2 (X_{Br}) was treated as zero. The phase diagram of the alloy could be built by calculating the free energy at 297 K as shown in Figure 3-4 in Chapter 3 text to arrive at similar conclusions of an entropy-driven preference for mixing as in earlier computational studies of mixed-halide perovskites[112,122,123].

A.2 ΔG_{light} for System under Optical Illumination (Photo-Excited State)

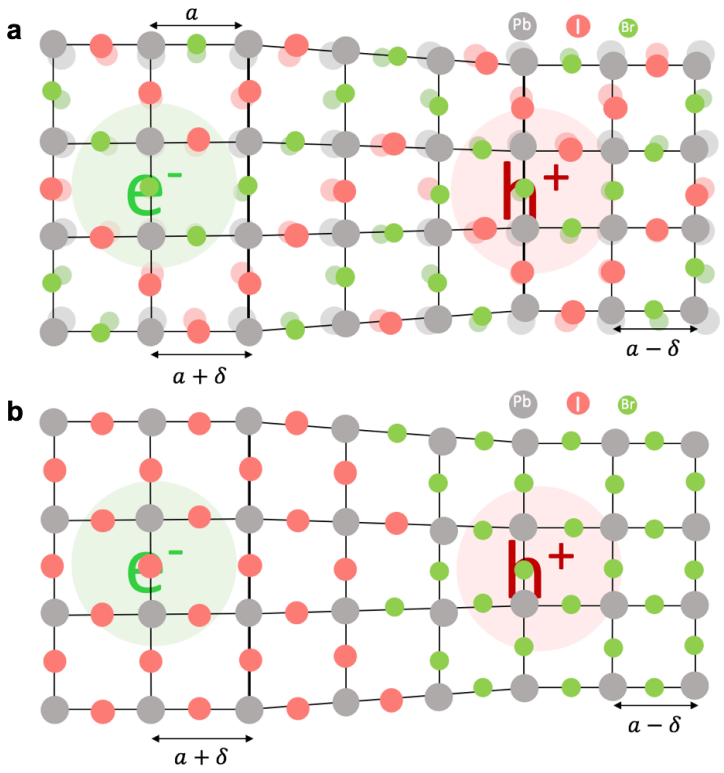

Figure A-1 The distortion of the lattices in the presence of photo-generated carriers were drawn schematically. Only halogen and Pb ions were displayed for simplicity. The e^- and h^+ represented the positive and negative charge carriers generated by photoexcitation. (a) In the ground state (dark), the lattices were displayed by the faded-colored dots with a pseudocubic lattice constant a. Under the light illumination, the lattices were distorted due to the interaction between the free carriers and lattices (forming polarons) with the change of constant $a \pm \delta$. (b) The photoinduced distortion in the lattices would drive the smaller Br^- anions to the lattice-compressed region and the larger I^- anions to the lattice-expanded area to release the localized strain energy. The alloy phase separated into I-rich and Br-rich domains.

The effects of photoexcitation were accounted for by involving the photoinduced polarons[26,48,116,124]. The polarons could bring in excessive strain energy (ΔG_s) on top of the ground-state ΔG_{dark} in Equation A1 due to the locally shortened and lengthened Pb-halogen bonds (Figure A1). When Δg_s (ΔG_s per volume) becomes sufficiently large, the strain energy would be released by de-mixing the halogen anions and forming Br- and I-rich domains (*i.e.*, phase separation). The increased strain energy was calculated as following[114]:

$$\Delta g_s = 4\mu_{mix}\left(\frac{\delta}{a}\right)^2 - (1-X_{Br})\cdot 4\mu_I\left(\frac{(a+\delta)-a_I}{a_I}\right)^2 - X_{Br}\cdot 4\mu_{Br}\left(\frac{(a-\delta)-a_{Br}}{a_{Br}}\right)^2 \quad \text{.....(A2)}$$

where a = 6.29-0.46X_{Br} / a_I = 6.29 / a_{Br} = 5.83 Å (lattice constant values from PDF 01-076-8588, 00-054-0752) is the initial lattice constant for the pseudocubic lattice of $CsPb(Br_xI_{1-x})_3$/$CsPbI_3$/$CsPbBr_3$ in dark, μ = 6.858-0.958X_{Br} / μ_I = 6.858 / μ_{Br} = 5.9 GPa is the shear modulus of the alloy $CsPb(Br_xI_{1-x})_3$/$CsPbI_3$/$CsPbBr_3$ with the numbers adapted from Cahen et al.[125] and Hantezadeh et al. [126], and δ is the change (shrink or expand) in lattice constant after photoexcitation. Therefore, $\Delta G = \Delta G_{light}$ in the excited state was written as:

$$\Delta G_{light}(X_{Br},T) = \Delta G_{dark}(X_{Br},T) + \frac{4}{3}\pi r^3 \cdot \Delta g_s(X_{Br}) \quad \text{.....(A3)}$$

The change of lattice distortion to trigger the phase separation in pure $CsPb(Br_xI_{1-x})_3$ (113) thin film with r = 35 nm was δ = 0.15 Å (weak illumination condition in the manuscript). This value is in reasonable agreement with previous results calculated based on first principle methods[26]. It is worth noting that the cohesive energy between $CsPb(Br_xI_{1-x})_3$ (113) and $Cs_4Pb(Br_xI_{1-x})_6$ (416) was also considered given the spatial confinement from the $Cs_4Pb(Br_xI_{1-x})_6$ (416) matrix (Figure A2).

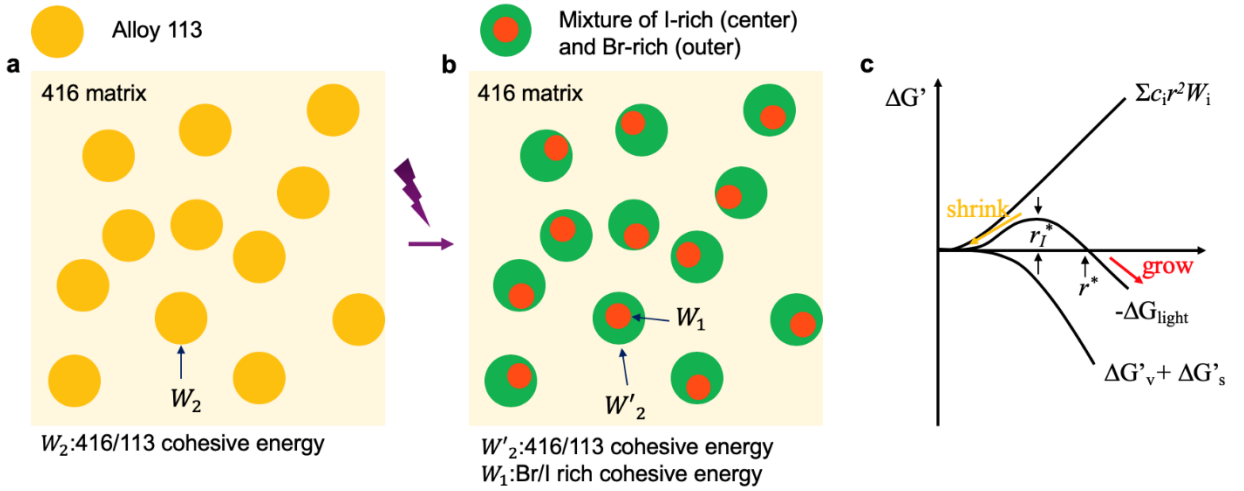

Figure A-2 All the interfaces of the $CsPb(Br_xI_{1-x})_3$/$Cs_4Pb(Br_xI_{1-x})_6$ composites before and after photoinduced phase separation were illustrated by schematics. (a) Nanocrystals of $CsPb(Br_xI_{1-x})_3$ are embedded in the $Cs_4Pb(Br_xI_{1-x})_6$ matrix with only the $CsPb(Br_xI_{1-x})_3$/$Cs_4Pb(Br_xI_{1-x})_6$ interface (cohesive energy W_2). (b) Phase separation occurred under optical illumination with the I-rich domains nucleated in the perovskite nanocrystals. The relative magnitude between the cohesive energy (W'_2 and W_1) is critical to determine the microscopic structures of the phase separation. c. The diagram showed the change of free energy as a function of radius r with the competition between the change of volumetric free energy and the cohesive energy.

A.3 Suppression of Phase Separation with Dominant Cohesive Energy

The phase separation under optical illumination could alternatively be suppressed if the domain size of the mixed-halide perovskites is reduced. The stability could be attributed to the dominating role of the cohesive energy $\Sigma c_i r^2 W_i$ when the surface-to-volume ratio is increased. While all other terms in model are proportional to the volume of the domains ($\propto r^3$), the cohesive energy is a function of the area ($\propto r^2$) (Equation 3.1&3.2 in Chapter 3 and Equation A1~A3). Domains of I-rich phase attempt to nucleate out of the mixed-halide phase (alloy phase). In order for the nucleats to continue to grow (red arrow Figure A2c), the domains of I-rich phase would need to exceed a radius r_I^* to get to the critical size r^* with negative ΔG' (positive ΔG_{light} in the manuscript). Otherwise, the free energy reduced due to the nucleation of I-rich domains would not be sufficient to compensate the free energy increased by creation of interfaces (interfaces as shown in Figure A2a, b); dynamic processes of nucleation and dissolution would then prohibit I-rich phase from growing (yellow arrow in Figure A2c). In other words, if mixed-halide phase has a domain size smaller than the r^*, the lowest energy for I-rich phase would be the $r_I = 0$. I-rich phase would never evolve from alloy mixed-halide phase, leading to suppressed phase separation as indicated by the yellow arrow in Figure A2c. By confining the nanocrystals with $r = 7.5$ nm in the matrix, experimentally, we are able to limit the size of iodine-rich nucleates into a small value with negative ΔG_{light}. The phase separation would not occur regardless of the Br content X_{Br} under the illumination with low intensity (Figure 3-4).

A.4 Illumination-Intensity-Dependent ΔG_{light}

The average lattice distortion δ is expected to increase under stronger photoexcitation[127-129]. When the intensity of polarons is low, the lattice distortion is limited to the localized area. The perturbed region has a size smaller than the critical size for the iodine-rich domains r_I^* to induce phase transformation. The average lattice distortion δ in a unit volume is small resulting in a small Δg_s and negative ΔG_{light}. As the intensity increases, the distorted areas start to interact with each other. It is then probable for the small nucleates to merge and form larger ones. When the intensity is over the threshold, nucleates with the size exceeding the critical radius of iodine-rich domains r_I^* are formed. δ is increased leading to larger Δg_s and positive ΔG_{light}, inducing phase separation. δ is positively related to the light intensity, so are Δg_s and ΔG_{light} as described in Figure A3, before reaching the saturation condition where charge carriers interact strongly with each other. For some Br-rich compositions, the mixed-halide perovskite would remain stable under weak illumination (smaller lattice distortion $\delta = 0.15$ Å), but experience phase separation when the intensity becomes

stronger (larger lattice distortion $\delta = 0.20$ Å). With a fixed size of $CsPb(Br_xI_{1-x})_3$ crystal $r = 7.5$ nm ($d = 15$ nm) in $Cs_4Pb(Br_xI_{1-x})_6$ matrix, the asymmetry of ΔG with respect to X_{Br} originated from the smaller cohesive energies with more Br content, as described in Equation A1 and A3. It's worth noting that, similar intensity dependent phase separation was reported by Kuno's group[112,130], which is consistent with our model.

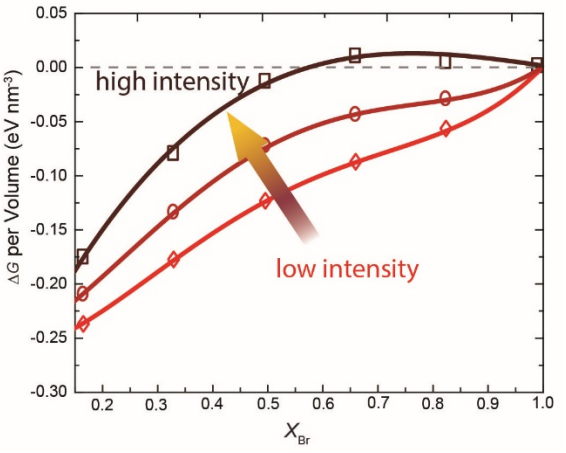

Figure A-3 ΔG_{light} increased as the illumination became stronger.

APPENDIX B
COMPUTATIONAL METHODS TO CALCULATE FREE ENERGY AND COHESIVE ENERGY OF MIXED-HALIDE PEROVSKITE SYSTEMS

B.1 Calculation of Volumetric Gibbs Free Energy of Mixing Δg_v for Ground-State $CsPb(Br_xI_{1-x})_3$

We modeled the mixed-halide perovskite $CsPb(Br_xI_{1-x})_3$ at the ground state (in dark) as a statistical ensemble of independent configurations under seven compositions: X_{Br} = 0, 1/6, 1/3, 1/2, 2/3, 5/6, and 1. This was similar to the treatment of a binary alloy system. The mixing enthalpy, Δh_i (X_{Br}), of each configuration i with ground-state energy, E_i (X_{Br}), was defined as:

$$\Delta h_i(X_{Br}) = E_i(X_{Br}) - (1 - X_{Br})E_{CsPbI_3} - X_{Br}E_{CsPbBr_3} \quad \text{.....(B1)}$$

where E_{CsPbI3} and $E_{CsPbBr3}$ represented the total energies of the pure compounds at the ground state when X_{Br} = 0 and 1, respectively, and both terms were computed in per volume units.

After knowing the mixing enthalpy, Δh_i (X_{Br}), and the degeneracy of each configuration i (due to different combinations of the anion positions under a constant X_{Br}), we could estimate the ensemble (or degeneracy)-averaged mixing enthalpy, Δh_{mix} (X_{Br}, T) as functions of the composition X_{Br} and temperature T accordingly to the Boltzmann distribution:

$$\Delta h_{mix}(X_{Br}, T) = \frac{\sum_i \Delta h_i(X_{Br}) \exp(-\frac{\Delta h_i(X_{Br})}{k_B T})}{\sum_i \exp(-\frac{\Delta h_i(X_{Br})}{k_B T})} \quad \text{.....(B2)}$$

The configuration energies E_i (X_{Br}) were each computed within the framework of Kohn-Sham density functional theory (DFT)[131]. We considered a cubic supercell with 2 × 1 × 1 expansion of a cubic perovskite building block, which corresponds to six halide anions and 10 atoms in total. The total number of configurations for this system was 2^6 = 64. We studied the cubic polymorph based on our experimentally confirmed fact that they all exhibited the cubic polymorph (Figure 3-2a, Figure 3-3 in Chapter 3). For such a cubic inorganic perovskite, the three halide sites are almost equivalent (where the symmetry is greatly enlarged due to the presence of the monoatomic Cs^+ cations), which could reduce the total number of configurations to 21 in total. We took the symmetry-reduced inequivalent configurations and perform a full structural relaxation for each case.

For the DFT total energy calculations, we used the Perdew-Burke-Ernzerhof (PBE)[132] exchange-correlation functional under the Generalized Gradient Approximation (GGA) and the projector augmented-wave (PAW)[133] formalism. A plane-wave cutoff energy of 500 eV and a 6 × 6 × 6 k-point mesh was used for all the configurations. The lattice volume and shape, and the atomic positions of each configuration were fully optimized using a quasi-Newton (variable metric) algorithm[134] to minimize atomic forces below 1.0 meV per Å. The relaxed mixed-halide perovskite configurations at $X_{Br} = 0.5$ are shown in Figure B1a, where the degeneracy was five considering symmetry-reduced inequivalent configurations.

With $\Delta h_{mix}(X_{Br}, T)$ calculated, the volumetric Gibbs free energy of mixing per unit volume in the dark, $\Delta g_v(X_{Br}, T)$ could be directly evaluated:

$$\Delta g_v(X_{Br},T) = \Delta h_{mix}(X_{Br},T) - T\Delta s_{mix}(X_{Br},T) \quad \text{(B3)}$$

where we estimated $\Delta s_{mix}(X_{Br}, T)$ assuming the ideal mixing behavior among halide anions:

$$\Delta s_{mix}(X_{Br},T) = k_B[X_{Br} lnX_{Br} + (1-X_{Br}) ln(1-X_{Br})] \quad \text{(B4)}$$

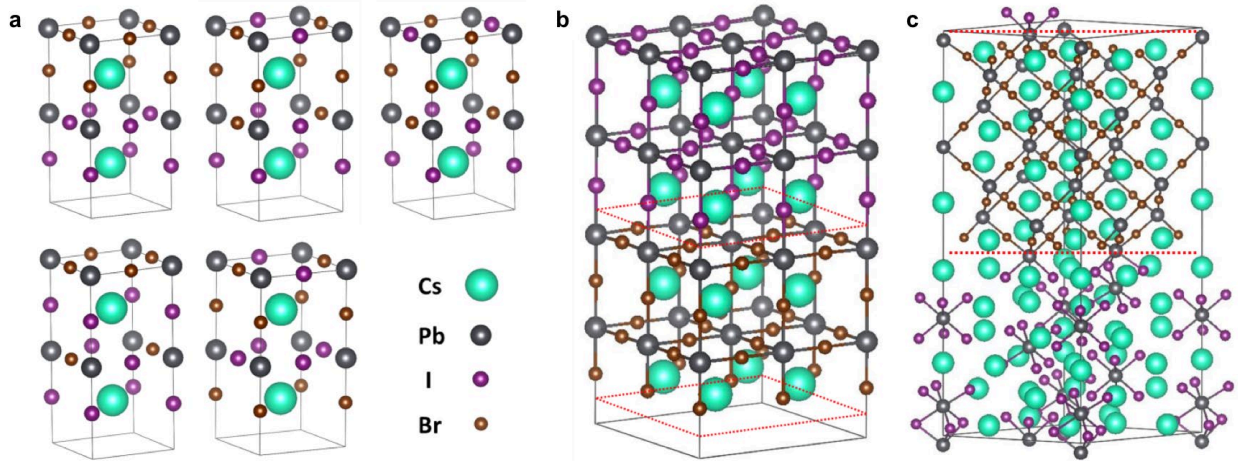

Figure B-1 DFT-relaxed configurations used for the calculations of various parameters were presented. (a) DFT-relaxed symmetry-reduced inequivalent configurations of cubic $CsPb(Br_{0.5}I_{0.5})_3$ with a degeneracy of five were shown. (b) DFT-relaxed configuration of a supercell showed the $CsPbBr_3$-$CsPbI_3$ interfaces as marked by two dotted red rectangles. (c) DFT-relaxed configuration of a supercell exhibited the $CsPbBr_3/Cs_4PbI_6$ interface as marked by two dotted red lines. The (111) surface of the 113 phase (top) and the (100) surface of the 416 phase (bottom) form a well-matched interface with two face-sharing PbX_6 octahedra.

B.2 Computation of Cohesive Energy at the Phase-Separated $CsPbBr_3$-$CsPbI_3$ Interface

To determine the cohesive energy between pure $CsPbBr_3$ and $CsPbI_3$ W_1 (equivalent to interfacial tension), we constructed a supercell (2 × 2 × 2 of $CsPbBr_3$ interfacing with 2 × 2 × 2 of $CsPbI_3$) with an interface between the two pure materials, as shown in Figure B1b. It is important to note that the cohesive energy contains contributions from: (i) the chemical interfacial energy due to chemical potential difference at the interface, and (ii) the strain energy at the interfaces due to slight lattice mismatch between two crystals when they are constrained to have the same lateral dimension in the supercell. The same DFT method and parameters mentioned above were used to relax this supercell, as well as to obtain the optimized configuration and the associated total energy at the ground state, $E_{CsPbI3+CsPbBr3}$. The cohesive energy, W_1, was then calculated as:

$$W_1 = \frac{E_{CsPbI_3+CsPbBr_3} - (E_{CsPbI_3} + E_{CsPbBr_3})}{2A} \quad \text{……(B5)}$$

where E_{CsPbI3} (2 × 2 × 2) and $E_{CsPbBr3}$ (2 × 2 × 2) represent the DFT-computed total energies of the individual pure compounds at the ground state, each with a cell height that is one half of the supercell used to compute $E_{CsPbI3+ CsPbBr3}$, A represents the relaxed interfacial area, and the factor "2" accounts for the two interfaces due to the periodic boundary condition applied in the DFT calculation. With the assumption that the predicted cohesive energy of the ground-state $CsPbBr_3$/$CsPbI_3$ interface does not change after photoexcitation, we obtained a cohesive energy of W_1 = 0.42 eV nm^{-2} at the $CsPbI_3$/$CsPbBr_3$ interface with 0.366 eV nm^{-2} contributed from the strain at the interface. The Young's modulus used for strain calculations for $CsPbBr_3$ and $CsPbI_3$ are 15.8 and 14.49 GPa[125,135] and Poisson's Ratios are 0.33 and 0.32 respectively. Compared with the cubic structure, other non-cubic perovskite crystal structures of $CsPbI_3$/$CsPbBr_3$ such as orthorhombic structure due to different synthesis protocols have lower symmetry. An increase the cohesive energy (chemical + interfacial strain) would be expected in general.

B.3 Computation of Cohesive Energy at the $CsPbX_3$-Cs_4PbX_6 Interface

The similar DFT method based on Supplementary Equation 8 was used to determine the cohesive energy W_2 between the initial $CsPb(Br_xI_{1-x})_3$ (nanocrystal 113) and $Cs_4Pb(Br_xI_{1-x})_6$ (matrix 416) phases, as well as the cohesive energy W_2' between Br-rich $CsPbBr_3$ and $Cs_4Pb(Br_xI_{1-x})_6$ after phase separation. As shown in Figure B1c, the interface between the cubic $CsPbBr_3$ phase (the (111) surface) and the hexagonal Cs_4PbI_6 phase (the (100) surface) is illustrated as an example. The $CsPbBr_3$/Cs_4PbBr_6, $CsPbBr_3$/Cs_4PbI_6, $CsPbI_3$/Cs_4PbI_6 and $CsPbI_3$/Cs_4PbBr_6 interfaces were all

relaxed and equilibrated using DFT calculations based on the reported crystallographic surfaces in an earlier work[111]. The computed cohesive energies W_2 were 0.373, 0.686, 0.375, and 1.374 eV nm^{-2}, respectively, for the pure $CsPbBr_3/Cs_4PbBr_6$, $CsPbBr_3/Cs_4PbI_6$, $CsPbI_3/Cs_4PbI_6$, and $CsPbI_3/Cs_4PbBr_6$ interfaces. The energy contributions from strain at the interfaces were calculated as 0.179, 0.051, 0.239 and 1.347 eV nm^{-2}, respectively, for the pure $CsPbBr_3/Cs_4PbBr_6$, $CsPbBr_3/Cs_4PbI_6$, $CsPbI_3/Cs_4PbI_6$, and $CsPbI_3/Cs_4PbBr_6$ interfaces. The Young's modulus of Cs_4PbBr_6, Cs_4PbI_6 used for calculations are 14.4 and 11.2 GPa adapted from Hu et al.[136] with Poisson ratios 0.2 and 0.19, respectively.

The $CsPbBr_3/Cs_4PbX_6$ interface is preferred over the interface of $CsPbI_3/Cs_4PbX_6$ due to the much smaller cohesive energy between $CsPbBr_3$ and Cs_4PbX_6. The nucleation of I-rich domains was reported previously in mixed-halide perovskites[48,137]. It is likely that the new I-rich phase starts to nucleate inside each alloy nanocrystal, making the matrix Cs_4PbX_6 (416) phase interface with a Br-rich $CsPbX_3$ (113) phase in the outer region of the nanoparticle, as illustrated in Figure A2. The change of bandgap measured and lattice constant with the composition indicated that 113 and 416 species shared the similar X_{Br} (Figure 3-2, Figure 3-3c and Figure 3-3f). Therefore, we could assume that the interface between $CsPb(Br_xI_{1-x})_3$ and $Cs_4Pb(Br_xI_{1-x})_6$ changed into the interface between the Br-rich 113 phase $CsPbBr_3$ and the initial 416 $Cs_4Pb(Br_xI_{1-x})_6$ matrix. Therefore, a cohesive energy change, $\Delta W_2 = (W_2' - W_2)$, is expected upon phase separation in $CsPbX_3$. Since the calculated $W_2(CsPbI_3/Cs_4PbI_6) = 0.375$ eV nm^{-2} is very close to $W_2(CsPbBr_3/Cs_4PbBr_6) = 0.373$ eV nm^{-2}, it is reasonable to assume that $W_2[CsPb(Br_xI_{1-x})_3/Cs_4Pb(Br_xI_{1-x})_6)]$ is a constant of (0.373 + 0.375)/2 = 0.374 eV nm^{-2}, when 113 and 416 are under the same initial X_{Br} value. Therefore, the halide composition dependent change of the cohesive energy was approximately calculated using the linear relation:

$$\begin{aligned}
&\Delta W_2(X_{Br}) = W_2'(X_{Br}) - W_2(X_{Br}) \\
&= (1 - X_{Br}) \cdot [W_2(CsPbBr_3 / Cs_4PbI_6) - W_2(CsPb(Br_{X_{Br}} I_{1-X_{Br}})_3 / Cs_4Pb(Br_{xBr} I_{1-xBr})_6)] \\
&= (1 - X_{Br}) \cdot (0.686 - 0.374) eV / nm^2 \\
&= 0.312 \cdot (1 - X_{Br}) eV / nm^2
\end{aligned} \quad \text{……(B6)}$$

The lattices match better between $Cs_4Pb(I_{1-x}Br_x)_6$ and the cubic $CsPb(I_{1-x}Br_x)_3$ compared with other lower-symmetric structures of $CsPb(I_{1-x}Br_x)_3$, such as the orthorhombic structure. Accordingly, the cohesive energy at the $Cs_4Pb(I_{1-x}Br_x)_6$/cubic $CsPb(I_{1-x}Br_x)_3$ interface should be the lowest. Other perovskite structures with lower symmetry (e.g. orthorhombic) would increase

the cohesive energy and make the phase separation less favorable in energy. With a large surface-to-volume ratio and the interfaces between $CsPb(I_{1-x}Br_x)_3/Cs_4Pb(I_{1-x}Br_x)_6$ plays a significant role in the phase stability, the cubic $CsPb(I_{1-x}Br_x)_3$ is the preferred structure with the least amount of cohesive energy. Initial PL spectra of $CsPb(Br_{0.5}I_{0.5})_3/Cs_4Pb(Br_{0.5}I_{0.5})_6$ as a function of temperature showed no signs of phase transition of the cubic-phase perovskite nanocrystals in the composite thin films (Figure B2).

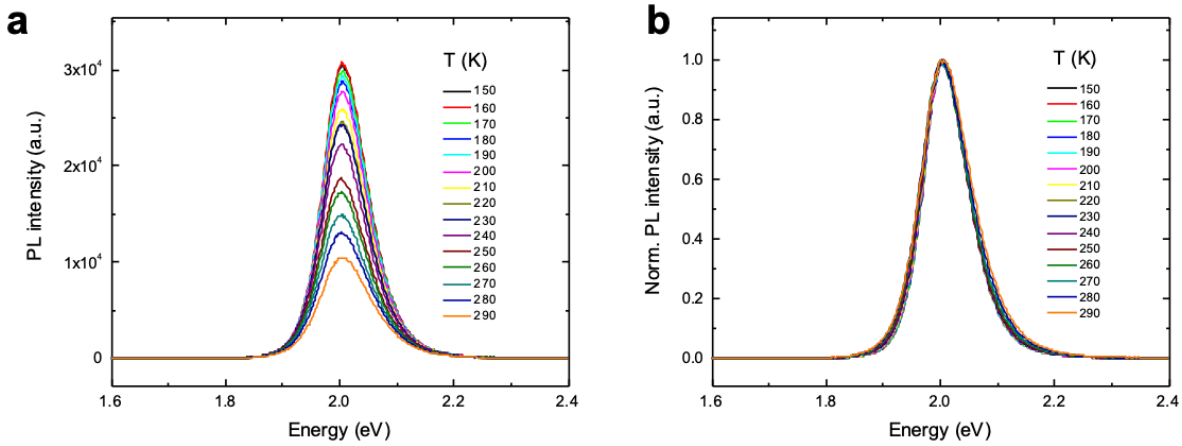

Figure B-2 Initial PL spectra of $CsPb(Br_{0.5}I_{0.5})_3$/ $Cs_4Pb(Br_{0.5}I_{0.5})_6$ as a function of temperature showed no signs of phase transition of the cubic-phase perovskite nanocrystals in the composite thin film. (a) absolute values of PL. (b) Normalized PL spectra.

APPENDIX C
LED DEVICE FABRICATION

Device Fabrication: Indium tin oxide (ITO)-coated glass substrates were cleaned sequentially by sonication in 1% Alconox precision cleaner solution, distilled water, acetone, and isopropyl alcohol for 15 min followed by UV ozone treatment for 20 min before use. The PEDOT:PSS solution was filtered by 5 μm poly(tetrafluoroethylene) syringe filters before use. The PEDOT:PSS solution was spin-coated onto ITO substrates at 4000 rpm for 53 s, then annealed at 135°C for 20 min in air. The substrates were then coated with the $CsPbBr_3|Cs_4PbBr_6$ composite perovskite emissive layer (60 nm). Finally, TPBi (40 nm), LiF (1.2 nm), and Al (100 nm) layers were deposited sequentially using thermal evaporation through shadow masks at a rate of 1.0, 0.03, and 4 Å s^{-1}, respectively, under high vacuum ($<3\times10^{-6}$ Torr).

REFERENCES

(1) National Center for Photovoltaics. *NREL Best Research-Cell Efficiencies Chart*; 2014.

(2) Ling, Y.; Yuan, Z.; Tian, Y.; Wang, X.; Wang, J. C.; Xin, Y.; Hanson, K.; Ma, B.; Gao, H. *Adv. Mater.* **2015**, *28* (2), 305–311.

(3) Tan, Z.-K. *Nature Nanotechnology* **2014**, *9* (9), 687–692.

(4) Li, J.; Shan, X.; Bade, S. G. R.; Geske, T.; Jiang, Q.; Yang, X.; Yu, Z. *J. Phys. Chem. Lett.* **2016**, *7* (20), 4059–4066.

(5) Ling, Y.; Tian, Y.; Wang, X.; Wang, J. C.; Knox, J. M.; Perez-Orive, F.; Du, Y.; Tan, L.; Hanson, K.; Ma, B.; Gao, H. *Adv. Mater.* **2016**, *28* (40), 8983–8989.

(6) Fang, Y.; Dong, Q.; Shao, Y.; Yuan, Y.; Huang, J. *Nature Photonics* **2015**, *9* (10), 679–686.

(7) Zhu, H.; Fu, Y.; Meng, F.; Wu, X.; Gong, Z.; Ding, Q.; Gustafsson, M. V.; Trinh, M. T.; Jin, S.; Zhu, X. Y. *Nat Mater* **2015**, *14* (6), 636–642.

(8) Xing, G.; Mathews, N.; Lim, S. S.; Yantara, N.; Liu, X.; Sabba, D.; Grätzel, M.; Mhaisalkar, S.; Sum, T. C. *Nat Mater* **2014**, *13* (5), 476–480.

(9) Snaith, H. J.; Abate, A.; Ball, J. M.; Eperon, G. E.; Leijtens, T.; Noel, N. K.; Stranks, S. D.; Wang, J. T.-W.; Wojciechowski, K.; Zhang, W. *J. Phys. Chem. Lett.* **2014**, *5* (9), 1511–1515.

(10) Hoke, E. T.; Slotcavage, D. J.; Dohner, E. R.; Bowring, A. R.; Karunadasa, H. I.; McGehee, M. D. *Chemical Science* **2015**, *6* (1), 613–617.

(11) deQuilettes, D. W.; Zhang, W.; Burlakov, V. M.; Graham, D. J.; Leijtens, T.; Osherov, A.; Bulović, V.; Snaith, H. J.; Ginger, D. S.; Stranks, S. D. *Nature Communications* **2016**, *7*, 11683.

(12) Wang, X.; Ling, Y.; Chiu, Y.-C.; Du, Y.; Barreda, J. L.; Perez-Orive, F.; Ma, B.; Xiong, P.; Gao, H. *Nano Lett.* **2017**, *17* (8), 4831–4839.

(13) Wang, X.; Ling, Y.; Lian, X.; Xin, Y.; Dhungana, K. B.; Perez-Orive, F.; Knox, J.; Chen, Z.; Zhou, Y.; Beery, D.; Hanson, K.; Shi, J.; Lin, S.; Gao, H. *Nature Communications* **2019**, *10* (1), 695.

(14) Ling, Y.; Tan, L.; Wang, X.; Zhou, Y.; Xin, Y.; Ma, B.; Hanson, K.; Gao, H. *J. Phys. Chem. Lett.* **2017**, *8* (14), 3266–3271.

(15) Lian, X.; Wang, X.; Ling, Y.; Lochner, E.; Tan, L.; Zhou, Y.; Ma, B.; Hanson, K.; Gao, H. *Adv. Funct. Mater.* **2018**, 1807345–1807347.

(16) Wang, X.; Gao, H. *Nano Lett.* **2015**, *15* (10), 7037–7042.

(17) Wei, H.; Fang, Y.; Mulligan, P.; Chuirazzi, W.; Fang, H.-H.; Wang, C.; Ecker, B. R.; Gao, Y.; Loi, M. A.; Cao, L.; Huang, J. *Nature Photonics* **2016**, *10* (5), 333–339.

(18) Wei, H.; DeSantis, D.; Wei, W.; Deng, Y.; Guo, D.; Savenije, T. J.; Cao, L.; Huang, J. *Nat Mater* **2017**, *16* (8), 826–833.

(19) Chen, Q.; Wu, J.; Ou, X.; Huang, B.; Almutlaq, J.; Zhumekenov, A. A.; Guan, X.; Han, S.; Liang, L.; Yi, Z.; Li, J.; Xie, X.; Wang, Y.; Li, Y.; Fan, D.; Teh, D. B. L.; All, A. H.; Mohammed, O. F.; Bakr, O. M.; Wu, T.; Bettinelli, M.; Yang, H.; Huang, W.; Liu, X. *Nature* **2018**, *561* (7721), 88–93.

(20) Gu, C.; Lee, J.-S. *ACS Nano* **2016**, *10* (5), 5413–5418.

(21) Rossel, C. *Europhysics News* **2018**, *49* (3), 10–14.

(22) Brivio, F.; Butler, K. T.; Walsh, A.; van Schilfgaarde, M. *Phys. Rev. B* **2014**, *89* (15), 155204–155206.

(23) Stranks, S. D.; Snaith, H. J. *Nature Nanotechnology* **2015**, *10* (5), 391–402.

(24) Li, Z.; Klein, T. R.; Kim, D. H.; Yang, M.; Berry, J. J.; van Hest, M. F. A. M.; Zhu, K. *Nat. Rev. Mater.* **2018**, *3* (4), 18017–18020.

(25) Ferreira, A. C.; Létoublon, A.; Paofai, S.; Raymond, S.; Ecolivet, C.; Rufflé, B.; Cordier, S.; Katan, C.; Saidaminov, M. I.; Zhumekenov, A. A.; Bakr, O. M.; Even, J.; Bourges, P. *Phys. Rev. Lett.* **2018**, *121* (8), 085502.

(26) Miyata, K.; Meggiolaro, D.; Trinh, M. T.; Joshi, P. P.; Mosconi, E.; Jones, S. C.; De Angelis, F.; Zhu, X. Y. *Science Advances* **2017**, *3* (8), e1701217.

(27) Yuan, Y.; Huang, J. *Acc. Chem. Res.* **2016**, *49* (2), 286–293.

(28) Marronnier, A.; Lee, H.; Geffroy, B.; Even, J.; Bonnassieux, Y.; Roma, G. *J. Phys. Chem. Lett.* **2017**, *8* (12), 2659–2665.

(29) Green, M. A.; Ho-Baillie, A.; Snaith, H. J. *Nature Photonics* **2014**, *8* (7), 506–514.

(30) Buin, A.; Pietsch, P.; Xu, J.; Voznyy, O.; Ip, A. H.; Comin, R.; Sargent, E. H. *Nano Lett.* **2014**, *14* (11), 6281–6286.

(31) Lu, D.; Zhang, Y.; Lai, M.; Lee, A.; Xie, C.; Lin, J.; Lei, T.; Lin, Z.; Kley, C. S.; Huang, J.; Rabani, E.; Yang, P. *Nano Lett.* **2018**, *18* (11), 6967–6973.

(32) Meggiolaro, D.; De Angelis, F. *ACS Energy Lett.* **2018**, *3* (9), 2206–2222.

(33) Heo, S.; Seo, G.; Lee, Y.; Lee, D.; Seol, M.; Lee, J.; Park, J.-B.; Kim, K.; Yun, D.-J.; Kim, Y. S.; Shin, J. K.; Ahn, T. K.; Nazeeruddin, M. K. *Energy Environ. Sci.* **2017**, *10* (5), 1128–1133.

(34) deQuilettes, D. W.; Vorpahl, S. M.; Stranks, S. D.; Nagaoka, H.; Eperon, G. E.; Ziffer, M. E.; Snaith, H. J.; Ginger, D. S. *Science* **2015**, *348* (6235), 683–686.

(35) Akkerman, Q. A.; Rainò, G.; Kovalenko, M. V.; Manna, L. *Nat Mater* **2018**, *17* (5), 394–405.

(36) Mei, Y.; Zhang, C.; Vardeny, Z. V.; Jurchescu, O. D. *MRC* **2015**, *5* (2), 297–301.

(37) Giorgi, G.; Fujisawa, J.-I.; Segawa, H.; Yamashita, K. *J. Phys. Chem. Lett.* **2013**, *4* (24), 4213–4216.

(38) Stranks, S. D.; Eperon, G. E.; Grancini, G.; Menelaou, C.; Alcocer, M. J. P.; Leijtens, T.; Herz, L. M.; Petrozza, A.; Snaith, H. J. *Science* **2013**, *342* (6156), 341–344.

(39) Dong, Q.; Fang, Y.; Shao, Y.; Mulligan, P.; Qiu, J.; Cao, L.; Huang, J. *Science* **2015**, *347* (6225), 967–970.

(40) Protesescu, L.; Yakunin, S.; Bodnarchuk, M. I.; Krieg, F.; Caputo, R.; Hendon, C. H.; Yang, R. X.; Walsh, A.; Kovalenko, M. V. *Nano Lett.* **2015**, *15* (6), 3692–3696. (https://pubs.acs.org/doi/10.1021/nl5048779)

(41) Zhang, D.; Yang, Y.; Bekenstein, Y.; Yu, Y.; Gibson, N. A.; Wong, A. B.; Eaton, S. W.; Kornienko, N.; Kong, Q.; Lai, M.; Alivisatos, A. P.; Leone, S. R.; Yang, P. *J. Am. Chem. Soc.* **2016**, *138* (23), 7236–7239.

(42) Zhang, F.; Zhong, H.; Chen, C.; Wu, X.-G.; Hu, X.; Huang, H.; Han, J.; Zou, B.; Dong, Y. *ACS Nano* **2015**, *9* (4), 4533–4542.

(43) Levchuk, I.; Osvet, A.; Tang, X.; Brandl, M.; Perea, J. D.; Hoegl, F.; Matt, G. J.; Hock, R.; Batentschuk, M.; Brabec, C. J. *Nano Lett.* **2017**, *17* (5), 2765–2770.

(44) Anaya, M.; Lozano, G.; Calvo, M. E.; Míguez, H. *Joule* **2017**, *1* (4), 769–793.

(45) Song, J.; Li, J.; Li, X.; Xu, L.; Dong, Y.; Zeng, H. *Adv. Mater.* **2015**, *27* (44), 7162–7167.

(46) Xiao, Z.; Zhao, L.; Tran, N. L.; Lin, Y. L.; Silver, S. H.; Kerner, R. A.; Yao, N.; Kahn, A.; Scholes, G. D.; Rand, B. P. *Nano Lett.* **2017**, *17* (11), 6863–6869.

(47) Beal, R. E.; Slotcavage, D. J.; Leijtens, T.; Bowring, A. R.; Belisle, R. A.; Nguyen, W. H.; Burkhard, G. F.; Hoke, E. T.; McGehee, M. D. *J. Phys. Chem. Lett.* **2016**, *7* (5), 746–751.

(48) Bischak, C. G.; Hetherington, C. L.; Wu, H.; Aloni, S.; Ogletree, D. F.; Limmer, D. T.; Ginsberg, N. S. *Nano Lett.* **2017**, *17* (2), 1028–1033.

(49) Yoon, S. J.; Draguta, S.; Manser, J. S.; Sharia, O.; Schneider, W. F.; Kuno, M.; Kamat, P. V. *ACS Energy Lett.* **2016**, *1* (1), 290–296.

(50) Wang, Y.; Chen, Z.; Deschler, F.; Sun, X.; Lu, T.-M.; Wertz, E. A.; Hu, J.-M.; Shi, J. *ACS Nano* **2017**, *11* (3), 3355–3364.

(51) Slotcavage, D. J.; Karunadasa, H. I.; McGehee, M. D. *ACS Energy Lett.* **2016**, *1* (6), 1199–1205.

(52) Brennan, M. C.; Draguta, S.; Kamat, P. V.; Kuno, M. *ACS Energy Lett.* **2017**, *3* (1), 204–213. (https://pubs.acs.org/doi/abs/10.1021/acsenergylett.7b01151)

(53) Choi, T.; Lee, S.; Choi, Y. J.; Kiryukhin, V.; Cheong, S.-W. *Science* **2009**, *324* (5923), 63–66.

(54) Frost, J. M.; Butler, K. T.; Walsh, A. *APL Materials* **2014**, *2* (8), 081506–081511.

(55) Quarti, C.; Mosconi, E.; De Angelis, F. *Chem. Mater.* **2014**, *26* (22), 6557–6569.

(56) Xiao, Z.; Yuan, Y.; Shao, Y.; Wang, Q.; Dong, Q.; Bi, C.; Sharma, P.; Gruverman, A.; Huang, J. *Nat Mater* **2014**, *14* (2), 193–198.

(57) Yang, T.-Y.; Gregori, G.; Pellet, N.; Grätzel, M.; Maier, J. *Angew. Chem.* **2015**, *127* (27), 8016–8021.

(58) Meggiolaro, D.; Mosconi, E.; De Angelis, F. *ACS Energy Lett.* **2019**, *4* (3), 779–785.

(59) Walsh, A.; Stranks, S. D. *ACS Energy Lett.* **2018**, *3* (8), 1983–1990.

(60) Eames, C.; Frost, J. M.; Barnes, P. R. F.; O'Regan, B. C.; Walsh, A.; Islam, M. S. *Nature Communications* **2015**, *6* (1), 7497.

(61) Azpiroz, J. M.; Mosconi, E.; Bisquert, J.; De Angelis, F. *Energy Environ. Sci.* **2015**, *8* (7), 2118–2127.

(62) Haruyama, J.; Sodeyama, K.; Han, L.; Tateyama, Y. *J. Am. Chem. Soc.* **2015**, *137* (32), 10048–10051.

(63) Song, J.; Li, J.; Li, X.; Xu, L.; Dong, Y.; Zeng, H. *Adv. Mater.* **2015**, *27* (44), 7162–7167.

(64) Brennan, M. C.; Draguta, S.; Kamat, P. V.; Kuno, M. *ACS Energy Lett.* **2017**, *3* (1), 204–213.

(65) Stoumpos, C. C.; Kanatzidis, M. G. *Acc. Chem. Res.* **2015**, *48* (10), 2791–2802.

(66) Ahmad, W.; Khan, J.; Niu, G.; Tang, J. *Sol. RRL* **2017**, *1* (7), 1700048.

(67) Shockley, W.; Queisser, H. J. *Journal of Applied Physics* **1961**, *32* (3), 510–519.

(68) Lai, M.; Kong, Q.; Bischak, C. G.; Yu, Y.; Dou, L.; Eaton, S. W.; Ginsberg, N. S.; Yang, P. *Nano Res.* **2017**, *10* (4), 1107–1114.

(69) Swarnkar, A.; Marshall, A. R.; Sanehira, E. M.; Chernomordik, B. D.; Moore, D. T.; Christians, J. A.; Chakrabarti, T.; Luther, J. M. *Science* **2016**, *354* (6308), 92–95.

(70) Zhao, B.; Jin, S.-F.; Huang, S.; Liu, N.; Ma, J.-Y.; ORCID: 0000-0002-7599-0008, D.-J. X.; Han, Q.; Ding, J.; Ge, Q.-Q.; Feng, Y.; ORCID: 0000-0002-6268-0959, J.-S. H. *J. Am. Chem. Soc.* **2018**, 1–10.

(71) Zhao, B.; Jin, S.-F.; Huang, S.; Liu, N.; Ma, J.-Y.; Xue, D.-J.; Han, Q.; Ding, J.; Ge, Q.-Q.; Feng, Y.; Hu, J.-S. *J. Am. Chem. Soc.* **2018**, *140* (37), 11716–11725.

(72) Nie, W.; Blancon, J.-C.; Neukirch, A. J.; Appavoo, K.; Tsai, H.; Chhowalla, M.; Alam, M. A.; Sfeir, M. Y.; Katan, C.; Even, J.; Tretiak, S.; Crochet, J. J.; Gupta, G.; Mohite, A. D. *Nature Communications* **2016**, *7*, 11574.

(73) Dualeh, A.; Moehl, T.; Tétreault, N.; Teuscher, J.; Gao, P.; Nazeeruddin, M. K.; Grätzel, M. *ACS Nano* **2013**, *8* (1), 362–373.

(74) Pockett, A.; Eperon, G. E.; Peltola, T.; Snaith, H. J.; Walker, A.; Peter, L. M.; Cameron, P. J. *J. Phys. Chem. C* **2015**, *119* (7), 3456–3465.

(75) Tress, W.; Marinova, N.; Moehl, T.; Zakeeruddin, S. M.; Nazeeruddin, M. K.; Gratzel, M. *Energy Environ. Sci.* **2015**, *8*, 995–1004.

(76) Wu, B.; Fu, K.; Yantara, N.; Xing, G.; Sun, S.; Sum, T. C.; Mathews, N. *Adv. Energy Mater.* **2015**, *5* (19), 1500829–8.

(77) Yuan, Y.; Chae, J.; Shao, Y.; Wang, Q.; Xiao, Z.; Centrone, A.; Huang, J. *Adv. Energy Mater.* **2015**, *5* (15), 1500615–1500617.

(78) Yuan, Y.; Wang, Q.; Shao, Y.; Lu, H.; Li, T.; Gruverman, A.; Huang, J. *Adv. Energy Mater.* **2015**, *6* (2), 1501803–1501807.

(79) Zhang, Y.; Wang, Y.; Xu, Z.-Q.; Liu, J.; Song, J.; Xue, Y.; Wang, Z.; Zheng, J.; Jiang, L.; Zheng, C.; Huang, F.; Sun, B.; Cheng, Y.-B.; Bao, Q. *ACS Nano* **2016**, *10* (7), 7031–7038.

(80) Graham, R.; Yu, D. *Mod. Phys. Lett. B* **2013**, *27* (25), 1330018–1330018.

(81) Allen, J. E.; Hemesath, E. R.; Lauhon, L. J. *Nano Lett.* **2009**, *9* (5), 1903–1908.

(82) Ahn, Y.; Dunning, J.; Park, J. *Nano Lett.* **2005**, *5* (7), 1367–1370.

(83) Strasfeld, D. B.; Dorn, A.; Wanger, D. D.; Bawendi, M. G. *Nano Lett.* **2012**, *12* (2), 569–575.

(84) Freitag, M.; Tsang, J. C.; Bol, A.; Yuan, D.; Liu, J.; Avouris, P. *Nano Lett.* **2007**, *7* (7), 2037–2042.

(85) Allen, J. E.; Perea, D. E.; Hemesath, E. R.; Lauhon, L. J. *Adv. Mater.* **2009**, *21* (30), 3067–3072.

(86) Xu, X.; Gabor, N. M.; Alden, J. S.; van der Zande, A. M.; McEuen, P. L. *Nano Lett.* **2010**, *10* (2), 562–566.

(87) Yoon, K.; Hyun, J. K.; Connell, J. G.; Amit, I.; Rosenwaks, Y.; Lauhon, L. J. *Nano Lett.* **2013**, *13* (12), 6183–6188.

(88) Melitz, W.; Shen, J.; Kummel, A. C.; Lee, S. *Surface Science Reports* **2011**, *66* (1), 1–27.

(89) Zhang, W.; Saliba, M.; Moore, D. T.; Pathak, S. K.; Hörantner, M. T.; Stergiopoulos, T.; Stranks, S. D.; Eperon, G. E.; Alexander-Webber, J. A.; Abate, A.; Sadhanala, A.; Yao, S.; Chen, Y.; Friend, R. H.; Estroff, L. A.; Wiesner, U.; Snaith, H. J. *Nature Communications* **2015**, *6* (1), 6142.

(90) Dymshits, A.; Henning, A.; Segev, G.; Rosenwaks, Y.; Etgar, L. *Scientific Reports* **2015**, *5* (1), 7837–6.

(91) Gu, Y.; Romankiewicz, J. P.; David, J. K.; Lensch, J. L.; Lauhon, L. J. *Nano Lett.* **2006**, *6* (5), 948–952.

(92) Matyba, P.; Maturova, K.; Kemerink, M.; Robinson, N. D.; Edman, L. *Nat Mater* **2009**, *8* (8), 672–676.

(93) Kuang, X.; Green, M. A.; Niu, H.; Zajdel, P.; Dickinson, C.; Claridge, J. B.; Jantsky, L.; Rosseinsky, M. J. *Nat Mater* **2008**, *7* (6), 498–504.

(94) Sze, S. M.; Coleman, D. J., Jr.; Loya, A. *Solid-State Electronics* **1971**, *14* (12), 1209–1218.

(95) Chen, Y.; Yi, H. T.; Wu, X.; Haroldson, R.; Gartstein, Y. N.; Rodionov, Y. I.; Tikhonov, K. S.; Zakhidov, A.; Zhu, X. Y.; Podzorov, V. *Nature Communications* **2016**, *7* (1), 12253.

(96) Stoumpos, C. C.; Malliakas, C. D.; Kanatzidis, M. G. *Inorg. Chem.* **2013**, *52* (15), 9019–9038.

(97) Milot, R. L.; Eperon, G. E.; Snaith, H. J.; Johnston, M. B.; Herz, L. M. *Adv. Funct. Mater.* **2015**, *25* (39), 6218–6227.

(98) Dignam, M. J. *Journal of Physics and Chemistry of Solids* **1968**, *29* (2), 249–260.

(99) Dignam, M. J.; Gibbs, D. B. *Journal of Physics and Chemistry of Solids* **1969**, *30* (2), 375–393.

(100) Strukov, D. B.; Williams, R. S. *Appl. Phys. A* **2008**, *94* (3), 515–519.

(101) Lang, D. V. *Journal of Applied Physics* **1974**, *45* (7), 3023–3032.

(102) Chen, Q.; Zhou, H.; Hong, Z.; Luo, S.; Duan, H.-S.; Wang, H.-H.; Liu, Y.; Li, G.; Yang, Y. *J. Am. Chem. Soc.* **2014**, *136* (2), 622–625.

(103) Ha, S. T.; Liu, X.; Zhang, Q.; Giovanni, D.; Sum, T. C.; Xiong, Q. *Advanced Optical Materials* **2014**, *2* (9), 838–844.

(104) Gargas, D. J.; Gao, H.; Wang, H.; Yang, P. *Nano Lett.* **2011**, *11* (9), 3792–3796.

(105) Janotti, A.; Van de Walle, C. G. *Rep. Prog. Phys.* **2009**, *72* (12), 126501–126530.

(106) Al-Sabahi, J.; Bora, T.; Al-Abri, M.; Dutta, J. *Materials* **2016**, *9* (4), 238–10.

(107) Chung, D. D. L. *Polymer Polymer Composites* **2000**, *8*, 219–229.

(108) Boyd, C. C.; Cheacharoen, R.; Leijtens, T.; McGehee, M. D. *Chem. Rev.* **2019**, *119* (5), 3418–3451.

(109) Cho, H.; Kim, Y.-H.; Wolf, C.; Lee, H.-D.; Lee, T.-W. *Adv. Mater.* **2018**, *350*, 1704587–24.

(110) Akkerman, Q. A.; Park, S.; Radicchi, E.; Nunzi, F.; Mosconi, E.; De Angelis, F.; Brescia, R.; Rastogi, P.; Prato, M.; Manna, L. *Nano Lett.* **2017**, *17* (3), 1924–1930. (https://pubs.acs.org/doi/abs/10.1021%2Facs.nanolett.6b05262)

(111) Quan, L. N.; Quintero-Bermudez, R.; Voznyy, O.; Walters, G.; Jain, A.; Fan, J. Z.; Zheng, X.; Yang, Z.; Sargent, E. H. *Adv. Mater.* **2017**, *29* (21), 1605945–1605946.

(112) Draguta, S.; Sharia, O.; Yoon, S. J.; Brennan, M. C.; Morozov, Y. V.; Manser, J. S.; Kamat, P. V.; Schneider, W. F.; Kuno, M. *Nature Communications* **2017**, *8* (1), 200.

(113) Lin, Q.; Wang, Z.; Snaith, H. J.; Johnston, M. B.; Herz, L. M. *Adv. Sci.* **2018**, *5* (4), 1700792–1700798.

(114) Porter, D. A.; Easterling, K. E. *Phase Transformations in Metals and Alloys*; Springer US: Boston, MA, 1992; pp 1–528.

(115) Batignani, G.; Fumero, G.; Srimath Kandada, A. R.; Cerullo, G.; Gandini, M.; Ferrante, C.; Petrozza, A.; Scopigno, T. *Nature Communications* **2018**, *9* (1), 1971.

(116) Bretschneider, S. A.; Ivanov, I.; Wang, H. I.; Miyata, K.; Zhu, X.; Bonn, M. *Adv. Mater.* **2018**, *338*, 1707312–1707318.

(117) Woo, H. C.; Choi, J. W.; Shin, J.; Chin, S.-H.; Ann, M. H.; ORCID: 0000-0002-1336-4589, C.-L. L. *J. Phys. Chem. Lett.* **2018**, *9*, 4066–4074.

(118) Li, X.; Wu, Y.; Zhang, S.; Cai, B.; Gu, Y.; Song, J.; Zeng, H. *Adv. Funct. Mater.* **2016**, *26* (15), 2435–2445.

(119) Shibata, H. *Jpn. J. Appl. Phys.* **1998**, *37* (Part 1, No. 2), 550–553.

(120) Manser, J. S.; Saidaminov, M. I.; Christians, J. A.; Bakr, O. M.; Kamat, P. V. *Acc. Chem. Res.* **2016**, *49* (2), 330–338.

(121) Bischak, C. G.; Wong, A. B.; Lin, E.; Limmer, D. T.; Yang, P.; Ginsberg, N. S. *J. Phys. Chem. Lett.* **2018**, *9* (14), 3998–4005.

(122) Brivio, F.; Caetano, C.; Walsh, A. *J. Phys. Chem. Lett.* **2016**, *7* (6), 1083–1087.

(123) Yin, W.-J.; Yan, Y.; Wei, S.-H. *J. Phys. Chem. Lett.* **2014**, *5* (21), 3625–3631.

(124) Ivanovska, T.; Dionigi, C.; Mosconi, E.; De Angelis, F.; Liscio, F.; Morandi, V.; Ruani, G. *J. Phys. Chem. Lett.* **2017**, *8* (13), 3081–3086.

(125) Rakita, Y.; Cohen, S. R.; Kedem, N. K.; Hodes, G.; Cahen, D. *MRC* **2015**, *5* (04), 623–629.

(126) Afsari, M.; Boochani, A.; Hantezadeh, M. *Optik - International Journal for Light and Electron Optics* **2016**, *127* (23), 11433–11443.

(127) Li, J.; Yin, W.-G.; Wu, L.; Zhu, P.; Konstantinova, T.; Tao, J.; Yang, J.; Cheong, S.-W.; Carbone, F.; Misewich, J. A.; Hill, J. P.; Wang, X.; Cava, R. J.; Zhu, Y. *npj Quant Mater* **2016**, *1* (1), 221–227.

(128) Wei, T.-C.; Wang, H.-P.; Liu, H.-J.; Tsai, D.-S.; Ke, J.-J.; Wu, C.-L.; Yin, Y.-P.; Zhan, Q.; Lin, G.-R.; Chu, Y.-H.; He, J.-H. *Nature Communications* **2017**, *8*, 15018.

(129) Wu, X.; Tan, L. Z.; Shen, X.; Hu, Te; Miyata, K.; Trinh, M. T.; Li, R.; Coffee, R.; Liu, S.; Egger, D. A.; Makasyuk, I.; Zheng, Q.; Fry, A.; Robinson, J. S.; Smith, M. D.; Guzelturk, B.; Karunadasa, H. I.; Wang, X.; Zhu, X.; Kronik, L.; Rappe, A. M.; Lindenberg, A. M. *Science Advances* **2017**, *3* (7), e1602388–e1602388.

(130) Ruth, A.; Brennan, M. C.; Draguta, S.; Morozov, Y. V.; Zhukovskyi, M.; Janko, B.; Zapol, P.; Kuno, M. *ACS Energy Lett.* **2018**, *3* (10), 2321–2328.

(131) Kohn, W.; Sham, L. J. *Phys. Rev.* **1965**, *140* (4A), A1133–A1138.

(132) Perdew, J. P.; Burke, K.; Ernzerhof, M. *Phys. Rev. Lett.* **1996**, *77* (18), 3865–3868.

(133) BLOCHL, P. E. *Phys. Rev. B* **1994**, *50* (24), 17953–17979.

(134) Pulay, P. *Chem. Phys. Lett.* **1980**, *73* (2), 393–398.

(135) Roknuzzaman, M.; Ostrikov, K. K.; Wang, H.; Du, A.; Tesfamichael, T. *Scientific Reports* **2017**, *7* (1), 14025.

(136) Hu, M.; Ge, C.; Yu, J.; Feng, J. *J. Phys. Chem. C* **2017**, *121* (48), 27053–27058.

(137) Li, W.; Rothmann, M. U.; Liu, A.; Wang, Z.; Zhang, Y.; Pascoe, A. R.; Lu, J.; Jiang, L.; Chen, Y.; Huang, F.; Peng, Y.; Bao, Q.; Etheridge, J.; Bach, U.; Cheng, Y.-B. *Adv. Energy Mater.* **2017**, *7* (20), 1700946–1700948.

BIOGRAPHICAL SKETCH

Education and Experience

Physics Department, Florida State University, candidate for PhD degree ***2011 – 2019 summer***

- Dr. Hanwei Gao's group (FSU): interdisciplinary research in light-matter interaction in semiconductors. ***2014 spring – 2019 summer***
- Dr. Stephen Hill's group (FSU): studies of materials exhibiting slow relaxation of magnetization at very low temperature by Electron Magnetic Resonance (EMR).

2012 summer - 2013 fall

B.S. degree, Department of Physics, University of Science and Technology of China (USTC)

2007 – 2011

Research Project

- Quantum tunneling in low-dimensional perovskites (work in progress)
- Scanning photocurrent microscopy on devices based on low-dimensional perovskites (work in progress)
- Interfacial effects in low-dimensional halide perovskites
- Dynamic tuning of optoelectronic properties in halide perovskites
- Light-emitting-diodes based on halide perovskites
- Charge carrier dynamics in vanadium dioxide

Technical Strengths

- Measurement
- Spectrally-resolved Scanning Photocurrent Microscopy
- Atomic Force Microscopy (Kelvin Probe Force Microscopy, Peak-force Tunneling AFM)
- Low temperature optical and electronic measurements (Photoluminescence spectra, photocurrent) in high vacuum systems
- Quantum Design PPMS
- Oxford Cryomagnetic system
- Material synthesis
- Chemical Vapor Deposition
- High Vacuum Thermal Evaporator
- Device fabrication: E-beam Lithography and Photolithography

Publications

1. Xi Wang, Yichuan Ling, Xiujun Lian, Yan Xin, Kamal B. Dhungana, Fernando Perez-Orive, Javon Knox, Zhizhong Chen, Yan Zhou, Drake Beery, Kenneth Hanson, Jian Shi, Shangchao Lin, Hanwei Gao. "Suppressed Phase Separation of Mixed-Halide Perovskites Confined in Endotaxial Matrices", *Nat. Commun*., 10, 695 (2019).
2. Xi Wang, Xiujun Lian, Zihan Zhang, Hanwei Gao. "Could Nanocomposites Continue the Success of Halide Perovskites?", *ACS Energy Lett* 4, 1446-1454 (2019).
3. Xiujun Lian†, Xi Wang†, Yichuan Ling, Eric Lochner, Lei Tan, Yan Zhou, Biwu Ma, Kenneth Hanson, Hanwei Gao. "Light Emitting Diodes Based on Inorganic Composite Halide Perovskites", *Adv. Funct. Mater.*, (2018) († equally contribution).
4. Xi Wang, Yichuan Ling, Yu-Che Chiu, Yijun Du, Jorge Luis Barreda, Fernando Perez-Orive, Biwu Ma, Peng Xiong, Hanwei Gao. "Dynamic Electronic Junctions in Organic–Inorganic Hybrid Perovskites". *Nano lett.* 17, 4831-4839 (2017).
5. X. Wang, H. Gao, "Distinguishing the Photothermal and Photoinjection Effects in Vanadium Dioxide Nanowires", *Nano Lett.*, 15, 7037 (2015).
6. Hanwei Gao, Biwu Ma, Yichuan Ling, Xi Wang. "Bandgap-Tunable Perovskite Materials and Methods of Making the Same", US Patent App. 16/117,628 (2018).
7. Zhizhong Chen, Yiping Wang, Xin Sun, Yu Xiang, Yang Hu, Jie Jiang, Jing Feng, Yi-Yang Sun, Xi Wang, Gwo-Ching Wang, Toh-Ming Lu, Hanwei Gao, Esther A Wertz, Jian Shi. "Remote Phononic Effects in Epitaxial Ruddlesden-Popper Halide Perovskites", *J. Phys. Chem. Lett.*, 9, 6676-6682 (2018).
8. Yu Tian, Chenkun Zhou, Michael Worku, Xi Wang, Yichuan Ling, Hanwei Gao, Yan Zhou, Yu Miao, Jingjiao Guan, Biwu Ma. "Highly Efficient Spectrally Stable Red Perovskite Light-Emitting Diodes", *Adv. Mater.* 30, 1707093 (2018).
9. Zhizhong Chen, Yiping Wang, Xin Sun, Yuwei Guo, Yang Hu, Esther Wertz, Xi Wang, Hanwei Gao, Toh-Ming Lu, Jian Shi. "Van Der Waals Hybrid Perovskite of High Optical Quality by Chemical Vapor Deposition", *Adv. Opt. Mater.* 5, 1700373 (2017).
10. Yichuan Ling, Lei Tan, Xi Wang, Yan Zhou, Yan Xin, Biwu Ma, Kenneth Hanson, Hanwei Gao. "Composite perovskites of cesium lead bromide for optimized photoluminescence". *J. Phys. Chem. Lett.*, 8, 3266-3271 (2017).

11. Y. Ling, Y. Tian, X. Wang, J.C. Wang, J.M. Knox, F. Perez-Orive, Y. Du, L. Tan, K. Hanson, B. Ma, H. Gao. "Enhanced Optical and Electrical Properties of Polymer-Assisted All-Inorganic Perovskites for Light-Emitting Diodes", *Adv. Mater.*, 28, 8983 (2016).
12. Y. Ling, Z. Yuan, Y. Tian, X. Wang, J. C. Wang, Y. Xin, K. Hanson, B. Ma, H. Gao, "Bright Light-Emitting Diodes Based on Organometal Halide Perovskite Nanoplatelets", *Adv. Mater.*, 28, 305 (2016).
13. Mincheng Zhong, Xi Wang, Jinhua Zhou, Ziqiang Wang, Yinmei Li. "Optimal beam diameter for lateral optical forces on microspheres at a water-air interface" *Chin. Opt. Lett.*12, 011403 (2014).

Honors and Awards

2019 Creativity and Research Award (FSU highest graduate research honor).

2018 Clara Kibler Davis Scholarship

2018 Ermine M. Owenby Jr. Fund to Promote Excellence

2016-18 Evelyn and John Baugh Research Presentation Scholarship

2016 Anna Jane Hendren Runyan Graduate and Undergraduate Awards

2016-18 COGS Conference Presentation Grant

2016 Second Prize (2nd out of 100) in Condensed Matter Research Poster Competition (Florida Chapter of the American Vacuum Society, and Florida Society for Microscopy 2016 Annual Joint Symposium)

2013 John E. & Melissa D. Gray Novotny Award (FSU physics department)

2011 Dean's scholarship (FSU physics department)

2010 USTC Outstanding Student Scholarship (Silver)

2010 USTC Undergraduate Research Project Outstanding Award

2008 USTC Outstanding Student Scholarship (Bronze)

2007 USTC Outstanding Freshman Scholarship (Bronze)

Presentations

1. Xi Wang, Yichuan Ling, Fernando Perez-Orive, Hanwei Gao. "Suppressed Phase Separation of Mixed-Halide Perovskites Confined in Endotaxial Matrices", ***Talk****, Bulletin of the Material Research Society, MRS Spring Meeting* (2019).

2. Xi Wang, Yichuan Ling, Fernando Perez-Orive, Hanwei Gao. “Dynamic Electronic Junctions in Halide Perovskites”, ***Talk****, Bulletin of the Material Research Society, MRS Spring Meeting* (2018).

3. Xi Wang, Yichuan Ling, Yu-Che Chiu, Yijun Du, Jorge Luis Barreda Esparza, Fernando Perez-Orive, Biwu Ma, Peng Xiong, Hanwei Gao. “Dynamic Tuning of Charge Transport in Organometal Halide Perovskites”, ***Talk****, Bulletin of the American Physical Society, APS March Meeting* (2017).

4. Xi Wang , Hanwei Gao, “Distinguishing the Photothermal and Photoinjection Effects in Vanadium Dioxide Nanowires”, ***Talk****, Bulletin of the American Physical Society, APS March Meeting* (2016).

5. Xi Wang , Hanwei Gao, “Distinguishing the Photothermal and Photoinjection Effects in Vanadium Dioxide Nanowires”, ***poster presentation****, Florida Chapter of the American Vacuum Society, and Florida Society for Microscopy 2016 Annual Joint Symposium* (2016).

6. Xi Wang, Hanwei Gao, “Distinguishing the Photothermal and Photoinjection Effects in Vanadium Dioxide Nanowires”, ***Talk****, Nano Florida* (2015).

7. Xi Wang, Sanhita Ghosh, Saiti Datta, Michael Hoch, Pedro Schlottmann, Haidong Zhou, Stephen Hill. “EPR Studies on the Kagomé System $Pr_3Ga_5SiO_{14}$*”.* ***Talk****, Florida Inorganic & Materials Symposium, Oct. 18-19, 2013.*

8. Xi Wang, Sanhita Ghosh, Saiti Datta, Michael Hoch, Pedro Schlottmann, Haidong Zhou, Stephen Hill. “EPR Studies on the Kagomé System $Pr_3Ga_5SiO_{14}$*”.* ***Poster****, 42nd Southeastern Magnetic Resonance Conference, Tallahassee, FL,* October 11-13, 2013.